

CONTROL OF FLOW STRUCTURE ON VFE-2 DELTA WING
WITH PASSIVE BLEEDING USING CFD

A THESIS SUBMITTED TO
THE GRADUATE SCHOOL OF NATURAL AND APPLIED SCIENCES
OF
MIDDLE EAST TECHNICAL UNIVERSITY

BY

SERDAR EMİN SAYILIR

IN PARTIAL FULFILLMENT OF THE REQUIREMENTS
FOR
THE DEGREE OF MASTER OF SCIENCE
IN
MECHANICAL ENGINEERING

JANUARY 2018

Approval of the thesis:

**CONTROL OF FLOW STRUCTURE ON VFE-2 DELTA WING
WITH PASSIVE BLEEDING USING CFD**

submitted by **SERDAR EMİN SAYILIR** in partial fulfillment of the requirements
for the degree of **Master of Science in Mechanical Engineering Department,**
Middle East Technical University by,

Prof. Dr. Gülbin Dural Ünver
Dean, Graduate School of **Natural and Applied Sciences**

Prof. Dr. Mehmet Ali Sahir Arıkan
Head of Department, **Mechanical Engineering**

Assoc. Prof. Dr. Mehmet Metin Yavuz
Supervisor, **Mechanical Engineering Dept., METU**

Examining Committee Members:

Prof. Dr. Mehmet Haluk Aksel
Mechanical Engineering Dept., METU

Assoc. Prof. Dr. Mehmet Metin Yavuz
Mechanical Engineering Dept., METU

Prof. Dr. Kahraman Albayrak
Mechanical Engineering Dept., METU

Assoc. Prof. Dr. Cüneyt Sert
Mechanical Engineering Dept., METU

Assoc. Prof. Dr. Murat Kadri Aktaş
Mechanical Engineering Dept., TOBB University

Date: January 18, 2018

I hereby declare that all information in this document has been obtained and presented in accordance with academic rules and ethical conduct. I also declare that, as required by these rules and conduct, I have fully cited and referenced all material and results that are not original to this work.

Name, Last name: Serdar Emin Sayılır

Signature:

ABSTRACT

CONTROL OF FLOW STRUCTURE ON VFE-2 DELTA WING WITH PASSIVE BLEEDING USING CFD

Sayılır, Serdar Emin

M.S., Department of Mechanical Engineering

Supervisor: Assoc. Prof. Dr. Mehmet Metin Yavuz

January 2018, 102 pages

The utilization of slender delta wings on military platforms like fighter jets and missiles has been a great topic of aerodynamics research for many decades from both experimental and numerical point of view as a result of their superior contributions to the flight performance. Second Vortex Flow Experiment (VFE-2) was carried out by NATO Research and Technology Organization between 2003 and 2008 to judge the realistic capability of the CFD codes which had been developed for simulating the leading edge vortices and their breakdowns occurring on this type of wings.

In the present study, the turbulent vortical flow and its breakdown in incompressible conditions over a generic VFE-2 wing were modeled using commercial code, ANSYS Fluent. First, the grid independence study was conducted for the sharp edged 65° swept VFE-2 wing to ensure the results of the simulations do not vary with mesh density. Then, different RANS based turbulence models including Spalart-Allmaras (S-A) and SST $k-\omega$ with curvature corrections were used for validation purposes where the results of the current study were compared with both Detached Eddy Simulation (DES) results and the experimental data available in the literature. The results indicated that SST $k-\omega$ model with curvature correction was

quite successful in simulating the vortical flow particularly in terms of the secondary separations and predicting the vortex breakdown location.

Once a complete confidence of the grid and the turbulence model was ensured, flow control using passive bleeding was tested to check the effectiveness of bleeding on manipulating the flow field and delaying the location of vortex breakdown. The bleeding method bases on the idea of letting the air stream from the pressure side of the wing to the suction side through the holes on the wing body and injecting it into the vortical flow field to strengthen the vortex structure and delay its breakdown. For delta wings, only a limited number of applications of this passive approach yet have been implemented up until now. In the present study, the control technique was applied in three sets of investigation including variation in sizes, inclination angles and shapes of bleed holes; where in each set one parameter was altered with keeping the others constant. For each investigation set, a delay of breakdown to about 10% of the chord wise location compared to the no-control case as well as a slight improvement in the lift force and coefficient was achieved. Combining the best case parameters from each set, however, resulted a less retardation compared to the each parameter's individual control performance.

Keywords: VFE-2 delta wing, sharp leading edge, vortex breakdown, CFD, passive flow control, bleeding

ÖZ

VFE-2 DELTA KANADI ÜZERİNDE HAD KULLANARAK PASİF AKITMA İLE AKIŞ YAPISI KONTROLÜ

Sayılır, Serdar Emin

Yüksek Lisans, Makina Mühendisliği Bölümü

Tez Yöneticisi: Doç. Dr. Mehmet Metin Yavuz

Ocak 2018, 102 sayfa

Uçuş performansının iyileşmesine yönelik üstün özelliklerinden dolayı, yüksek süpürme açılı delta kanatların savaş uçakları ve füzeler gibi askeri uygulamalarda kullanımları, uzun yıllardır hem deneysel hem de numerik çalışma açısından çok önemli bir aerodinamik araştırma konusu olmuştur. Bu tip kanatların üzerinde oluşan hücum kenarı girdapları ve bunların kırımını sayısal olarak simüle etmek için geliştirilen CFD kodlarının gerçekçi kapasitelerini değerlendirmek amacıyla, 2003-2008 yılları arasında NATO Araştırma ve Teknoloji Organizasyonu tarafından İkinci Girdap Akış Deneyi (VFE-2) gerçekleştirilmiştir.

Bu çalışmada, eşdeğer bir VFE-2 kanadı üzerinde oluşan, sıkıştırılmaz koşuldaki türbülanslı girdaplı akış ve bu akışın kırımını, ticari ANSYS Fluent yazılımı kullanılarak modellenmiştir. İlk olarak, ağ yoğunluğu ile sonuçların değişmediğinden emin olmak maksadıyla, keskin kenarlı ve 65° süpürme açılı VFE-2 kanadı için ağdan bağımsızlık çalışması yapılmıştır. Ardından, RANS tabanlı türbülans modelleri olan Spalart-Allmaras (S-A) ve SST $k-\omega$ with curvature corrections kullanılarak elde edilen çözüm sonuçları, literatürden sağlanan Detached Eddy Simulation (DES) sonuçları ve deneysel veriler ile doğrulanmıştır. Sonuçlar, SST $k-\omega$ with curvature correction modelinin, özellikle ikincil ayrışmalar ve girdap

kırınım yerinin tespiti açısından, girdaplı akışın simülasyonunda çok başarılı olduğunu göstermiştir.

Ağ ve türbülans modeli performansından tam olarak emin olduktan sonra, akıtma yönteminin akış alanını manipüle etme ve girdap kırınımını geciktirmeye yönelik etkinliğini test etmek amacıyla pasif akıtma ile akış kontrolü yöntemi uygulanmıştır. Akıtma yöntemi havanın kanat üzerinde açılan oluk veya deliklerinden, basınç tarafından emiş tarafına doğru, akmasına izin verilmesi ve girdap yapısını güçlendirerek kırınımını geciktirmek üzere girdaplı akış alanına enjekte edilmesi fikrine dayanır. Delta kanatlar için şimdiye kadar bu pasif yaklaşımın sadece sınırlı sayıda uygulaması gerçekleştirilmiştir. Bu çalışmada söz konusu teknik, akıtma deliklerinin büyüklükleri, eğim açıları ve şekillerinin değişim etkilerinin incelendiği üç farklı set üzerinden uygulanmış olup burada her set içinde ilgili parametre değiştirilirken diğer iki parametre sabit tutulmuştur. Her bir inceleme seti için kaldırma kuvveti ve katsayısının az miktarda artışının yanında girdap kırınımının, akış kontrolünün olmadığı durumla kıyasla, kord boyu lokasyonunun yaklaşık 10%'u kadar geciktirilmesi sağlanmıştır. Ancak her setteki en iyi parametreleri bir araya getirmek, her parametrenin tekil kontrol performansına kıyasla daha düşük öteleme sonucunu vermiştir.

Anahtar Kelimeler: VFE-2 delta kanadı, keskin hücum kenarı, girdap kırınımı, hesaplamalı akışkanlar dinamiği, pasif akış kontrolü, akıtma

To my family

ACKNOWLEDGMENTS

I first would like to deliver my sincerest gratitude to my supervisor Assoc. Prof. Dr. Mehmet Metin Yavuz for his guidance, encouragement, support, criticism and patience throughout this study. It was really a precious experience for me to work with such a good person in my life.

Later I would like to express my great appreciation to my friends Can Küçükyılmaz, Gökay Günacar, Kadir Gürsoy, Cenk Çetin, Burak Gülsaçan and all the current and former members of Yavuz Research Group for their support and help in surmounting the problems that I faced during the study.

I also would like to thank to my dear commanders and colleagues in Turkish Army for their encouragement, guidance and help for completing the study while I was serving as a military officer.

Last but the most, I would like to deliver my deepest gratitude to my beloved family: my parents Münire and Zeki Sayılır, my sister Sibel Sayılır and my brother Selçuk Sayılır together with his wife and children, for their unconditional and invaluable love, endless support and encouragement all my life long.

TABLE OF CONTENTS

ABSTRACT	v
ÖZ	vii
ACKNOWLEDGMENTS	x
TABLE OF CONTENTS	xi
LIST OF TABLES	xiii
LIST OF FIGURES	xiv
NOMENCLATURE	xvii
CHAPTERS	
1. INTRODUCTION	1
1.1 Motivation	5
1.2 Aim of the Study	6
2. LITERATURE SURVEY	9
2.1 Flow Over Slender Delta Wings at High Angle of Attack	9
2.2 Flow Asymmetry, Shear Layer Instabilities and Vortex Wandering	14
2.3 Effect of Leading Edge Bluntness	16
2.4 Breakdown of the Leading Edge Vortices	19
2.5 Control of Vortical Flow Over Delta Wings	24
3. COMPUTATIONAL MODELING	31
3.1 Wing Modeling	31
3.2 Mesh Generation	36
3.3 Governing Equations and Turbulence Models	44
3.3.1 Reynolds Averaging and Boussinesq Approximation	44

3.3.2 Spalart-Allmaras (S-A) Model	46
3.3.3 Shear-Stress Transport (SST) k- ω Model	47
3.4 Grid Independence Study	50
4. VALIDATION STUDY	61
5. FLOW CONTROL USING BLEEDING.....	75
6. CONCLUSION.....	89
6.1 Summary and Conclusions.....	89
6.2 Recommendations for Future Work	90
REFERENCES.....	91
APPENDICES	
A. TURBULENCE MODELING.....	97
A.1. Spalart-Allmaras Model (Continued From Section 3.3.2).....	97
A.2. Shear-Stress Transport (SST) k- ω Model (Continued From Section 3.3.3).....	99

LIST OF TABLES

Table 3.1 Main dimensions of the wing.....	37
Table 3.2 Distance to chord ratios	38
Table 3.3 Meshing strategy	39
Table 3.4 Mesh quality	40
Table 3.5 Boundary conditions.....	51
Table 3.6 Vortex breakdown locations of four meshes	60
Table 4.1 Vortex core location coordinates	73
Table 4.2 Vortex breakdown locations of the turbulence models and experiment	73
Table 5.1 Control work strategy	77
Table 5.2 Control work vortex breakdown locations	83
Table 5.3 Lift Variation between the No-Control and Control Cases	87

LIST OF FIGURES

Figure 1.1 A slender delta wing and the vortical flow structures emanating over it at angle of attack [1].....	2
Figure 1.2 Vortex breakdown visualized in a water tunnel over a slender delta wing as a result of the emission of colored dye near the apex [2].....	3
Figure 2.1 Contribution of the vortex lift to the total lift performance of a slender delta wing [9]	10
Figure 2.2 Leading edge vortex formation and related pressure distribution [13]	11
Figure 2.3 Primary and secondary vortices and corresponding surface patterns [14]	11
Figure 2.4 Cross sectional structure of leading edge primary vortex [14]	12
Figure 2.5 Change of the core flow from a jet-type to a wake-type [12]	14
Figure 2.6 Vortical sub structures in the shear layer and asymmetric expanding vortex cores without breakdown [20].....	16
Figure 2.7 Oil flow visualization and vortex system for rounded leading edge [29].	17
Figure 2.8 The effects of bluntness on leading edge vortex structures [28].....	18
Figure 2.9 Bubble and spiral type vortex breakdown [17]	20
Figure 2.10 Process of spiral type vortex breakdown [17].....	20
Figure 2.11 The vorticity components for a vortex and their senses [41].....	23
Figure 2.12 Azimuthal vorticity contours and sectional streamlines generated numerically on a vertical plane containing the vortex axis [11]	23
Figure 2.13 Flow control with tandem delta wing configuration [43]	25
Figure 2.14 Examples for leading edge flaps and extensions [43]	27
Figure 2.15 Plasma actuator control conducted on a slender wing [45]	27
Figure 2.16 Avoiding of vortex breakdown with trailing edge jet blowing [46].....	28
Figure 2.17 General effectiveness assessments of pneumatic control techniques [43]	28
Figure 2.18 Effectiveness comparison of steady and unsteady blowing [43]	29
Figure 3.1 VFE-2 wing model details [4].....	32
Figure 3.2 Fore-sting details [4].....	33

Figure 3.3 VFE-2 wing three-view drawing and sharp vs. rounded edges [47].....	34
Figure 3.4 Functions representing the wing semithickness contours [4].....	35
Figure 3.5 Isometric views of the 3D model built in Solidwoks.....	35
Figure 3.6 Computational domain	37
Figure 3.7 Surfaces and edges to be distinctly meshed with different element sizes.	39
Figure 3.8 General view of overall meshed domain.....	41
Figure 3.9 Inflated surface mesh around the wing	41
Figure 3.10 Surface meshes: a) Mesh 1, b) Mesh 2, c) Mesh 3, and d) Mesh 4	42
Figure 3.11 Near wing volume meshes: a) Mesh 1, b) Mesh 2, c) Mesh 3 and d) Mesh 4.....	43
Figure 3.12 Scaled residual history of Mesh 3 calculation	52
Figure 3.13 Monitor points distribution: a) top (numbers were given in line with the x-coordinate from the apex) and b) side view	52
Figure 3.14 Velocity magnitude histories at a) Point 2, b) Point 3 and c) Point 6.....	54
Figure 3.15 y^+ contour of Mesh 2.....	54
Figure 3.16 Stations where pressure coefficient is calculated	55
Figure 3.17 Cp profiles of the four meshes at chord wise stations on the suction side a) $x/C=0.4$, b) $x/C=0.6$	56
Figure 3.18 Cp contours: a) Mesh 1, b) Mesh 2, c) Mesh 3, and d) Mesh 4.....	57
Figure 3.19 Azimuthal vorticity contours: a) Mesh 1, b) Mesh 2, c) Mesh 3 and d) Mesh 4.....	59
Figure 3.20 Contours of axial velocity normalized free stream velocity ($U= u/U_0$) of a) Mesh 1, b) Mesh 2, c) Mesh 3 and d) Mesh 4 at where axial velocity first switches sign (breakdown initiation).	60
Figure 4.1 Cp contours of a) S-A-cc and b) SST k- ω -cc	62
Figure 4.2 Azimuthal vorticity contours of a) S-A-cc and b) SST k- ω -cc	63
Figure 4.3 Span wise Cp profiles of the experiment [7] and three numerical simulations at chord wise stations on suction side a) $x/C=0.2$, b) $x/C=0.4$, c) $x/C=0.6$, d) $x/C=0.8$, and e) $x/C=0.95$	67

Figure 4.4 Experimental and numerical streamlines with C_p contours a) experiment [7], b) DES [7], c) S-A-cc and d) SST $k-\omega$ -cc	68
Figure 4.5 Normalized axial velocity ($U=u/U_0$) contours at $x/C= 0.2, 0.4, 0.65,$ and 0.95 : a) DES [7], b) S-A-cc and c) SST $k-\omega$ -cc	72
Figure 5.1 Hole 1: a) location (top view), b) sketch on the upper surface and c) side view	78
Figure 5.2 Hole 1 isometric views	79
Figure 5.3 Size investigation set a) Hole 1, b) Hole 2 and c) Hole 3.....	79
Figure 5.4 Angle investigation set a) Hole 1, b) Hole 4, c) Hole 5 and d) Hole 6.....	80
Figure 5.5 Shape investigation set a) Hole 1, b) Hole 7, c) Hole 8, d) Hole 9, e) Hole 10 and f) Hole 11.....	81
Figure 5.6 Swirling strength colored by stream-wise velocity for: a) Base, b) Hole 2, c) Hole 5 and d) Hole 7	84
Figure 5.7 Span wise C_p profiles of the non-controlled and three controlled cases at chord wise stations on the suction side a) $x/C=0.4,$ b) $x/C=0.65$ and c) $x/C=0.8$	87

NOMENCLATURE

Λ	Sweep angle ($^{\circ}$)
C_p	Pressure coefficient
C_{μ}	Momentum coefficient
ΔC_N	Change in normal force coefficient
ΔX_{bd}	Change in breakdown location
C_L	Lift coefficient
α	Angle of attack ($^{\circ}$)
k	Turbulence kinetic energy (m^2/s^2)
μ_t	Turbulent viscosity (Pa.s)
ε	Turbulence dissipation rate (m^2/s^3)
ω	Specific turbulence dissipation rate (1/s)
Re_{mac}	Reynolds number based on mean aerodynamic chord
M	Mach number
Ω_z	Azimuthal vorticity (s^{-1})
u	Axial velocity (m/s)
U_0	Freestream velocity (m/s)
U	Normalized free stream velocity
x	Cartesian x-coordinate measure of a point (m)
C	Wing root chord (m)

y^+	A non-dimensional wall distance
cc	Curvature correction
CFD	Computational fluid dynamics
DES	Detached eddy simulation
Exp	Experiment
S-A	Spalart Allmaras
SST	Shear stress transport
R	Radius (m)
A/R	Aspect ratio

CHAPTER 1

INTRODUCTION

Wing planforms having delta (triangle) like shapes have been topics of great interest in aerodynamics researches for many decades. Main reason for these extensive efforts is lying under useful features of delta wings such that increasing maximum angle of attack and cruise speed, even to the supersonic, providing higher lift capability and enabling sharper maneuvers with better structural stability. Delta wings have a wide area of utilization, especially for military purposes, beginning from fighter jets to novel unmanned aerial vehicles (UAV), mini-micro aerial vehicles (MAV) or unmanned combat aerial vehicles (UCAV).

One of the major classification methods for these wings is based on their sweep angle (Λ). Wings are called as ‘slender or high swept’ when Λ is higher than 55° and ‘non-slender or low swept’ when it is between 35° and 55° . Although there are certain differences between the air flows over the both types of wings, a common description can be made on their general aerodynamics. At certain angle of attack, two counter rotating vortices above the suction side, which are formed by rolling up of vortex sheets separating at both leading edges, dominate their flow fields. These primary leading edge vortices interact with boundary layer at their reattachment zones and cause secondary, even tertiary vortices to develop. Figure 1.1 illustrates a sample delta wing and the vortical flow structures emanating over it at angle of attack [1].

Another prominent parameter that must be respected while dealing with the flow over delta wings is their leading edges. They can be sharp or rounded with different values and this also brings significant differences relating to the number of vortices, their initiation positions, mechanisms, strengths, etc.

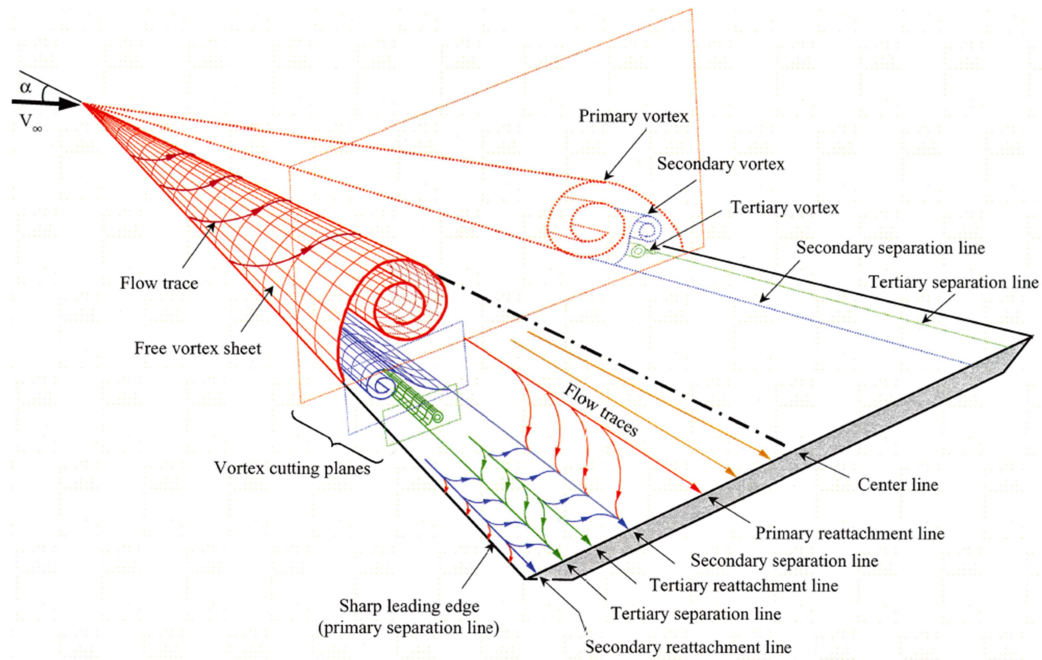


Figure 1.1 A slender delta wing and the vortical flow structures emanating over it at angle of attack [1]

In any of these cases, however, they are the leading edge vortices which make the most important contributions to delta wings in gaining the useful characteristics mentioned above. Increasing angle of attack also increases the strength of the vortices and even enhances their benefits. However, at sufficiently high angle of attack the vortices undergo a sudden expansion over the wing, known as breakdown or burst. Figure 1.2 reveals a visualization of vortex breakdown performed by Mitchell and Delery [2]. This phenomenon has adverse effects on the delta wings performances and brings out negative consequences like considerable loss of lift, pressure and velocity fluctuations causing problems of stability and random loadings on the wing body that may lead to fatigue. Besides, with further increasing the incident, breakdown location moves upwards to the apex of the wing and at a certain angle this might yield stall, loss of all aerodynamic lift because of the separation of the boundary layer from the wing surface.

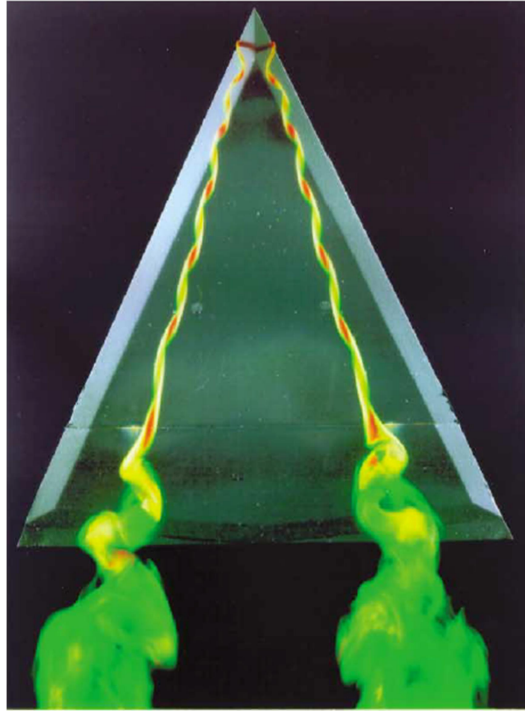


Figure 1.2 Vortex breakdown visualized in a water tunnel over a slender delta wing as a result of the emission of colored dye near the apex [2]

Thus, stabilizing the vortices to prevent or delay their breakdown has been of a great concern for aerodynamicists over many years. In order to do so, firstly understanding the full nature of the flow structure around delta wing in depth has a crucial importance; and a great amount of experimental and numerical effort has been made on this issue throughout many years especially concerning high swept wings. One of these efforts was famous as Vortex Flow Experiment-1 (VFE-1) which was carried out on a sharp edged wing with a sweep angle of 65° in 1984 – 1986. The aim of this experiment was to produce good experimental data for validation of the Euler codes, which had reached a high standard in calculation of vortical flows at the beginning of 1980's [3]. However it was seen that the Euler codes were not well suited to calculate the pressure distribution on the slender wing properly since the secondary vortex separation was not simulated by the inviscid equations, even for the sharp leading edge having fixed primary separation, which is the leading edge itself [3].

Along the following years, remarkable progress was achieved in the numerical calculation of vortical flows by taking into account the viscous effects through solutions of the RANS equations. Utilizing the new turbulence models the Reynolds numbers (Re) effects to be included now, attached boundary layers to be covered properly and the secondary vortices to be turned out. This development in computational methods, on the other hand, brought together with the necessity for a new and more detailed experimental data for validation. Therefore a Second International Vortex Flow Experiment (VFE-2) was conducted under the supervision of NATO-RTO (Research and Technology Organization) in 2003-2008 [3].

A different slender delta wing, which had originally been produced and tested experimentally by NASA for a large variety of Mach numbers (M) and Re in 1996 [4], was selected as a common configuration for VFE-2. The wing had again 65° sweep angle and was offering the researchers the opportunity to work on both sharp and rounded leading edges with its interchangeable leading edge design characteristics. Steady and unsteady measurements were implemented in experimental VFE-2 studies to gain a comprehensive insight about the vortical flow around the wing. Besides, number of numerical analysis was performed with fully turbulent approach, meaning that the flow is supposed to be always turbulent, to model the unsteady as well as time averaged nature of the flow field.

The main emphasis for the new experiments, however, was directed towards studies on the rounded leading edge configuration, since a large number of investigations are available in the literature for delta wings with sharp leading edges [3]. In addition to this, even though some experimental studies in VFE-2 handled incompressible flow cases, the numerical ones did only concerned compressible free stream conditions with $M \geq 0.4$ and $Re_{mac} \geq 3 \times 10^6$. Besides, the investigations were decided to be carried out for three different angles of attack as 13° , 18° and 23° which brings out also three different flow regimes for the VFE-2 wing as to be onset of the vortical flow, fully developed (fully separated) vortical flow without vortex breakdown and fully developed (fully separated) vortical flow with vortex breakdown correspondingly. Considering different selections of the parameters above, a large

number of investigation cases was deduced and addressed by the researchers worldwide during VFE-2 as well as the following years.

As previously mentioned, the achievements in correct representation of the vortical flow over delta wings provide important data for researchers working on the flow control activities for that type of planforms. Different kinds of flow control techniques which can be sort as active and passive or steady and unsteady have been extensively investigated in terms their effectiveness to retard the breakdown location. However, none of these techniques has clearly demonstrated a superior performance in controlling either the vortical flow structure or its breakdown location. Each technique, does, on the other hand, provide a unique approach to the control of the vortex breakdown depending on the desired outcome [2].

Passive flow control strategies do not need external energy input and therefore have advantages of simplicity and practicality [5]. Although they are generally found less effective than active methods, some novel techniques draw attention with their success, currently. Bleeding control is one of them. In this concept, air is allowed to stream from the pressure side to the suction side through the holes on the wing body and injected into the vortical flow field. This bleeding air is supposed to manipulate the vortex in a manner to stabilize it and so to move its breakdown towards the trailing edge. The number of efforts targeting to assess the effectiveness of the method, especially for delta wings, is growing today by applying to various cases and with different bleeding configurations.

1.1 Motivation

Importance of slender delta wings have incrementally pursued along many decades because of their advantageous aerodynamic features especially for military designs. In parallel to this, a comprehensive insight about the vortical flow taking place on these wings has always been a critical issue for researchers since only then an effective flow control could be realized to achieve the desired performances. Being aware of this fact and the necessity for more detailed experimental data of the flow around slender wings, with sharp as well as rounded leading edges, to judge the

improved capabilities of the computational turbulence models, NATO-RTO organized VFE-2 in the mid 2000's. Even today, successful numerical representation of the flow physics around a VFE-2 wing and manipulation of its leading edge vortices to prevent or delay their breakdown for the sake of aerodynamic superiority of the wing, is a matter of investigation. It is seen in literature that neither during nor after VFE-2, the turbulent incompressible flow over the wing, which corresponds relatively low speed flight conditions and low Re , has not yet been analyzed in depth from the numerical point of view. In addition to that, only a small number of control studies can be found dedicated to VFE-2 wing yet until now and just one of them covered a bleeding application in 2015 [6]. Therefore, first achieving a proper CFD simulation for a sharp edged VFE-2 wing under incompressible flow conditions, with a genuine unstructured grid and solution set up, and predicting vortex formations and breakdowns correctly can contribute to the ongoing efforts. After that, taking the advantage of practical applicability of CFD, conducting number of bleeding control cases to the VFE-2 wing as a novel passive method may notably help to build a general assessment for future studies on the same type of applications. The bleeding approach proposes injection of air, which is allowed to stream from the pressure side to the suction side through the holes on the wing body, into the vortical flow field to reinforce the vortex structure and delay its breakdown.

1.2 Aim of the Study

In this thesis study, it was aimed to numerically model the incompressible air flow passing by a sharp edged slender VFE-2 wing at 23° angle of attack with the conditions of $Re_{mac} = 1 \times 10^6$ and $M = 0.07$ using a Reynolds Average Navier Stokes (RANS) turbulence model with steady and fully turbulent approach, and then to simulate bleeding control investigations with the same model aiming to vortex breakdown retardation over the wing. The CAD model of the wing was generated referring to the definitions of Chu and Luckring [2]. The calculations were performed using SST $k-\omega$ and Spalart-Allmaras (S-A) with the necessary curvature correction extensions. Domain discretization, one of the most crucial processes of the numerical studies, was unstructured and a strategy was built to assure the essential grid

refinement over the wing surface. The mesh independence was achieved by the calculations done with SST $k-\omega$ first, then the results of the two RANS models making use of this mesh were compared with each other as well as with the unsteady SST Detached Eddy Simulation (DES) results of Tangermann et al. [7] and the experimental results obtained in VFE-2 by Furman and Breitsamter [8] regarding surface pressure distributions, normalized axial velocity and azimuthal vorticity contours, surface streamlines and vortex breakdown locations. After validating the corresponding turbulence model, bleeding control technique was applied by three sets of investigation. Each set altered one of the three parameters belonging to the bleed holes, that are size, inclination angle and shape, and kept the other two constant for investigating the effect of the corresponding parameter to the breakdown location shift. In the “size investigation set”, three hole sizes as being small, medium and large, were tested and in the “inclination angle set” four angles, being 20° , 25° , 30° and 35° , were examined. In the third set, on the other hand, the effect of six different shape configurations, named as “rectangle”, “circle”, “high aspect ratio chord wise rectangle”, “chord wise slot”, “high aspect ratio span wise rectangle” and “span wise slot” were compared to each other. After these simulations, a new bleed hole that combines the best resulting parameters of each set was investigated, in terms of its effectiveness to retard the breakdown of the vortex.

CHAPTER 2

LITERATURE SURVEY

2.1 Flow Over Slender Delta Wings at High Angle of Attack

A common characteristic of flows over delta wings and bodies of high sweep angle flying at high angles of attack is the induced aerodynamic forces and moments due to formation of vortices usually emitted from the leading edges of lifting surfaces or the smooth surface of the bodies. These vortices cause strong swirling velocity fields that bring regions of low pressure near the surface and as a consequence the generation of additional aerodynamic load known as the "vortex induced lift" [1]. Figure 2.1 [9] indicates the nonlinear contribution of the vortex lift to the total lift performance of a slender delta wing. Through almost a half century, the beneficial effects of vortices have been exploited by the aircraft designers for achieving high lift during takeoff/landing and enhancing the maneuverability of platforms such as agile fighters, supersonic commercial airplanes, aerospace vehicles, guided missiles and specifically in last decades unmanned aerial vehicles (UAV) or unmanned combat aerial vehicles (UCAV).

The formation of vortices on slender configurations starts already at low angles of attack developing from the wing rear part to the apex. Flow approaching a swept-back wing meets initially the lower surface of it and moves outboard towards the leading edge [10]. Unable to negotiate the sharp turn the flow separates from the leading edge and, as a consequence of the span wise pressure gradient on the upper side, rolls up by self-induction forming into a helical free shear layer positioned over the wing. This layer is continuously fed by vorticity shedding of the separated flow, sourcing from both the wing upper and lower surfaces around the leading edge, and surrounds a concentrated viscous core that ejects flow downstream. This core grows in diameter linearly downstream getting a conical form and its size is effectively independent of Reynolds number [11]. When vorticity feeding exists over the entire

leading-edge, the primary vortex is called “fully developed” [12]. Figure 2.2 [13] and Figure 2.3 [14] reveal the details of delta wing primary vortex formation and its inner structure with the corresponding surface patterns.

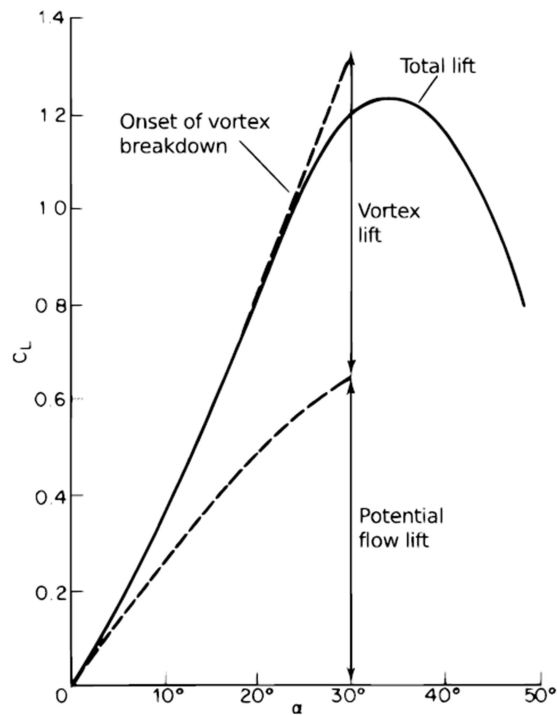


Figure 2.1 Contribution of the vortex lift to the total lift performance of a slender delta wing [9]

The leading edge vortex has a straight trajectory over most of the wing extent. Over the angle of attack range that is of interest, the vortex sweep angle is nearly independent of increasing angle of attack this constant value is almost proportional to the wing sweep angle [11]. The angle between the vortex core and the wing surface also increases linearly with angle of attack. The overall vortex circulation increases linearly with chord wise distance downstream. Besides, the circulation increases with angle of attack and decreases with leading edge sweep [11]. The ratio of tangential to axial velocity components of the vortex core, sometimes called as “swirl number,” is related to the rate of increase of swirl along the core.

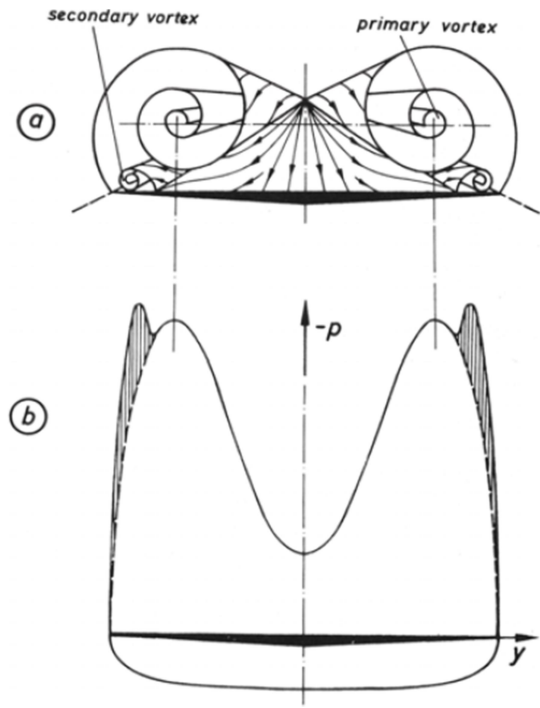


Figure 2.2 Leading edge vortex formation and related pressure distribution [13]

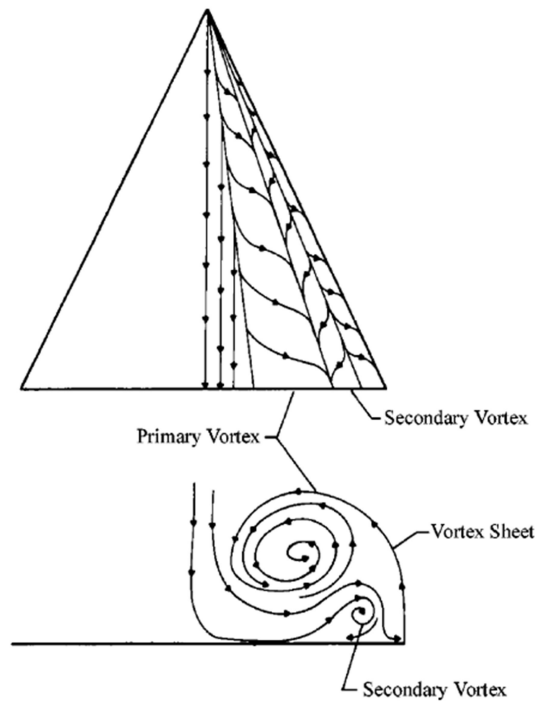


Figure 2.3 Primary and secondary vortices and corresponding surface patterns [14]

Observing the vortex structure on a vertical cross plane, it can be divided into three regions as shear layer at the outermost, rotational core in the middle and viscous sub-core at the center [15]. The bulk of the swirling flow outside the boundary layer can be treated as non-dissipative although the viscous sub-core shows an area of solid body rotation, high axial velocity (sometimes its maximum can be as large as four or five times the free stream velocity [16]), low total pressure and high dissipation, due to the steep gradient in the cross flow components. Figure 2.4 [14] indicates this cross sectional structure of leading edge primary vortex.

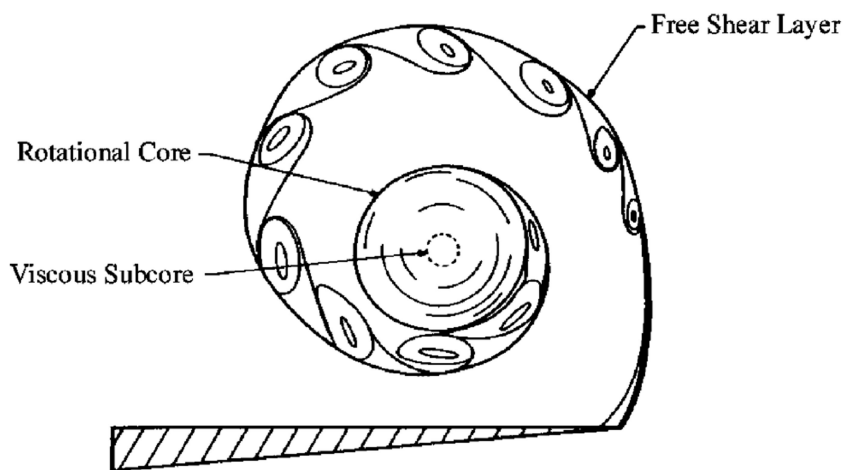


Figure 2.4 Cross sectional structure of leading edge primary vortex [14]

Underneath the primary vortex on the wing upper side an attached flow, having outboard direction, is established. The attachment line of the primary vortex lies even at its center line or at some span wise position between the center line and the leading edge, depending on the angle of attack [13]. Besides, the pressure increases from the suction peak, the center of the vortex, towards the leading-edge, resulting in a severe lateral pressure gradient. As a result of this fact, after having passed the suction peak underneath the primary vortex axis, the attached flow induces the boundary layer to separate and form an additional (secondary) vortex rotating in the counter sense of the primary one. Under certain circumstances this secondary vortex may lead to yet another adverse pressure gradient and a tertiary vortex [1]. On the contrary of the swirling shear layer, the underlying cause of these additional vortices

is viscous-dominated and the presence of a laminar or turbulent boundary layer strongly affects the formation of these vortices [13].

The axial velocity increment over the wing upper surface, resulting from leading edge vortices, leads to a high suction level, with the local pressure minima indicating the track of the vortex axis on the wing surface. Consequently, fully developed and stable stage leading edge vortices produce additional lift, maintain an increase in maximum angle of attack and significantly improve maneuver capabilities of aircrafts [12].

As increasing the angle of attack the leading edge vortices reach a full separated condition from the upper wing surface and get stronger till a certain extent. Further increments in the angle of attack causes the vortices undergo a sudden expansion and disorganization which is termed “breakdown” or “burst” in the literature. The axial core flow inside the vortex stagnates due to the adverse pressure gradient when raising the angle of attack and this yields the vortex to burst [12, 17, 18]. As can be seen from Figure 2.5 [12] the jet-type core flow of the vortex changes to a wake-type flow leading to extremely high turbulence intensities at the breakdown position. As a result, the vortex core expands rapidly accompanied by high velocity fluctuations. The breakdown position moves even upstream with increasing the angle of attack. It should also be noted that the position of the breakdown is not stationary even for a stationary model. It typically oscillates unsteadily about some mean position [19]. Breakdown of the leading edge vortices results in severe limitations on the performance of the aircraft by effecting the aerodynamic forces and moments immediately.

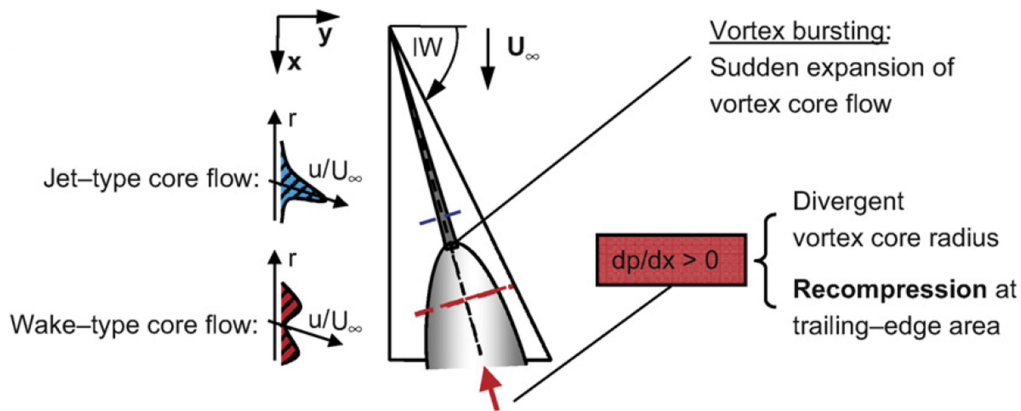


Figure 2.5 Change of the core flow from a jet-type to a wake-type [12]

2.2 Flow Asymmetry, Shear Layer Instabilities and Vortex Wandering

The interaction between the two counter rotating leading edge vortices on both boards of the wing (left and right) gets stronger with increasing angle of attack and leading edge sweep, leading to flow asymmetry. This phenomenon becomes more severe when vortex breakdown takes place and yields a sudden and early onset of the breakdown on one side with a higher sensitivity of the core expansion [11].

Another important aspect of the vortical flow is about the shear layer or the feeding sheet which surrounds the primary vortex. This layer may exhibit various forms of instability giving rise to vortical sub-structures wrapping around the leading edge vortex. Figure 2.6 [20] shows visibly the vortical sub structures in the shear layer as well as the asymmetric expanding vortex cores without breakdown on a laser light sheet visualization of the leading-edge vortices at different chord wise stations above an 85° swept delta wing. Gad-el-Hak and Blackwelder [21] observed the vortex sheet emanating from the leading edge rolls up periodically in to discrete vortical sub-structures which undergo a pairing process in their flow visualizations done with low Re and they attributed this phenomenon to the inviscid and unsteady Kelvin-Helmholtz (K-H) type instability. They also reported to be able to observe these vortical sub-structures in another experimental measurement done with much higher Re [22]. As one investigates the shear layer in two-dimensions, the K-H instability can be seen a generic part of the vortical flow over the wing. However, another

explanation for the sourcing of the shear layer unsteadiness and roll up says that the vortex/surface interaction and boundary layer separation can play a major role on formation of the sub-structures [23]. Besides, even the shear layer instabilities are mostly considered to be an unsteady phenomenon, some researchers revealed the existence of stationary small-scale vortices in the periphery of the primary vortex core [24, 25]. It was confirmed that the steady and unsteady sub-structures seen in the shear layer are not necessarily two distinct phenomena [16].

Although the free stream flow can be steady and the delta wing is in a stationary condition, the primary vortices occurring over it has inherent unsteady features like what is mentioned above. Another prominent one of these features is that the wandering location of the vortex core. Menke and Gursul [26] observed large-amplitude and broadband random velocity fluctuations taking place upstream of the breakdown and also in the absence of the breakdown over slender wings. It was suggested that these fluctuations can be associated to the random displacement of the vortex core [16]. The origin of vortex wandering has been thought to have some several reasons. K-H instabilities existing in the separated shear layer, nonlinear interactions of small vortices with primary vortex and the unsteady turbulent flow in the wake of the wing are mainly discussed as the possible sources of this phenomenon.



Figure 2.6 Vortical sub structures in the shear layer and asymmetric expanding vortex cores without breakdown [20]

2.3 Effect of Leading Edge Bluntness

Although the above mentioned general features of vortical flow can be said to be common for sharp and rounded (blunt) leading edge wings, there are some important differences worth to be emphasized. For sharp leading edges, primary separation is fixed and it is located at the leading edge itself. Besides, the development of the leading-edge vortex is only little influenced by Reynolds number effects. However, the vortex aerodynamics gets complicated for blunt leading edges and quite differs from the sharp-edged case in at least two regards. [27]. First, the position of the separation line is free to move along the edge. For low to moderate angles of attack, flow could be fully attached on rounded edged wings. The leading edge separation first occurs at the wing rear part and then it progresses up through the leading edge with increasing angle of attack. Actually the onset and progression of this separation depends both the leading edge bluntness and the flow conditions. The separation position for the rounded leading edges is determined by the pressure gradient and the

boundary layer development [13]. Additionally, the separation at any station occurs from a smooth surface close to the leading edge but not necessarily precisely at the leading edge as it is the case for sharp edge [28]. Secondly, an inner and co-rotating vortex is present for rounded edged wings for certain Reynolds numbers and moderate angle of attacks range [8]. There exists a laminar separation near the apex close to the mid-span of the wing and downstream of that a small inner vortex is formed by the inboard separated flows. It is basically favored by the positive lateral pressure gradient sourced by the primary leading edge vortex and it rotates at the same direction with the primary leading edge vortex. The trajectory and strength of the inner vortex depend on the angle of attack (strength of the leading edge vortex) and Reynolds number (area of laminar flow) [8]. Figure 2.7. [29] shows details of a sample dual vortex system for a rounded edged wing.

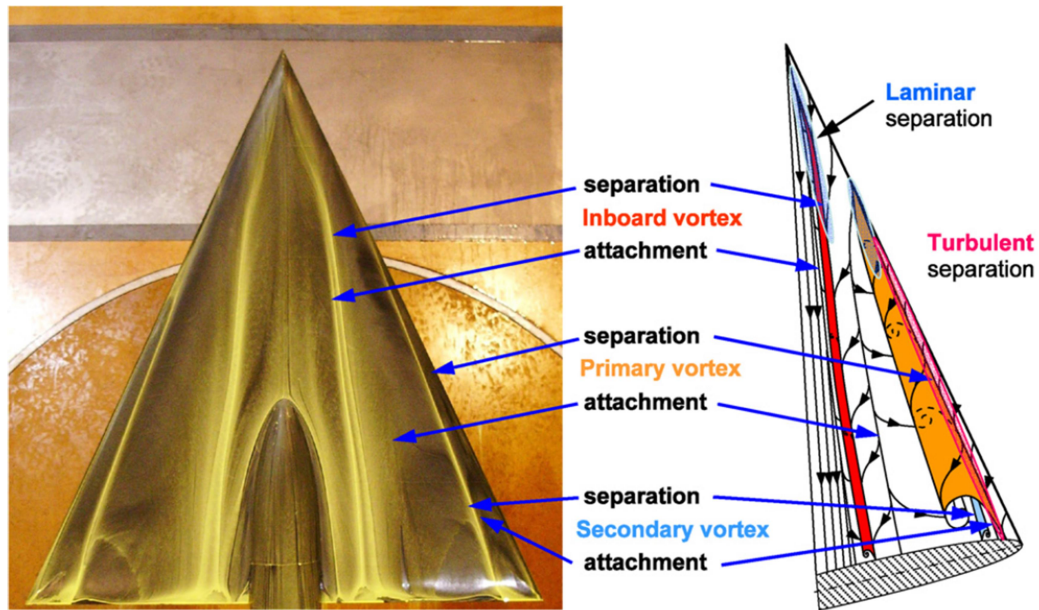


Figure 2.7 Oil flow visualization and vortex system for rounded leading edge [29]

The complexity of flow physics for the rounded edge configurations can have significant impact on the performance and maneuver aerodynamics of high swept wings [28]. Consequently, even though angle of attack, Mach number, Reynolds number and leading edge radius are the main parameters those determine the onset of the vortex as well as its position and strength for blunt leading edges, the angle of

attack is the sole main parameter for sharp leading edges [30]. The effects of bluntness on leading edge vortex structures are given in Figure 2.8 [28].

One of the most important efforts to investigate the bluntness effects on vortical flow aerodynamics over a slender delta wing was Vortex Flow Experiment-2 which was organized by NATO Research and Technology Organization (RTO) between 2003 and 2008. In scope of this experiment, numbers of experimental and numerical studies were performed by researchers from different NATO countries [3, 31]. A common wing configuration was used in these studies. The wing had a 65° degree sweep angle and was originally produced and used by NASA in 1996 by Chu and Luckring [4] with sharp as well as rounded leading edges for experimental measurements. In this thesis study, the same wing model with only the sharp leading edge configuration was selected to investigate.

Sharp leading edge

Blunt leading edge

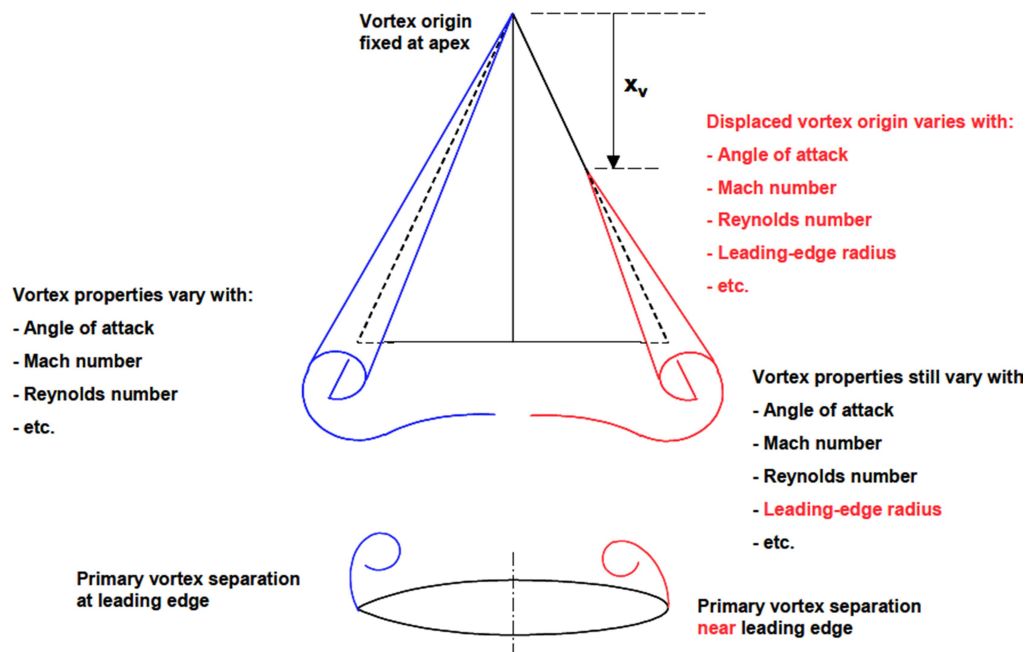


Figure 2.8 The effects of bluntness on leading edge vortex structures [28]

2.4 Breakdown of the Leading Edge Vortices

The bursting process of leading edge vortices on slender delta wings can be abbreviated as that the slowly evolving rotating flow expands suddenly into a highly fluctuating structure in which the swirling and longitudinal velocities are drastically reduced in the central part of this structure [2]. This is a complex phenomenon and the structure of the breakdown and the newly adopted flow after it are matters of controversy among scientists. Despite this fact, in practical aeronautical situations it is commonly accepted that when the vortical structure rapidly expands (breakdowns), a reversed axial flow occurs in the core region and large-scale velocity fluctuations are observed in the wake after the breakdown location. Besides, the highly dissipative region swells and forms a viscous recirculation region. This brings the effect of an obstacle for the vortex and enhances dissipating losses, yielding an ultimate collapse for the vortical structure.

The phenomenon was first observed by Werle [32] during a water tunnel experiment in 1954. Peckham and Atkinson [33] are, on the other hand, the first to observe it on a delta wing in 1957, confirming Werle's work. The basic classification of the types of the phenomenon, which is widely agreed now, was first done by Lambourne and Brayer in 1962 [17]. According to their investigation two types of breakdown for vortices generated by leading edges of a delta wing could be encountered. These were reported as bubble and spiral type and clearly revealed by Figure 2.9 [17].

In the bubble type breakdown, an oval shape recirculation zone forms up after the vortex core stagnates. The upstream half of the bubble is nearly axisymmetric with the flow smoothly passing around it, on the other hand the downstream half is open with irregular flow shedding from the bubble's aft end forming a turbulent wake like happening right after a blunt solid body [10]. The spiral mode is however represents a rapid deceleration of the vortex core flow first, then followed by its abrupt kink to take the form of a spiral. This spiraling core persists for one or two more turns before breaking in to large scale turbulence [10]. For leading edge vortices, the spiral also rotates and its rotation direction is in the same direction with the upstream vortex while the sense of the spiral is in opposite direction. Figure 2.10 [17] illustrates the spiral type of the breakdown process.

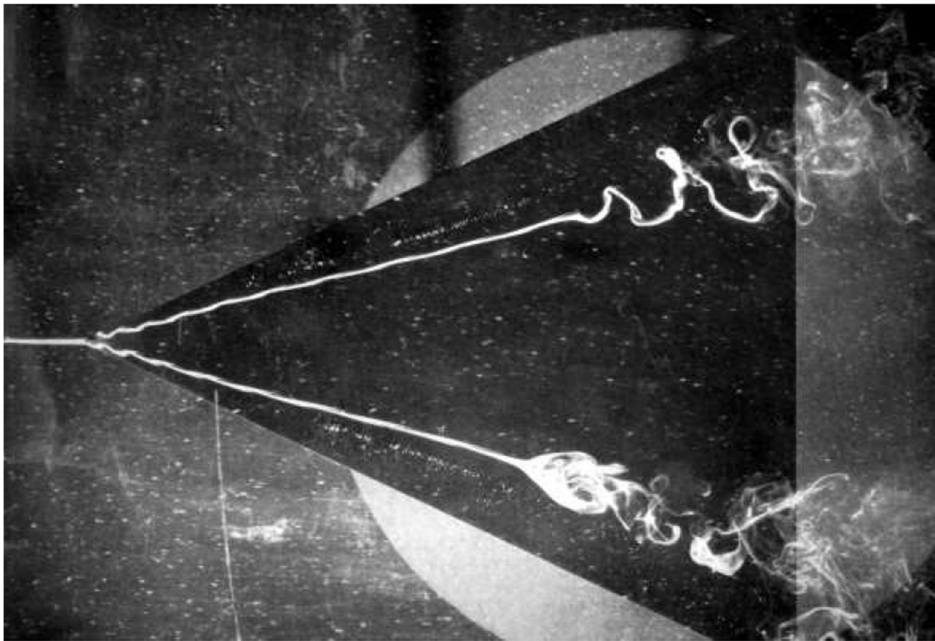


Figure 2.9 Bubble and spiral type vortex breakdown [17]

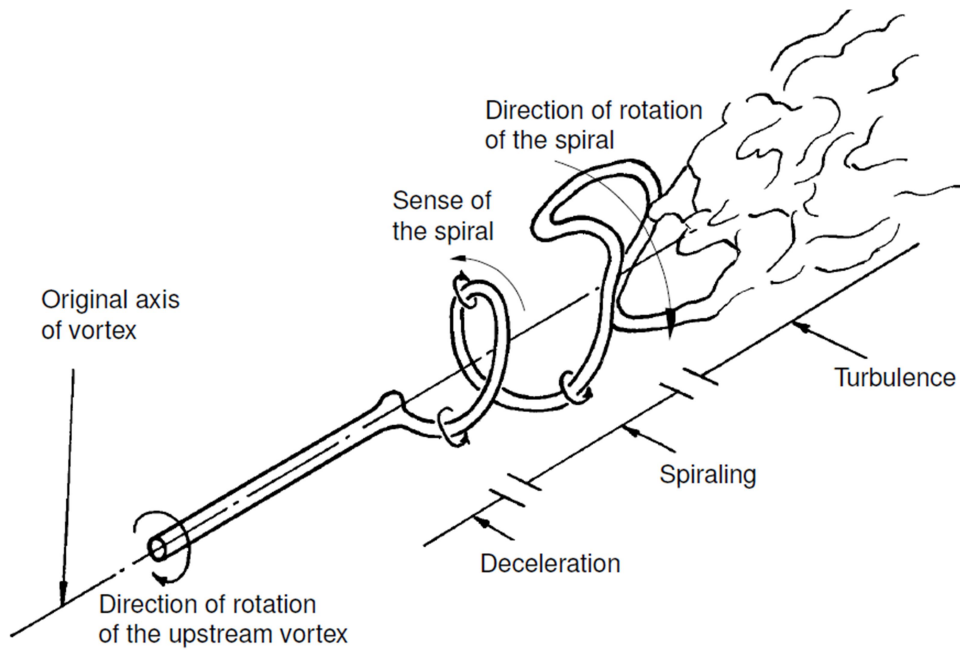


Figure 2.10 Process of spiral type vortex breakdown [17]

After many researches on the burst types of the leading edge vortices it was suggested that the spiral type is more common over delta wings and in fact occasionally even the bubble type breakdown switches to spiral mode in experiments [16].

The sensitivity of the location of vortex breakdown to number of parameters brings another challenge to researchers. The location for the breakdown in slender delta wings basically depends on a combination of sweep angle and incidence [10]. However going in to detail the problem gets complicated. Besides the effects of experimental set-up, the free stream turbulence and the shape of the leading edge, the inherent 3D unsteady nature of the vortical flow itself is an important factor for the oscillations of the vortex breakdown locations on both sides of the wing [11].

The mechanism of breakdown of the leading edge vortices is a quite complicated issue and is still one of the unresolved problems in aerodynamics [34]. There are number of theories for vortex breakdown, however at this time none of these has been widely accepted [14]. Wave propagation is the widely accepted mechanism in order to explain the process that yields the burst of the leading edge vortices [16]. Increasing the angle of attack and adverse pressure gradient in the near wake developed as a consequence of it, drives the flow toward criticality leading to trapping, amplification and upstream movement of axisymmetric waves [11]. On the other hand, the conditions for the breakdown onset have been much well-identified throughout the years by the help of numerous both experimental and numerical efforts.

Except very low values, well below any practical value, the Reynolds number rather weakly affects the vortex breakdown occurrence [3, 17]. Swirl level and adverse pressure gradient along the vortex axis are the two main parameters provoking the onset and movement of the leading edge the vortex breakdown and an increase in one of them promotes an earlier initiation of it [16]. The rate of the azimuthal (tangential) velocity to the axial velocity (introduced as swirl number previously) is the most determinant factor for breakdown onset. It cannot go beyond a critical value which is nearly 1.3 [3]. It was also stated by Lee and Ho [35] that only when the

convection of vorticity along the core axis balances the vorticity generation from the boundary layer of the leading edge, a stationary leading-edge vortex can be achieved; and swirl or helix angle, the arctangent of the swirl number, is an important indicator of this balance [36, 37] and which cannot exceed a value approximately 50° [38]. When external circumstances cause the swirl number or angle to exceed the critical values, then the breakdown takes place. Another parameter that can be said to be a key factor for the breakdown initiation is the adverse pressure gradient that the vortical flow subjects to. Rising pressure downstream causes the axial velocity component to retard and the axial vorticity convection to reduce following an increase in the swirl number till the critical value and burst of the vortex [14, 3].

Another explanation for the vortex breakdown phenomenon was done by Lopez [39] and Brown and Lopez [40]. They showed that a change in sign of the azimuthal vorticity upstream is a necessary condition for the initiation of vortex breakdown. Figure 2.11 [41] gives clearly the directions and senses of vorticity components. It can be seen from figure that the velocity that opposes the axial flow generates a negative sense of azimuthal vorticity. Since this fact, the deceleration of the axial velocity may be linked to the negative azimuthal vorticity and at a certain extend this can cause a recirculation region to form and eventually the vortex to burst. Figure 2.12 [11] presents azimuthal vorticity contours and sectional streamlines generated numerically on a vertical plane containing the vortex axis. Three dimensional critical points (i.e. the points where all the velocity components vanish) are also visible by black solid circles. This figure clearly reveals the change of the sign of azimuthal vorticity at the breakdown region and also the helical instabilities occurring in the bubble first and eventually lead to a spiral type breakdown.

Even the progression of the onset of the breakdown towards the apex with increasing the incident is again a complex phenomenon and associated with certain characteristics like the geometry and flow conditions, it can be called a valid generalization. However, when the angle of attack exceeds the one that causes the vortices to burst at the wing apex location, the shear layer separated from the leading edges cannot generate swirling flow that will have axial motion over the wing. This time vortex shedding will take place instead [42].

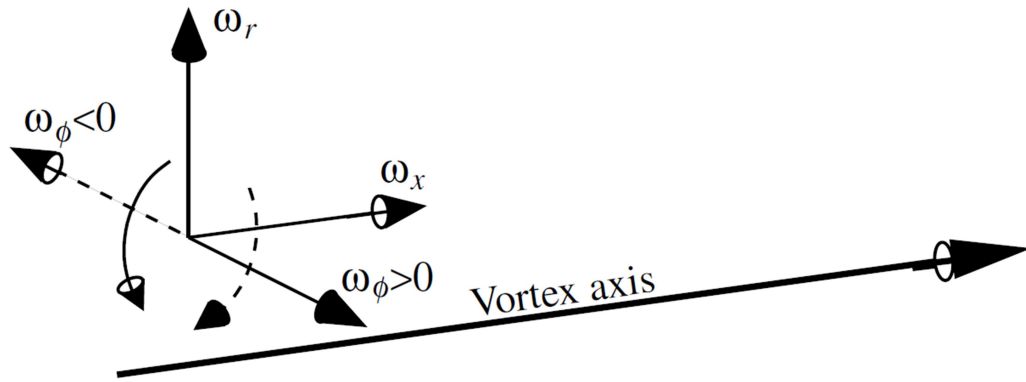


Figure 2.11 The vorticity components for a vortex and their senses [41]

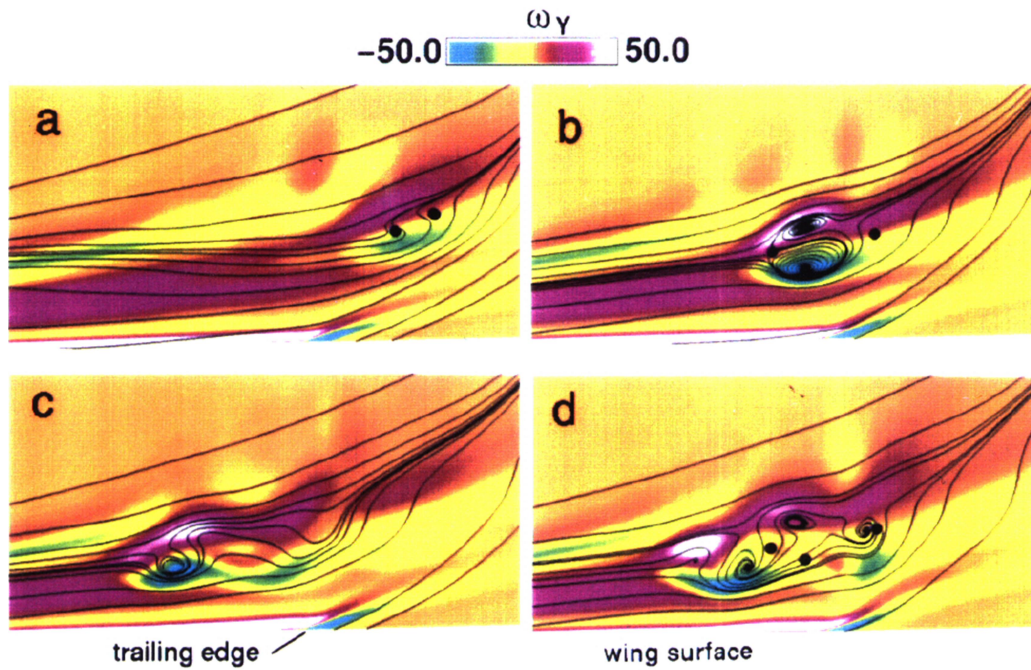


Figure 2.12 Azimuthal vorticity contours and sectional streamlines generated numerically on a vertical plane containing the vortex axis [11]

2.5 Control of Vortical Flow Over Delta Wings

Since the breakdown of leading edge vortices on a delta wing brings mostly unwanted consequences, aerodynamicists have long been devoted great amount of work to control the vortical flow to either avoid or delay the burst of the vortices. In order to manipulate the vortex breakdown location over high swept wings at high angle of attack, numerous flow control techniques have been employed and showed success at certain extent over the last 60 years. Despite this, none of these techniques has clearly demonstrated a superior efficiency or effectiveness in controlling either the vortical flow structure or the vortex breakdown location [2]. On the other hand, each of these methods can be said to provide a specific solution for the control of the breakdown phenomenon of leading edge vortices, depending on the desired outcome.

Mainly the two parameters for the breakdown onset, swirl ratio and pressure gradient over the wing, are manipulated in current control applications [2]. One can simply state that the breakdown of vortices is closely related to swirl level and any measure taken for slowing down the azimuthal (tangential) velocity component or to augment the axial velocity component will have a stabilizing effect and delay vortex breakdown. This action basically targets to stabilize and strengthen the vortex to adverse effects by injecting stream wise momentum into it. One can also tend to tailor the pressure field downstream of the wing aiming to prevent the adverse pressure gradient occurring at the rear parts of the wing, since an adverse pressure gradient can cause vortex breakdown. However, in this case the whole aerodynamic field downstream of the vehicle must be manipulated.

When compared to one another, since the pre-conditions of breakdown are relatively well clarified, a local action towards decreasing the swirl number in a manner previously mentioned is far more effective. However, the leading edge vortex structures are generally far from the originating surface and it is not easy to apply control actions precisely in the flow field. Due to this fact manipulating a boundary layer that is attached to the surface of the wing is found to be a much easier way by researchers. [2].

Generally the means for flow control activities of leading edge vortices and their breakdown are split into two broad categories as being passive and active. In passive techniques mechanical devices such as forebodies, strakes and canards are used in combination with the main wing to generate multiple-vortex systems. The vortices originating from upstream or developed downstream energize the vortical flow on the main wing by interacting it and delay the vortex breakdown and stall. Multiple vortex systems can also be seen taking place in canard-wing and tandem delta wing configurations. Figure 2.13 [43] presents a tandem delta wing configuration and corresponding breakdown location shift with varying angle of attack. One of the more recent phenomena for passive control employs the interaction of controlled structural oscillations of an elastic wing with the shear layer instabilities and it appears mostly a feature of non-slender wings [43]. This interaction mainly supports the reattachment of the flow and leads to an increase in lift [44].

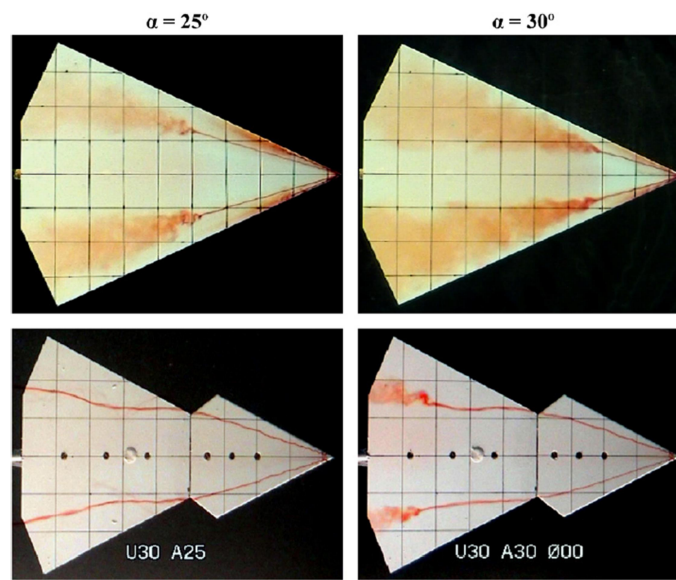


Figure 2.13 Flow control with tandem delta wing configuration [43]

Active flow control techniques can be divided into three groups as being control surfaces, plasma actuators, and blowing or suction via pneumatic devices. Leading edge flaps and extensions or apex fences are used to change mainly the angle of attack or sweep angle and also to effect the flow separation both at the leading edge and apex of the wing in order to manipulate the formation, location and strength of

the vortical flow that inherently results in a change in breakdown location. Figure 2.14. [43] gives examples for leading edge flaps and extensions. Figure 2.15 [45] on the other hand, is a prominent example for the application of plasma actuators conducted on a slender wing by Visbal and Gaitonde [45]. As clearly be seen from this figure, the breakdown was completely prevented and the jet flow at the core was retained by the effect of the wall-jet originated from plasma actuators near the apex.

The main stream of active flow control can easily be said using pneumatic devices for suction or blowing which include the applications of span wise blowing, tangential blowing, leading-edge blowing, along-the vortex core blowing, trailing-edge blowing, leeward surface suction, leading-edge suction, suction along the vortex core [2]. In Figure 2.16 [46] a trailing edge jet blowing effect on the delay of vortex breakdown, which is caused by the adverse pressure gradient induced by the fin structure, is revealed. In this application the pressure field downstream of the wings was tailored to manipulate the pressure gradient over the wing.

The main purpose for the active control applications employing pneumatic devices is to manage it with less amount of energy requirement as possible. That can be called the effectiveness of that particular method. Although each particular method can be prominent for a specific case and desired control outcome, a general effectiveness assessment can be made on them and concluded as in Figure 2.17 [43]. Here C_μ is the momentum coefficient, which is a non-dimensional coefficient to describe the mass flow rate of the blowing or suction, c is the chord length and ΔX_{bd} is the difference between breakdown locations of controlled and uncontrolled cases.

Independent of the type of flow control, another classification for all manipulation methods can be made as being steady and unsteady. The unsteady excitation methods can be grouped as low-frequency and high-frequency ones. The high frequency methods mainly aspire to manipulate the instabilities sourced by vortex. Low frequency types, on the other hand, aim to control the axial pressure gradient and so to influence the breakdown behavior [44].

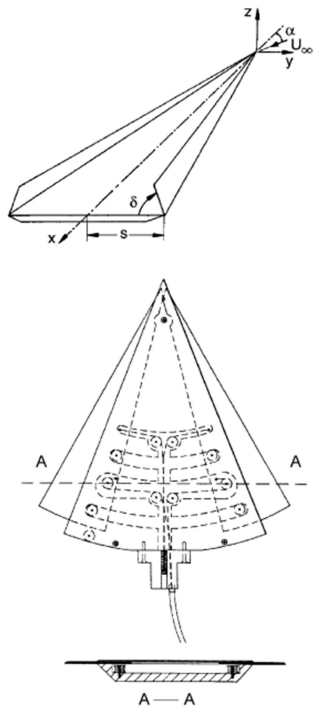


Figure 2.14 Examples for leading edge flaps and extensions [43]

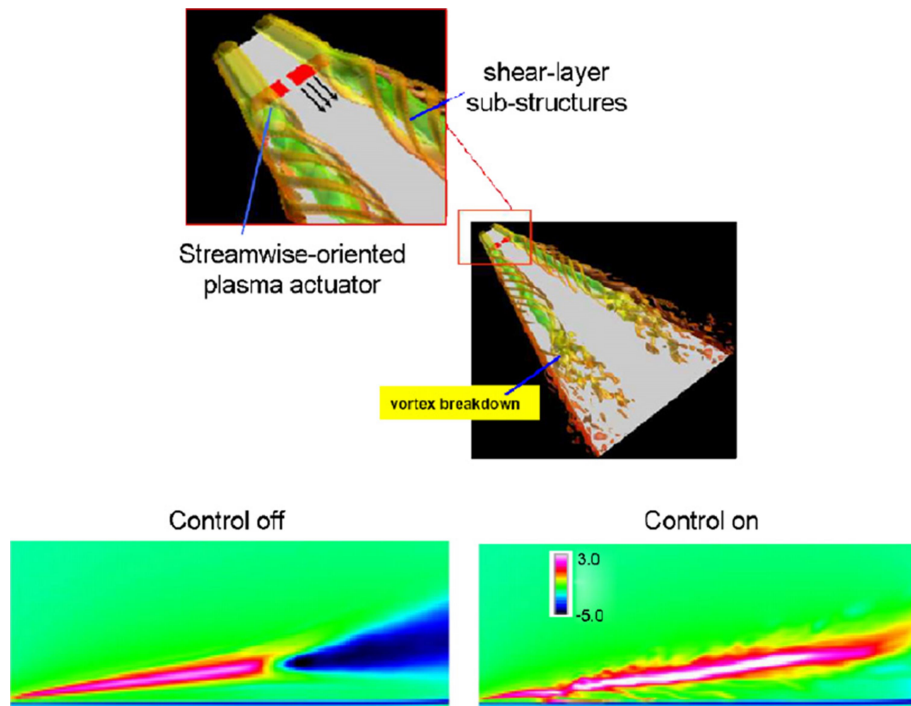


Figure 2.15 Plasma actuator control conducted on a slender wing [45]

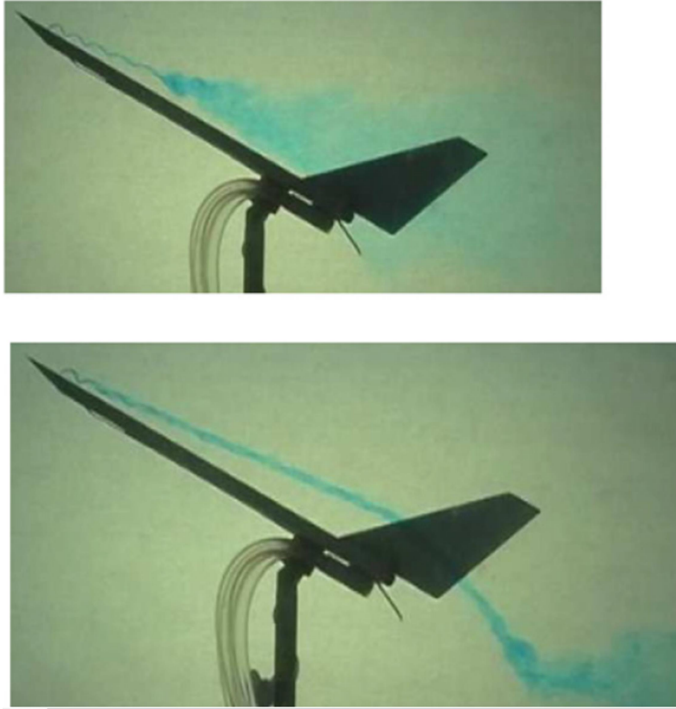


Figure 2.16 Avoiding of vortex breakdown with trailing edge jet blowing [46]

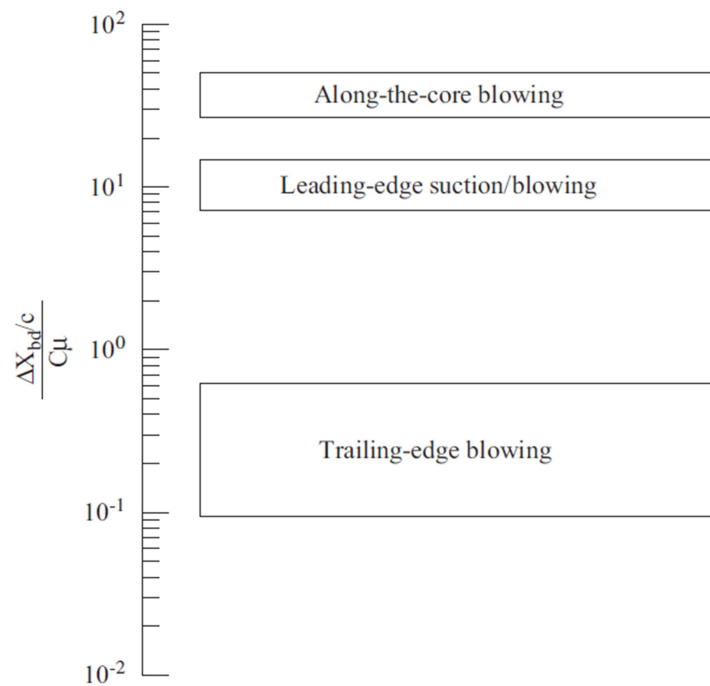


Figure 2.17 General effectiveness assessments of pneumatic control techniques [43]

The occurrence of vortex breakdown can be related to dramatic expansion of the flow structure inherently induced by the amplifications of instable disturbances. That is why; introducing well defined perturbations into the flow field by unsteady methods can put forward efficient results in controlling the breakdown phenomenon. Various researchers reported that they could manage to control the phenomenon with a much higher efficiency than continuous techniques by first achieving a significant control effect with an unsteady pulsating action and then carefully adjusting its frequency to coincide with the natural frequency (eigen-frequencies) of the vortex instabilities addressed [2]. Besides, control surface application as the oscillation of flaps with small deflection angles also found to be more effective than its steady counterpart [43]. The difference between the effectiveness of steady and unsteady blowing techniques can be understood by looking at Figure 2.18 [43]. C_μ is again momentum coefficient and ΔC_N is the difference of normal-force coefficients of controlled and uncontrolled cases for the figure.

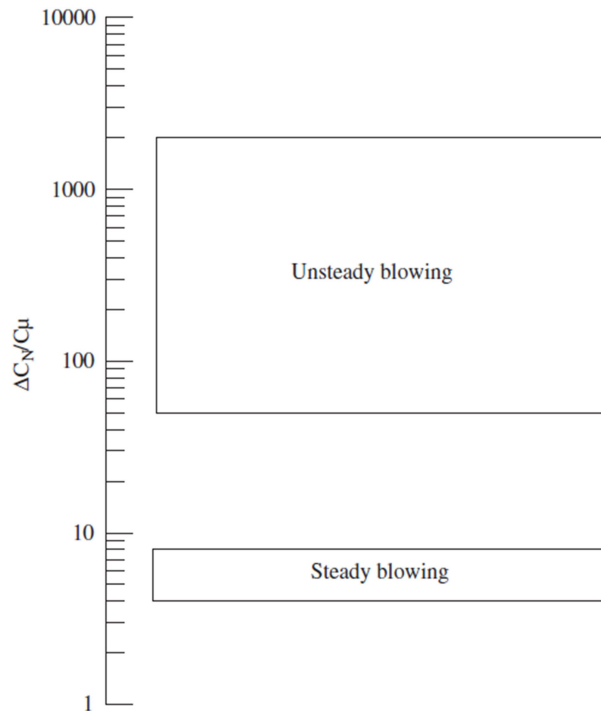


Figure 2.18 Effectiveness comparison of steady and unsteady blowing [43]

As can be clearly understood by the definitions above, the main difficulty for periodic pulsating techniques is, to first identify the characteristic frequencies in the vortical structure and then to assign the right place and intensity of the control action. Other particular aspects of vortex breakdown phenomenon like oscillations of the breakdown locations also cause major obstacles to overcome for successful implementation of the control action. Sometimes it could be extremely difficult to quantify the exact location of the breakdown with steady approaches and so that researchers acquires unsteady measurements or calculations for the purpose.

The interpretation of the breakdown phenomenon is still a matter of controversy and mostly lack of exact information about the location of onset of the flow separation at the origin of the vortex and precise spatial vortex position make the control efforts quite difficult [2]. This insufficient knowledge about the vortical flow field and inability for accurate prediction of vortex breakdown can be attributed to the often poor effectiveness of flow control methods [2].

Bearing in mind that the great number of studies in the literature dedicated to the breakdown control activities and their relative success, it will be required to improve the predictive capacities of both experimental and numerical techniques which aim to clearly demonstrate the physics of the phenomenon. Besides, the mass flow rate and/or energy requirement for an effective manipulation of the flow around a full-scale aircraft needs further studies to be correctly identified [2].

CHAPTER 3

COMPUTATIONAL MODELING

3.1 Wing Modeling

As previously mentioned, the wing which was utilized in VFE-2 was originally produced and tested by NASA in Langley Research Center's (LRC) facilities in 1996. Chu and Luckring presented all the details of the wing, experimental setup and measurement results for different leading edge configurations performed across a wide range of Reynolds and Mach numbers in their reports [4]. The wing has a 65° sweep angle. It comprises of a flat triangle plate in the middle, a trailing edge closure and interchangeable leading edges which can be adapted to the sides of the flat plate. These leading edges have four different types as to be one sharp and three rounded. They are classified in terms of their closure radius which are normalized by the mean aerodynamic chord and having values of 0, 0.05, 0.15, and 0.30 percent, respectively. Rounded leading edges are also called as small, medium and large radius corresponding to these values. Inside the tunnel's test section the wing was supported by a sting system which holds the wing up to nearly $x/C = 0.6$. In Figure 3.1, model details are presented on a half wing configuration.

The downstream continuation of the sting in the near field of the wing is called as fore-sting. In this study, the fore-sting was modeled up to position $x/C = 1.758$ as it was recommended by Chu and Luckring [4]. Details of this portion of the sting can be found in Figure 3.2.

As previously mentioned, one of the main purposes of the VFE-2 was to investigate the effect of the leading edge bluntness to the vortical flow field. That is why, as Chu and Luckring did in LRC, both sharp and rounded (medium radius) leading edges were tested in VFE-2. In this study, sharp leading edge configuration was selected for simulating the flow passing by. In Figure 3.3 three-view of the full VFE-2 wing

with the interrelations of the dimensions are provided as well as the sharp and medium radius leading edge contours [47].

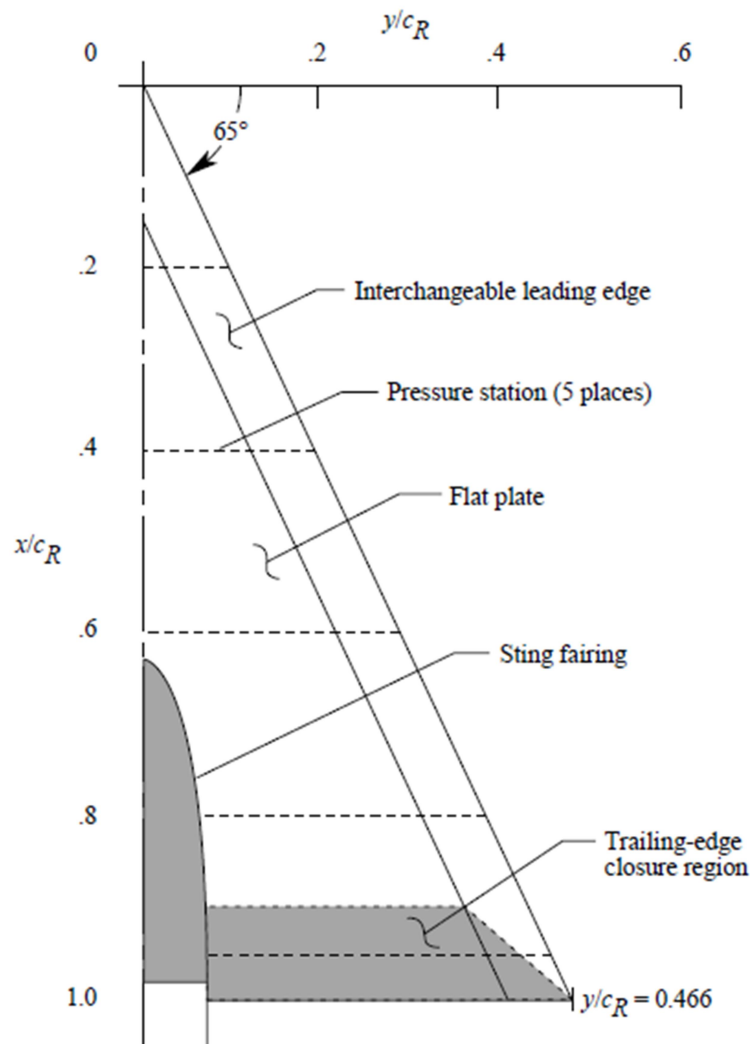


Figure 3.1 VFE-2 wing model details [4]

Figure 3.4 shows the functions which define the contours of leading edge and semi-thickness of the wing. All analytical expressions and related parameters of these functions were also given in [4]. Utilizing all data mentioned above for sharp leading edge configuration, a metric 3D model of the wing was generated in Solidworks. The isometric views of the model are presented in Figure 3.5. Throughout this study, the origin of the coordinates and names of its axes are as they are presented in Figure 3.5.

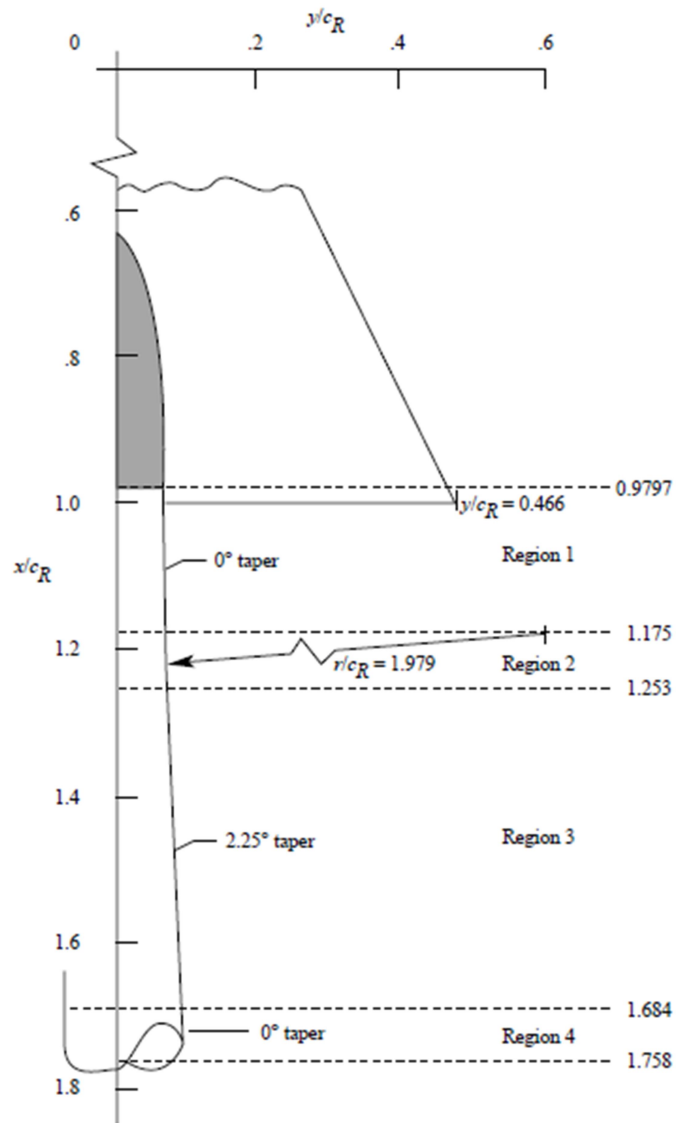


Figure 3.2 Fore-sting details [4]

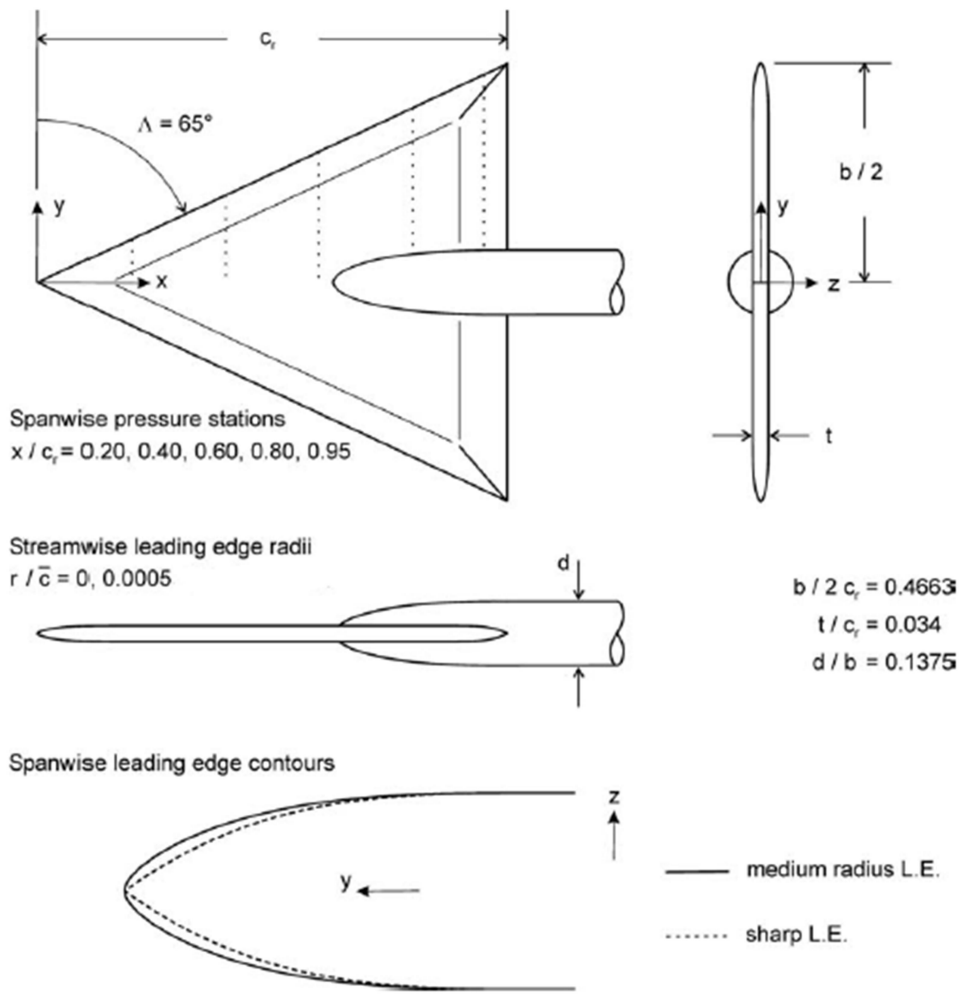


Figure 3.3 VFE-2 wing three-view drawing and sharp vs. rounded edges [47]

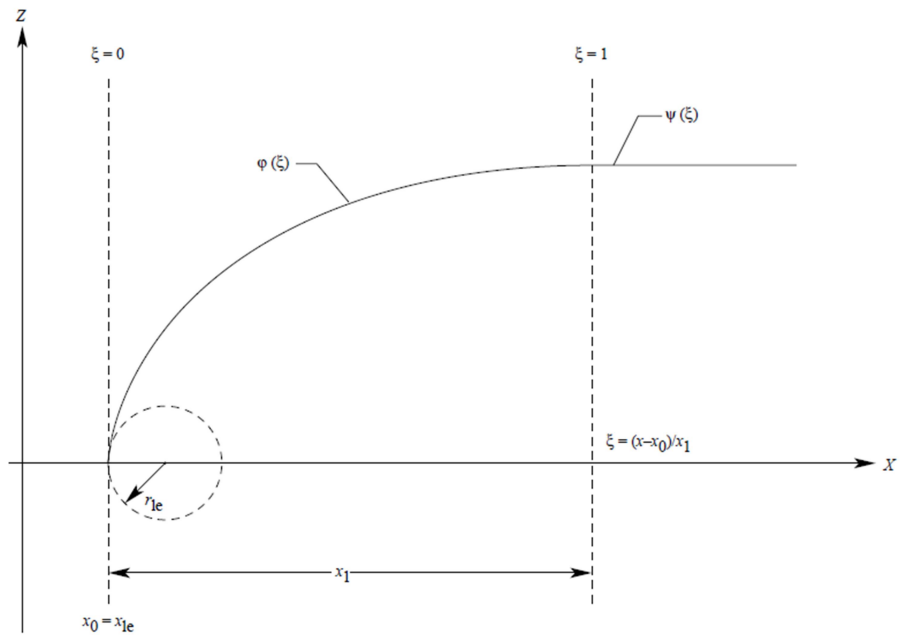


Figure 3.4 Functions representing the wing semithickness contours [4]

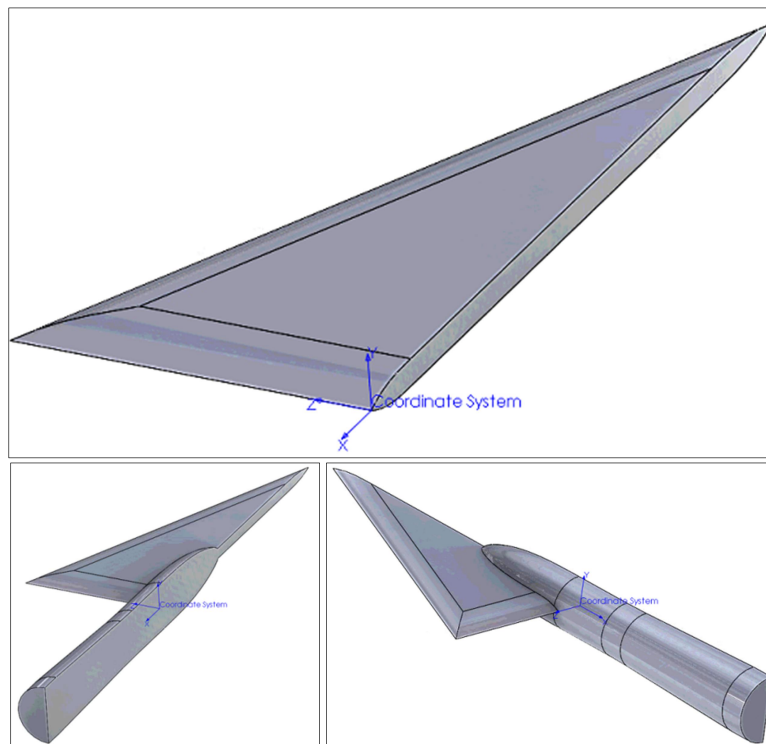


Figure 3.5 Isometric views of the 3D model built in Solidworks

3.2 Mesh Generation

The generated delta wing has a root chord of 0.98 m and its other main dimensions are given in Table 3.1. In order to analyze numerically the dynamics of air passing by wings, large computational domains are employed. This enables catching desired grid quality and quantities besides reducing the blockage effects of the wall boundaries on the flow. Reviewing the literature, researchers can be seen using different domain shapes and sizes for the mentioned purposes regarding their cases to model. For this study, a rectangular prism shaped domain, having the sizes of 20 x 15 x 5 m, was built. The wing was placed with 23° angle of attack inside the box as its root chord is on the global x-axis and its symmetry plane coincides with the symmetry plane of the domain. The blockage ratio is 0.2%, being considerably low. In Figure 3.6, the explicit orientation of the wing with the domain details is presented. Distances between the wing and the domain boundaries in terms of the root chord can be found in Table 3.2.

Domain discretization was done using ANSYS Meshing module. Unstructured patch conforming algorithm utilizing tetrahedron elements for volume mesh and triangular elements for the wing surfaces, was selected as the main method. Near wing volume grid has got a great importance in terms of resolving the flow field accurately. This fact brings out the necessity of refining the surface mesh of the wing on the suction side.

When going into the works in literature, in which the authors performed numerical analysis on the same wing type and similar flow conditions, it is found some grid refinement methods were employed for this purpose [1, 7]. These methods are derived based on empirical investigations on the performance of the mesh to resolve the flow phenomenon such as separations, vortices and their breakdown.

Surface mesh refinements in [1, 7] suggest conformably that, capturing the primary separation at the leading edge is the most critical aspect of the work to model vortical flow structure and the breakdown afterward, successfully. In accordance with this, the surface grid at the leading edge and the primary attachment location as well as at the other separation and attachment locations should be refined at its optimum.

Additionally, the inflation of the surface mesh must be carried out attentively. This is important for the laminar and turbulent boundary layers to be encompassed and finely resolved as well as the y^+ at wing surface to be kept at the desired value.

Table 3.1 Main dimensions of the wing

Wing Dimensions	
Root Chord Length	0.98 m
Mean Aerodynamic Chord (mac)	0.65 m
Max. Span	0.914 m
Max. Thickness	0.033 m

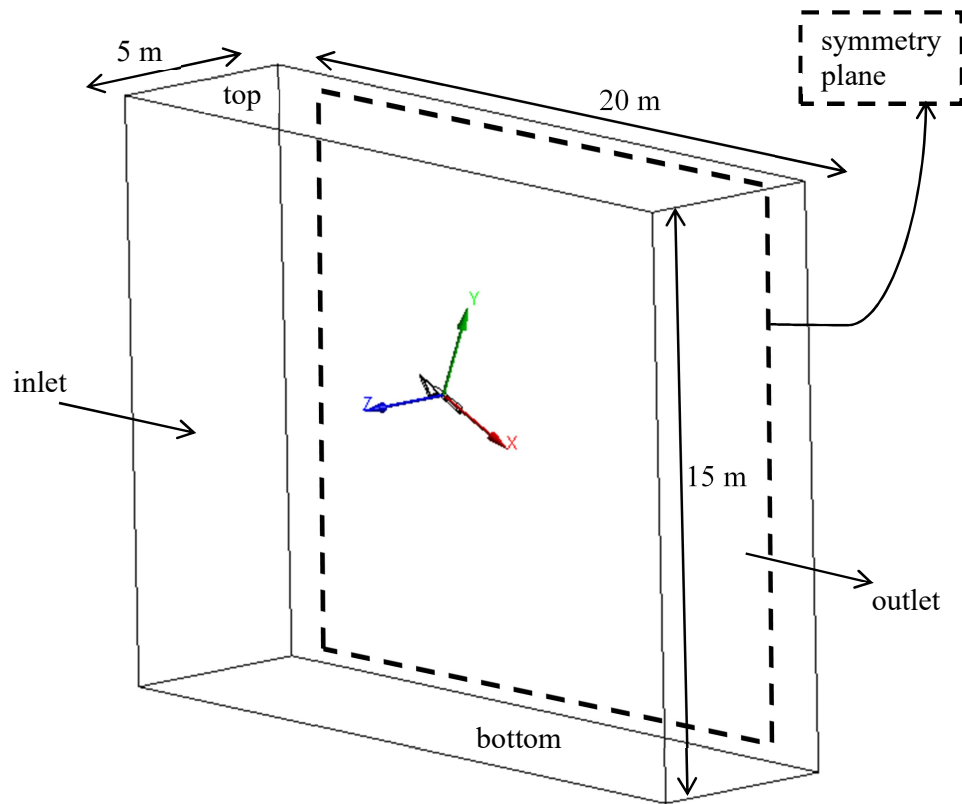


Figure 3.6 Computational domain

Table 3.2 Distance to chord ratios

Distances of the Wall Boundaries to the Coordinate Center		Distance to Chord Ratio
Top	7.5 m	7.7
Bottom	7.5 m	7.7
Inlet	6 m	6.1
Outlet	14 m	14.3
Side Wall	5 m	5.1

A surface meshing strategy was developed for the purposes above. This also allowed conducting a better-controlled grid independence work. According to this strategy, certain surface partitions of the suction (upper) side of the wing, besides the leading and trailing edges, were respected distinctly and meshed with different element sizes. Figure 3. 7 shows these surface portions and edges to be treated in particular. The surface mesh on the wing pressure (lower) side and the strut, however, was sized differently.

In addition to this, all the surface meshes were inflated as prismatic layers on the basis of a first layer thickness, layer number and growth rate. After large number of iterations, optimum values for the surface element sizes and inflation parameters were achieved. The quality of the mesh was also of a great concern. All global parameters were adjusted to obtain a well distributed and high quality mesh throughout the domain as well as close wing area.

The four resulting computational grids having overall element sizes of 2, 6, 10 and 15 Million, with the related meshing strategy settings, and their average quality values are given in Table 3.3 and Table 3.4, respectively.

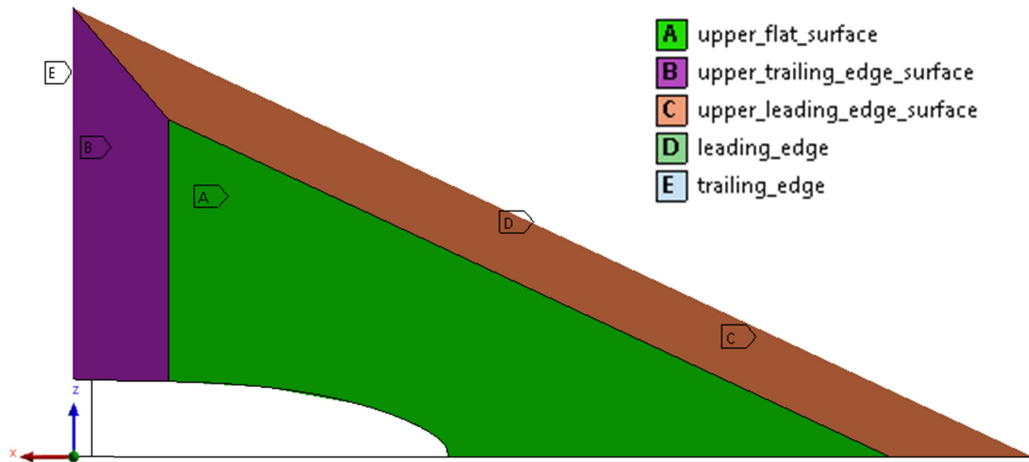


Figure 3.7 Surfaces and edges to be distinctly meshed with different element sizes

Table 3.3 Meshing strategy

	Mesh 1	Mesh 2	Mesh 3	Mesh 4
Element sizes (mm)				
Leading edge	3	1.05	0.645	0.459
Trailing edge	5	2.1	1.5	1.2
Upper flat surface	12.5	5.3	3.81	3
Upper leading edge surface	7.5	3.2	2.21	1.8
Upper trailing edge surface	10	5.8	3.01	2.4
Wing residue (lower surfaces and the strut)	18	6.9	4.91	3.8
Overall domain mesh sizes				
Number of Nodes	533.739	1.774.343	3.093.829	4.722.093
Number of Elements	2.001.854	6.009.680	10.074.492	15.000.074

Table 3.4 Mesh quality

	Mesh 1	Mesh 2	Mesh 3	Mesh 4
Average Skewness	0.23	0.22	0.21	0.21
Average Aspect Ratio	58.28	36.66	29.67	24.90

In Figure 3.8, the general view of the discretized solution domain can be seen. Sizes of the tetrahedral elements were kept smaller in the vicinity of the wing and larger at the outer regions, while inversely the number of them was. 27 prismatic inflation layers surrounding the wing are visible in Figure 3.9. The layers are covering a thickness of approximately 7 mm which is sufficient to capture the boundary layer which was observed in detail by Furman and Breitsamter in [8].

The four surface meshes, generated on the upper side of the wing using the strategy in Table 3.3, are provided in Figure 3.10. As previously mentioned, the concentration of the elements is much higher at the critical regions regarding the flow features. Being in line with this, side view of the near wing volume elements for the four distinct meshes are presented in Figure 3.11.

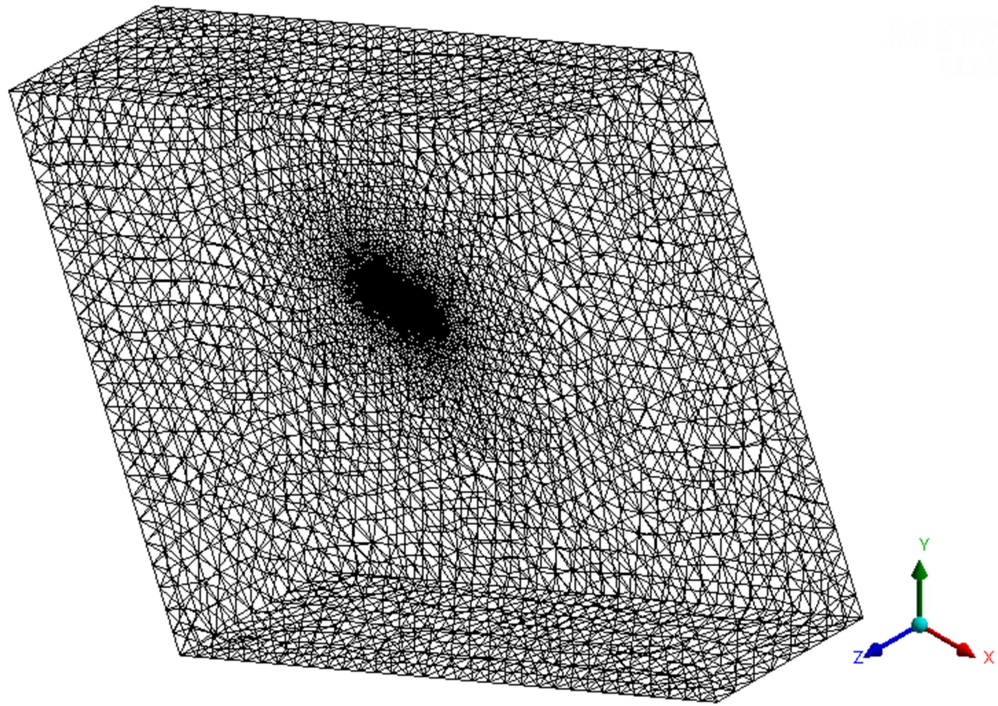


Figure 3.8 General view of overall meshed domain

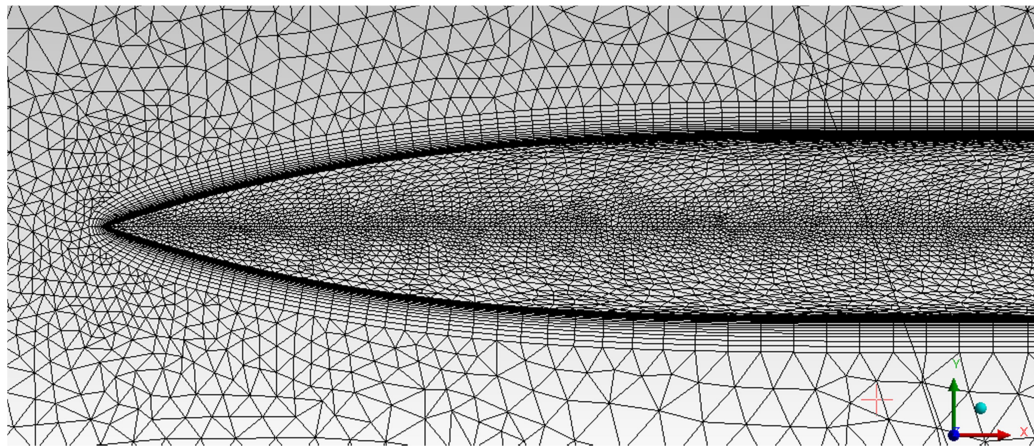


Figure 3.9 Inflated surface mesh around the wing

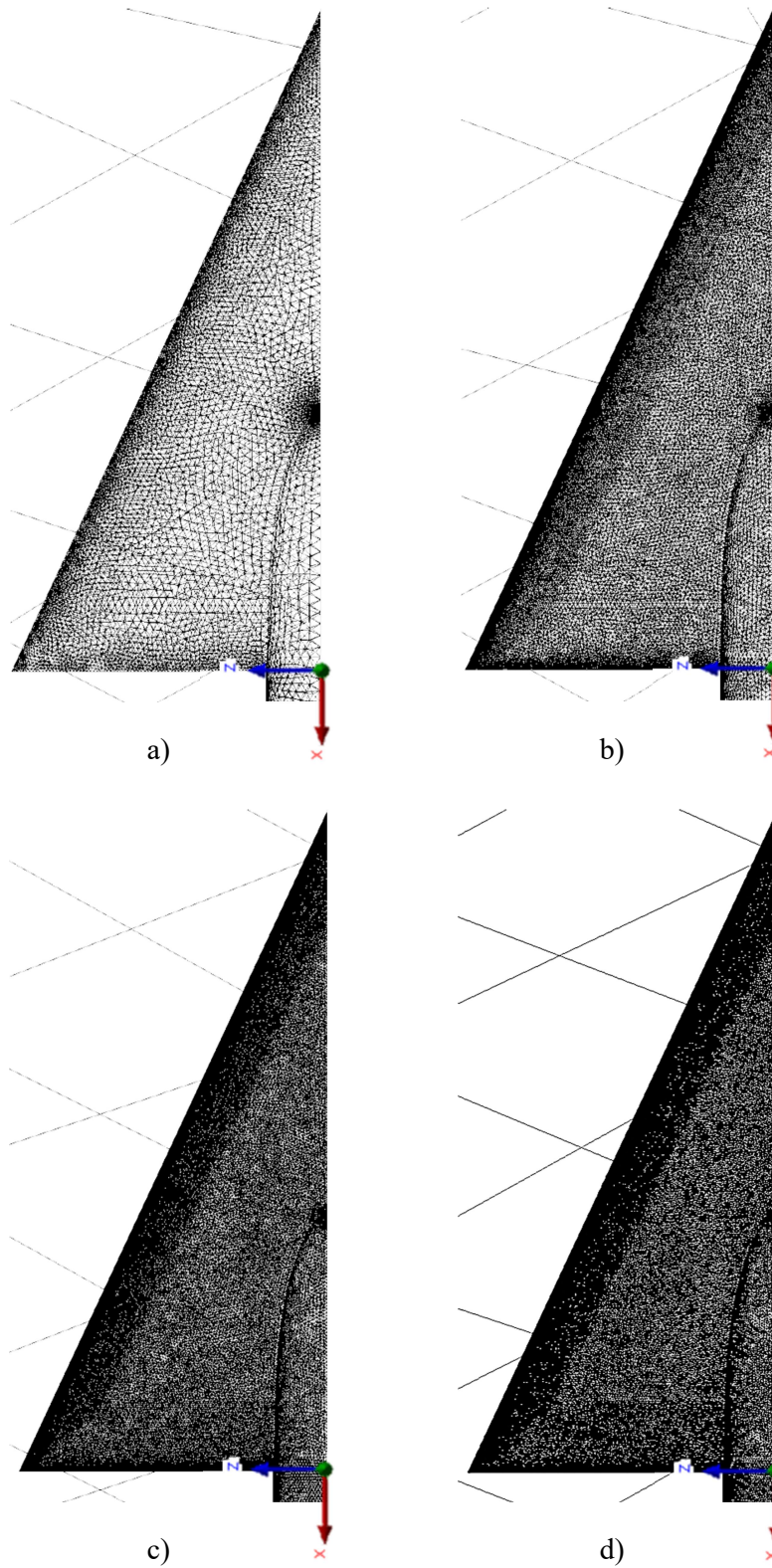
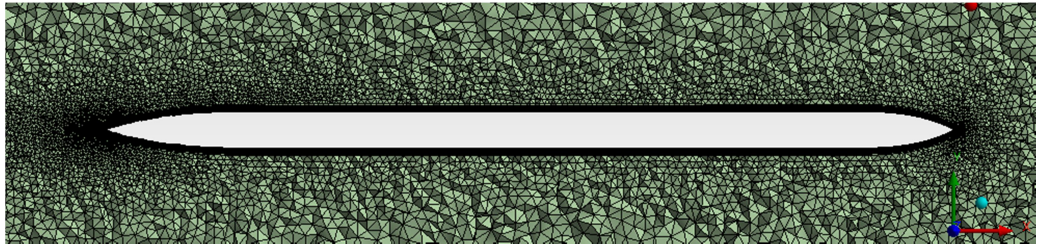


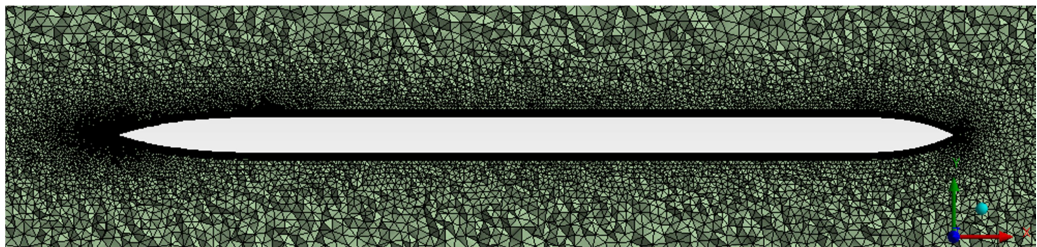
Figure 3.10 Surface meshes: a) Mesh 1, b) Mesh 2, c) Mesh 3, and d) Mesh 4



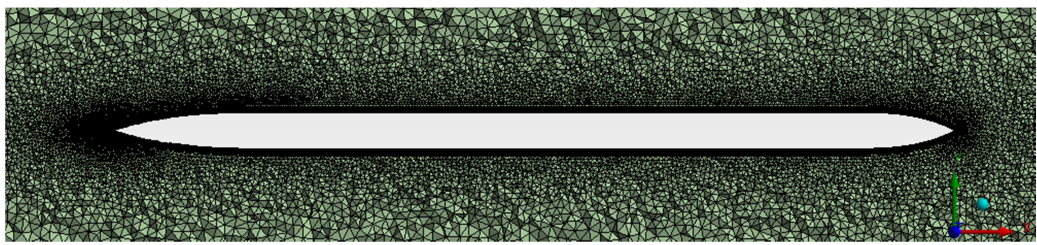
a)



b)



c)



d)

Figure 3.11 Near wing volume meshes: a) Mesh 1, b) Mesh 2, c) Mesh 3 and d) Mesh 4

3.3 Governing Equations and Turbulence Models

There are many choices for computational modeling of turbulence and each of them has a tradeoff in terms of the complexity and accuracy corresponding to the case to be handled. The calculations of Küçükyılmaz [48] can provide a good pre-understanding about the compatibility of certain RANS based models with the flow physics of the present study. Simulation of the two-equation eddy viscosity model SST k- ω in [48], with curvature correction, was determined to be very successful to capture the vortex breakdown at the actual position. Besides, the one-equation model Spalart-Allmaras (S-A) was found to give promising results in terms of calculating the pressure coefficient close to the experiment. As a result of these motives, it was decided in this study to focus on the modeling the vortical flow field with SST k- ω and S-A.

The theory underlying these two RANS based turbulence models, along with the corresponding mathematical definitions, are explained and presented in the followings.

3.3.1 Reynolds Averaging and Boussinesq Approximation

Today, significant numbers of CFD simulations of turbulent flows are conducted with RANS models which are based on Reynolds averaging of the continuity and momentum equations. In this averaging, the solution variables in the instantaneous (exact) Navier-Stokes equations are decomposed into the mean (ensemble-averaged or time-averaged) and fluctuating components.

According to this, velocity components can be written as:

$$u_i = \bar{u}_i + u_i' \quad (3.1)$$

where \bar{u}_i and u_i' are the mean and the fluctuating components of velocity, respectively.

Scalar quantities like pressure, energy, or species concentration can be expressed similarly as follows:

$$\phi = \bar{\phi} + \phi' \quad (3.2)$$

In order to obtain Reynolds Averaged Navier-Stokes (RANS) equations, the expressions of the form above (3.1 and 3.2) for the flow variables are substituted into the instantaneous continuity and momentum equations first. Then, taking time average of these equations will yield the RANS equations which are presented in Cartesian tensor form as below:

$$\frac{\partial \rho}{\partial t} + \frac{\partial}{\partial x_i} (\rho \bar{u}_i) = 0 \quad (3.3)$$

$$\begin{aligned} \frac{\partial}{\partial t} (\rho \bar{u}_i) + \frac{\partial}{\partial x_j} (\rho \bar{u}_i \bar{u}_j) = & -\frac{\partial \bar{p}}{\partial x_i} + \frac{\partial}{\partial x_j} \left[\mu \left(\frac{\partial \bar{u}_i}{\partial x_j} + \frac{\partial \bar{u}_j}{\partial x_i} - \frac{2}{3} \delta_{ij} \frac{\partial \bar{u}_k}{\partial x_k} \right) \right] \\ & + \frac{\partial}{\partial x_j} (-\rho \overline{u'_i u'_j}) \end{aligned} \quad (3.4)$$

Here, ρ is the fluid density, t is time, \bar{p} is the time averaged pressure, μ is the dynamic viscosity and δ_{ij} is the Kronecker delta. There is one other term in the momentum equation that represents the effects of turbulence and needs to be modeled in order to close equation 3.4. It is $-\rho \overline{u'_i u'_j}$, called as Reynolds stress tensor.

A common method for modeling the Reynolds stresses uses the Boussinesq hypothesis to relate linearly these stresses to the rate of strain of the time averaged (mean) velocity and it is formulated as:

$$-\rho \overline{u'_i u'_j} = \mu_t \left(\frac{\partial \bar{u}_i}{\partial x_j} + \frac{\partial \bar{u}_j}{\partial x_i} \right) - \frac{2}{3} \left(\rho k + \mu_t \frac{\partial \bar{u}_k}{\partial x_k} \right) \delta_{ij} \quad (3.5)$$

Here, k represents the turbulence kinetic energy and μ_t the turbulent viscosity (or eddy viscosity). The advantageous side of this approach is the relatively low computational cost in terms of the computation of μ_t . The Boussinesq approximation is used in the S-A, $k-\omega$ and $k-\epsilon$ models. In S-A model, the turbulence kinetic energy is not calculated and only one additional transport equation (representing turbulent

viscosity) is solved. In the case of other two linear eddy viscosity models (k- ω and k- ϵ) on the other hand, two additional transport equations are solved. For both models one equation is solved for turbulence kinetic energy, k, and one for either the specific dissipation rate (ω) or the turbulence dissipation rate (ϵ). μ_t is then calculated as a function of k and ω or k and ϵ .

3.3.2 Spalart-Allmaras (S-A) Model

As mentioned above, the S-A model is a one-equation model and that solves a modeled transport equation for the kinematic eddy (turbulent) viscosity. It was proposed by P. R. Spalart and S. R. Allmaras in 1992 [49] being a compatible model with grids of any structure and Navier-Stokes solvers as well as powerful enough specifically for basic flows of aerospace applications. Moreover it has been shown to give good results for boundary layers subjected to adverse pressure gradients [50].

The variable that is transported in the S-A model is $\tilde{\nu}$ and its transport equation is:

$$\frac{\partial}{\partial t}(\rho\tilde{\nu}) + \frac{\partial}{\partial x_i}(\rho\tilde{\nu}u_i) = G_{\tilde{\nu}} + \frac{1}{\sigma_{\tilde{\nu}}}\left[\frac{\partial}{\partial x_j}\left\{(\mu + \rho\tilde{\nu})\frac{\partial\tilde{\nu}}{\partial x_j}\right\} + C_{b2}\rho\left(\frac{\partial\tilde{\nu}}{\partial x_j}\right)^2\right] - Y_{\tilde{\nu}} + S_{\tilde{\nu}} \quad (3.6)$$

Out of the near-wall (viscosity-affected) region, $\tilde{\nu}$ is identical to the turbulent kinematic viscosity and ν is the molecular kinematic viscosity again, $G_{\tilde{\nu}}$ is the production of turbulent viscosity and $Y_{\tilde{\nu}}$ is the destruction of turbulent viscosity that occurs in the near-wall region due to wall blocking and viscous damping. Besides, $S_{\tilde{\nu}}$ is the user defined source term and $\sigma_{\tilde{\nu}}$ and C_{b2} are model constants as being $2/3$ and 0.622 respectively.

Turbulent viscosity is then modeled as:

$$\mu_t = \rho\tilde{\nu}f_{v1} \quad (3.7)$$

The viscous damping function f_{v1} is:

$$f_{v1} = \frac{\chi^3}{\chi^3 + C_{v1}^3} \quad (3.8)$$

and

$$\chi \equiv \frac{\tilde{\nu}}{\nu} \quad (3.9)$$

with $C_{v1} = 7.1$

The mathematical definitions for the production and destruction of turbulent viscosity as well as the wall treatment of the model and other related details are presented in Appendix A.

3.3.3 Shear-Stress Transport (SST) k- ω Model

SST k- ω turbulence model was developed by Menter in 1994 [51] promoting a very effective manner to blend the above mentioned two-equation eddy viscosity models using the the Boussinesq approximation, k- ω and k- ϵ . It makes use of the strong sides of the k- ω model in the near wall region and the k- ϵ model in the further regions. In order to do so, the k- ϵ model is converted into a k- ω formulation [50].

Certain refinements separate this model from the standard k- ω . First of them is that the standard k- ω and the transformed k- ϵ models are both multiplied by a blending function and added together. In the near-wall region the blending function yields 1 activating the standard k- ω . However away from the surface, it takes the value 0 and this time the transformed k- ϵ model is activated. Another important difference is the modification of the turbulent viscosity in order to account for the transport of the turbulent shear stress. Besides to these, the SST k- ω incorporates a damped cross-diffusion derivative term in the ω equation and the modeling constants are different than those in the standard k- ω . The resulting of all these features makes the SST k- ω model more accurate and reliable than the standard k- ω for certain challenging cases like adverse pressure gradient flows, airfoils, transonic shock waves etc.

The transport equations for the SST k- ω model are given as:

$$\frac{\partial}{\partial t}(\rho k) + \frac{\partial}{\partial x_i}(\rho k u_i) = \frac{\partial}{\partial x_j} \left(\Gamma_k \frac{\partial k}{\partial x_j} \right) + \tilde{G}_k - Y_k + S_k \quad (3.10)$$

$$\frac{\partial}{\partial t}(\rho \omega) + \frac{\partial}{\partial x_j}(\rho \omega u_j) = \frac{\partial}{\partial x_j} \left(\Gamma_\omega \frac{\partial \omega}{\partial x_j} \right) + G_\omega - Y_\omega + D_\omega + S_\omega \quad (3.11)$$

Here, \tilde{G}_k represents the production of turbulence kinetic energy due to mean velocity gradients, G_ω indicates the production of ω , Y_k and Y_ω symbolizes the dissipation of k and ω due to turbulence, Γ_k and Γ_ω represent the effective diffusivity of k and ω , S_k and S_ω are user-defined source terms and D_ω indicates the cross-diffusion term.

The effective diffusivities for the SST k- ω model are given by:

$$\Gamma_k = \mu + \frac{\mu_t}{\sigma_k} \quad (3.12)$$

$$\Gamma_\omega = \mu + \frac{\mu_t}{\sigma_\omega} \quad (3.13)$$

σ_k and σ_ω are the turbulent Prandtl numbers for k and ω in these equations. The formulation for turbulent viscosity, μ_t , is given as:

$$\mu_t = \frac{\rho k}{\omega} \frac{1}{\max \left[\frac{1}{\alpha^*}, \frac{SF_2}{a_1 \omega} \right]} \quad (3.14)$$

$$\sigma_k = \frac{1}{F_1/\sigma_{k,1} + (1 - F_1)/\sigma_{k,2}} \quad (3.15)$$

$$\sigma_\omega = \frac{1}{F_1/\sigma_{\omega,1} + (1 - F_1)/\sigma_{\omega,2}} \quad (3.16)$$

In the above three equations S indicates the magnitude of the strain rate and a_1 , $\sigma_{k,1}$, $\sigma_{k,2}$, $\sigma_{\omega,1}$, $\sigma_{\omega,2}$ are model constants given as 0.31, 1.176, 1.0, 2.0 and 1.168 respectively. α^* , on the other hand, is a coefficient that damps the turbulent viscosity causing a low-Reynolds number correction and given as:

$$\alpha^* = \alpha_\infty^* \left(\frac{\alpha_0^* + \text{Re}_t/R_k}{1 + \text{Re}_t/R_k} \right) \quad (3.17)$$

$$\text{Re}_t = \frac{\rho k}{\mu \omega} \quad (3.18)$$

where, $R_k = 6$, $\beta_i = 0.072$, $\alpha_0^* = 0.024$ and $\alpha_\infty^* = 1$ having the same constant values as in the standard k - ω model. It must be noted that in the high-Reynolds number form of the k - ω model even $\alpha^* = \alpha_\infty^* = 1$.

The blending functions, F_1 and F_2 , are formulated as:

$$F_1 = \tanh(\phi_1^4) \quad (3.19)$$

$$\phi_1 = \min \left[\max \left(\frac{\sqrt{k}}{0.09\omega y}, \frac{500\mu}{\rho y^2 \omega} \right), \frac{4\rho k}{\sigma_{\omega,2} D_\omega^+ y^2} \right] \quad (3.20)$$

$$D_\omega^+ = \max \left[2\rho \frac{1}{\sigma_{\omega,2}} \frac{1}{\omega} \frac{\partial k}{\partial x_j} \frac{\partial \omega}{\partial x_j}, 10^{-10} \right] \quad (3.21)$$

$$F_2 = \tanh(\phi_2^2) \quad (3.22)$$

$$\phi_2 = \max \left[2 \frac{\sqrt{k}}{0.09\omega y}, \frac{500\mu}{\rho y^2 \omega} \right] \quad (3.23)$$

Here, D_ω^+ represents the positive part of the cross-diffusion term and y symbolizes the distance to the next surface.

Further detailed information about the modeling of SST k - ω , including the generations of k and ω (\tilde{G}_k and G_ω terms), their dissipations (Y_k and Y_ω terms) and the cross-diffusion modification of the model (D_ω term) as well as related model constants, are provided in Appendix A.

In addition to all the definitions of the linear eddy-viscosity models above, one should be aware of the deficiency of them that they are insensitive to the effects of streamline curvature and system rotation, which play a significant role in many

turbulent flows of practical interest. In order to overcome this problem and to take into account these effects, a modification of the production term has been derived firstly by Spalart and Shur [52] for one equation S-A model, and based on this work Smirnov and Menter [53] derived another modification for the standard two-equation turbulence models. Applying these corrections make significant effect on the solution performances of the models to the vortical flow systems occurring on delta wings.

3.4 Grid Independence Study

The incompressible turbulent flow physics over the wing, including boundary layer separations, instabilities, vortical structure and its breakdown, was solved using steady RANS based models in ANSYS Fluent.

In order to achieve a converged and grid independent solution, SST $k-\omega$ turbulence model was utilized in conjunction with the curvature correction extension. This viscous, two-equation eddy viscosity model was chosen since its popular superior performance in terms of behaving the adverse pressure gradients and separating flows successfully. The achievement attained in the study of Küçükylmaz [48] was also another major factor leading to use of this model. The correction extension was also necessary to sensitize the model to the effects of streamline curvature as it was suggested by the literature [52, 53] and mentioned above.

The simulated air flow has the conditions of $M= 0.07$ and $Re_{mac}= 1 \times 10^6$. This brings out the free stream velocity being set to 24 m/s and its turbulent intensity was assigned as 0.1 %, being a quite low rate as it is also desired in experimental investigations. All of the boundary conditions corresponding to the solution set up for this study can be found in Table 3.5.

SIMPLE scheme was used for pressure-velocity coupling. In order to interpolate the field variables, which are momentum, turbulence kinetic energy (k), and specific dissipation rate (ω), to the faces of the control volume (convective term), a second order upwind scheme was employed. Green-Gauss Node Based spatial discretization scheme was chosen for determining the gradients of the solution variables and Standard interpolation scheme was used for calculating the cell face pressures.

Table 3.5 Boundary conditions

Zone	Boundary Type	Related Parameter	Value
Inlet	Velocity Inlet	Velocity Magnitude (m/s)	24
		Turbulent Intensity (%)	0.1
		Turbulent Viscosity Ratio	10
Outlet	Pressure Outlet	Gauge Pressure (Pascal)	0
Symmetry Plane	Symmetry	Symmetry	-
Top, Side and Bottom Walls	Wall	Free Slip	-
All Wing Surface	Wall	No Slip Wall	-

A large number of calculations were run with different settings for the relaxation factors and initialization parameters in the solver to achieve converged solutions. The convergence of the solutions was assured by checking mainly two parameters. First of them was to observe the scaled residual histories of continuity, three velocity components, k and ω . In Figure 3.12 the residuals of Mesh 3 calculation are presented. The second one was to monitor the history of the average velocity magnitude values at eight points randomly distributed over the wing. Figure 3.13 reveals the distribution of the points on the layers which are located above the suction side with distances of 4, 20, 55 and 110 mm, respectively. In Figure 3.14 the velocity magnitude histories of three points are provided. As can be seen here, the iteration numbers waited in calculations are not the same for the four grids under run. At some monitor points especially, even the residuals begin to show a steady trend for that mesh, the velocity magnitudes could still be observed altering.

Besides these, the y^+ contours of the wing surfaces after each calculation were plotted and it was seen that their maximum was kept around 1, which is an indication of a successful wall treatment for SST $k-\omega$ model in Fluent. The y^+ contour plot for Mesh 2 is given in Figure 3.15.

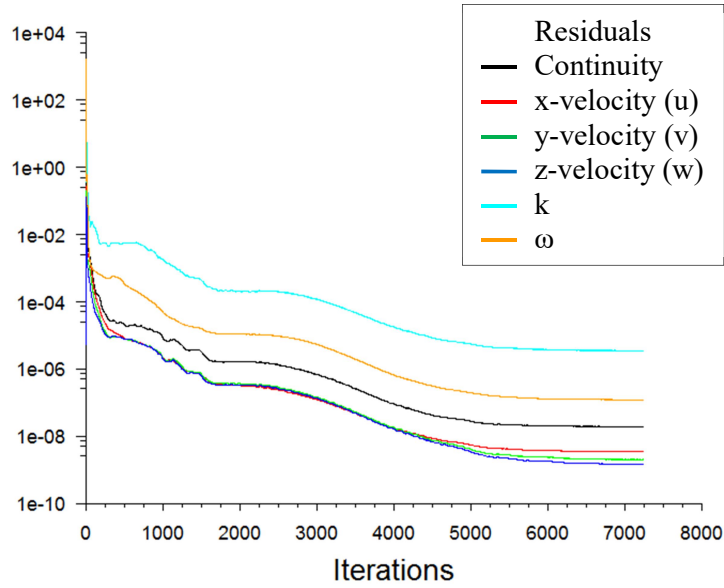


Figure 3.12 Scaled residual history of Mesh 3 calculation

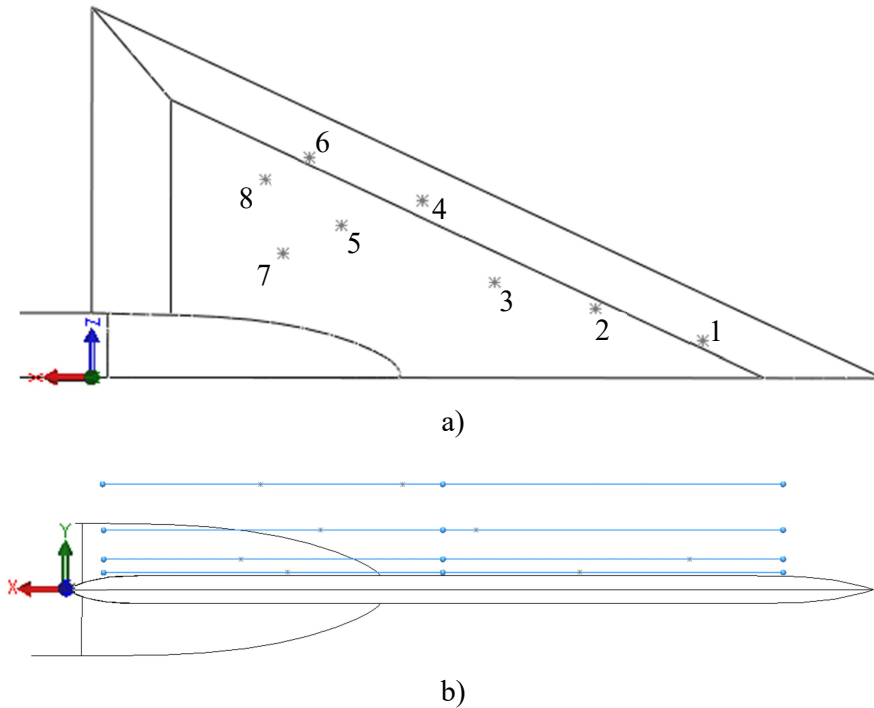
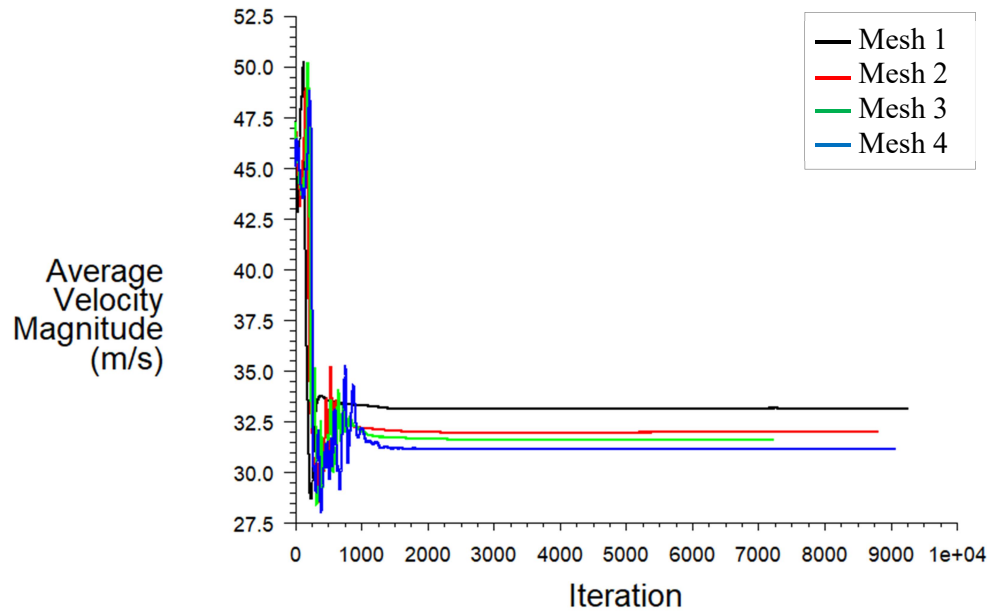
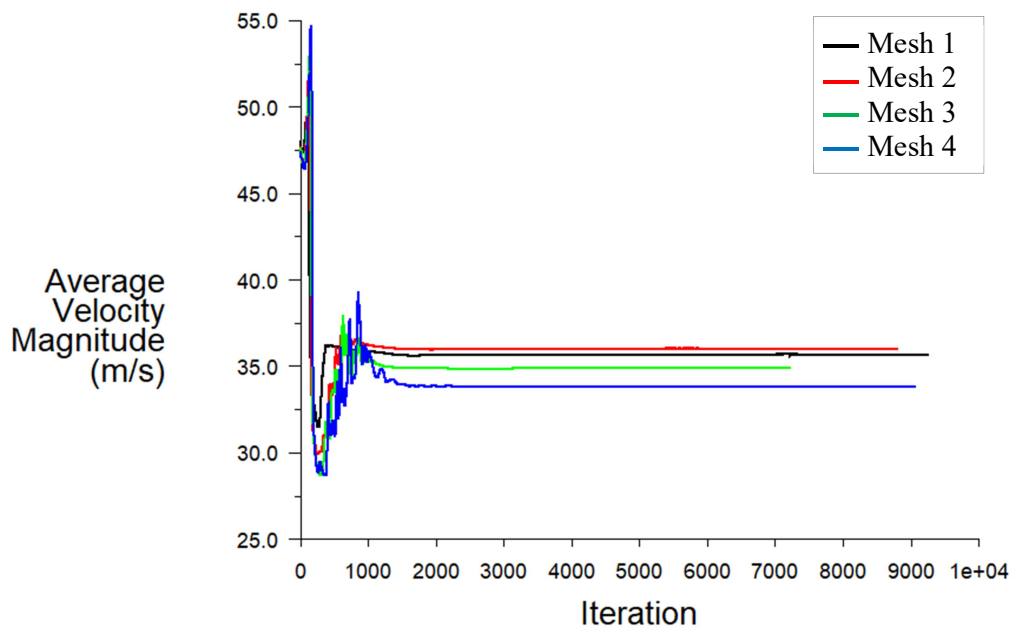


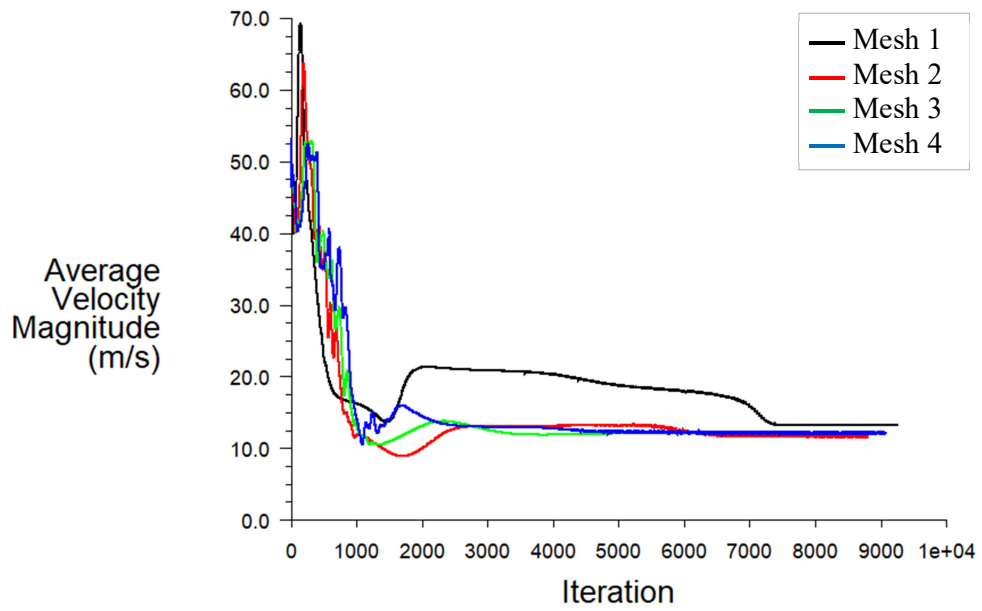
Figure 3.13 Monitor points distribution: a) top (numbers were given in line with the x-coordinate from the apex) and b) side view (small grey points distributed on layers which are located with distances of 4, 20, 55 and 110 mm, respectively)



a)



b)



c)

Figure 3.14 Velocity magnitude histories at a) Point 2, b) Point 3 and c) Point 6

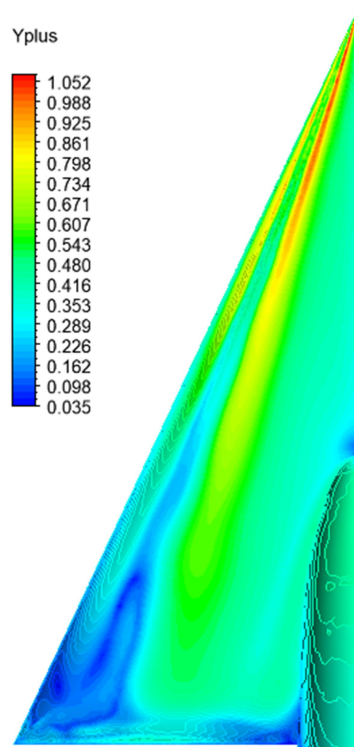


Figure 3.15 y^+ contour of Mesh 2

The meshes having the escalating number of elements were solved to understand the optimum sizing setting for the numerical analysis. One of the main variables used to assess the mesh independence is the pressure coefficient calculated on chord wise stations on the wing upper surface. Figure 3.16 shows that stations located at $x/C= 0.4$ and 0.6 . The C_p charts of the four meshes drawn on these two lines are provided in Figure 3.17. It is clear from this figure that, Mesh 3 and Mesh 4 present similar profiles in each station. Especially in $x/C= 0.4$ they are distinctly closer to each other and comparing to other meshes more successful to reproduce the secondary vortex which is evident as a second low-pressure peak outboard of the primary peak.

When looking into the scaled C_p contour plots given in Figure 3.18, the primary vortex core and, at its outboard, the footprints of the secondary vortex core are visible as blue lower pressure areas. The vortex breakdown, a consequence of increasing adverse pressure gradient, can also be recognized by higher pressure fields downstream. Similar to the span wise C_p charts in Figure 3.17, Mesh 3 and Mesh 4 are demonstrating much closer contour structures. They clearly have more mature and finely resolved areas, especially in the primary and secondary vortex regions.

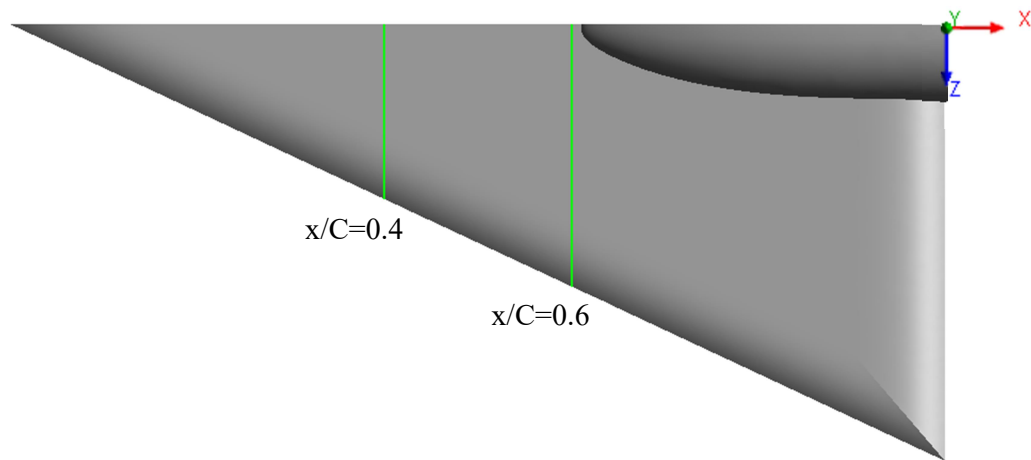
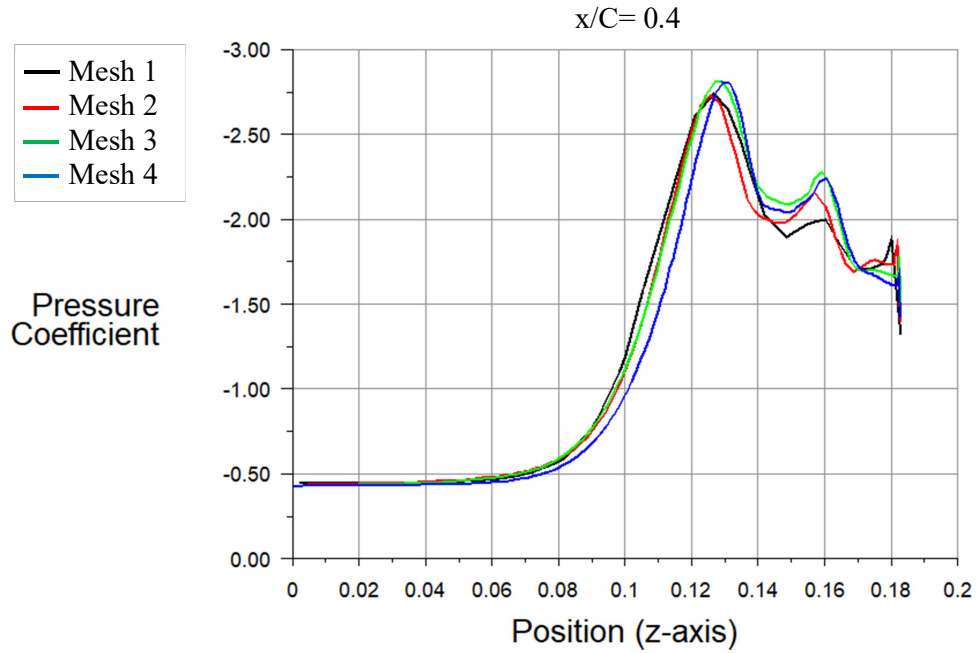
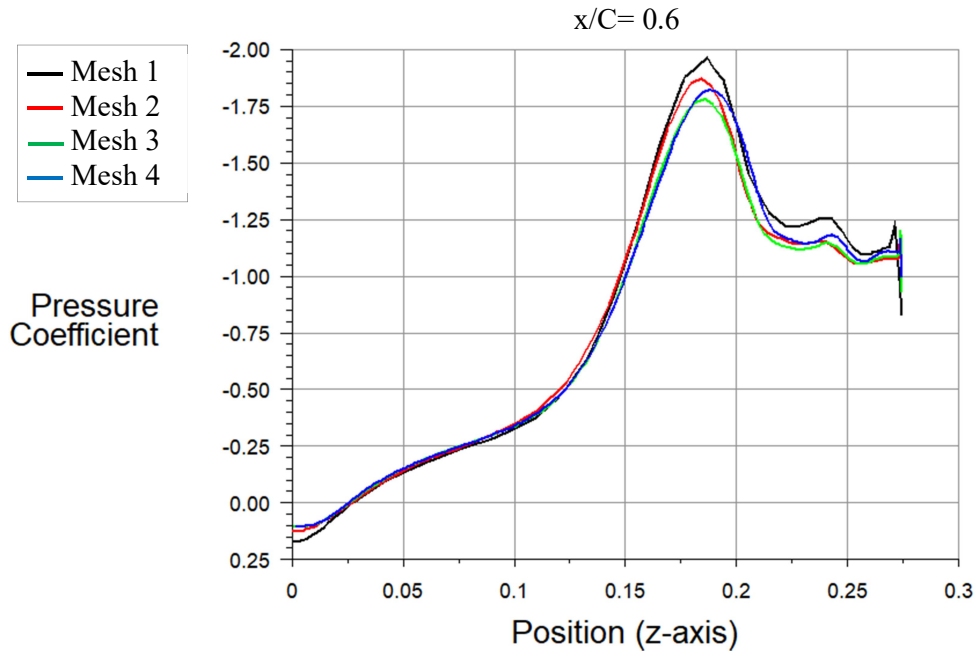


Figure 3.16 Stations where pressure coefficient is calculated



a)



b)

Figure 3.17 Cp profiles of the four meshes at chord wise stations on the suction side
 a) $x/C=0.4$, b) $x/C=0.6$

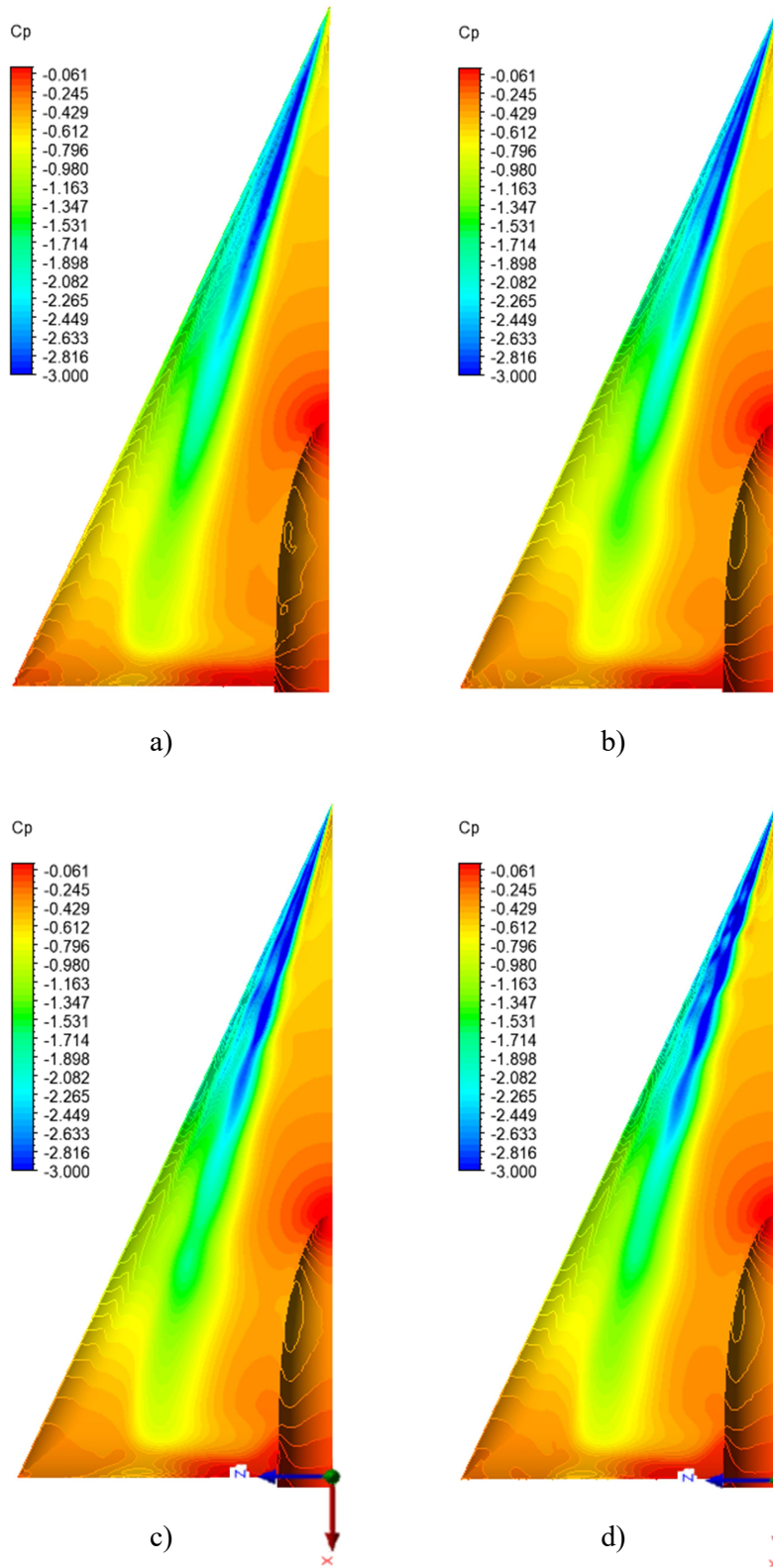
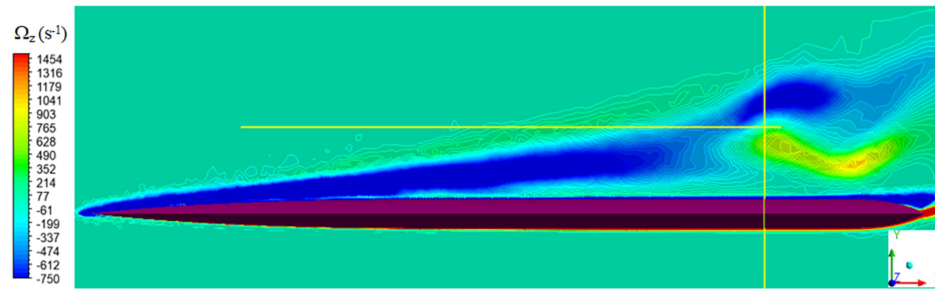


Figure 3.18 C_p contours: a) Mesh 1, b) Mesh 2, c) Mesh 3, and d) Mesh 4

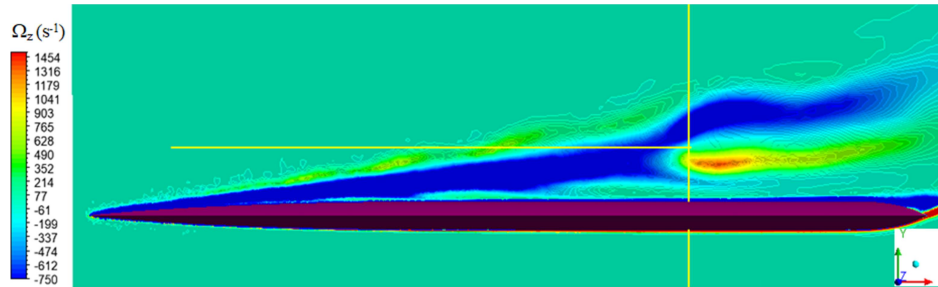
Another prominent parameter investigated for grid independence is the azimuthal vorticity contours, plotted on planes cutting the wing perpendicular and along the primary vortex core. Figure 3.19 presents these contours with two yellow lines on it. The vertical yellow line shows the section where the axial velocity inside the vortex core stagnates and first switches sign from positive to negative, causing a backflow, which is accepted as an indication of breakdown initiation. This phenomenon is also seen clearly in a good agreement with the azimuthal vorticity sign switching process, as expected. The horizontal line, on the other hand, represents the vertical position of the vortex core which is determined by finding the minimum velocity element inside the region.

The azimuthal vorticity contours reveal the much finer resolution of Mesh 3 and Mesh 4, resembling to each other and having certain differences from other two coarser meshes. Besides, here we have the chance to see the breakdown positions of the vortices and their movement to the apex by refining the grid. By looking at the plots, one simply can say that the breakdown locations of Mesh 3 and Mesh 4, which is the third and the most important parameter checked in the mesh independence, are fairly close to each other, again being different from other two grids. The tabulated coordinates of the breakdown locations of the four grids are given in Table 3.6 and the normalized axial velocity contours for each grid, plotted on the cross planes at their breakdown locations, are provided in Figure 3.20. The vortex breakdown initiation was determined using these contours by checking the axial position where the sign of the normalized stream wise velocity (u/U_0) inside the vortex core first turned into negative.

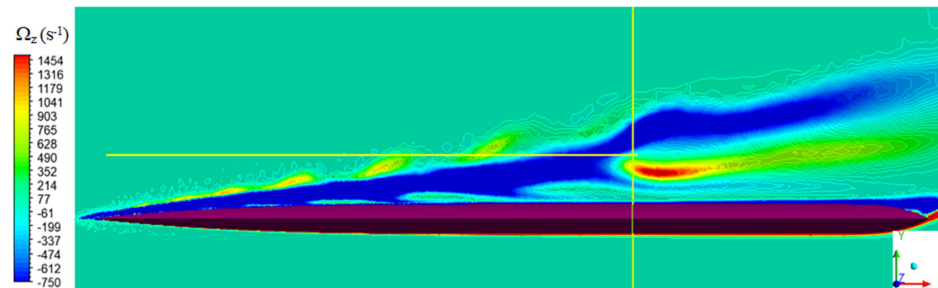
Mesh 3 was chosen as the grid to be used for proceeded investigations in this study since giving finer, more mature and distinguished results when compared with Mesh 1 and Mesh 2, besides showing significantly close performance to Mesh 4 considering the assessment parameters above, most importantly the breakdown location. It has also the advantage of employing less number of elements than Mesh 4, so requiring less computational power and time.



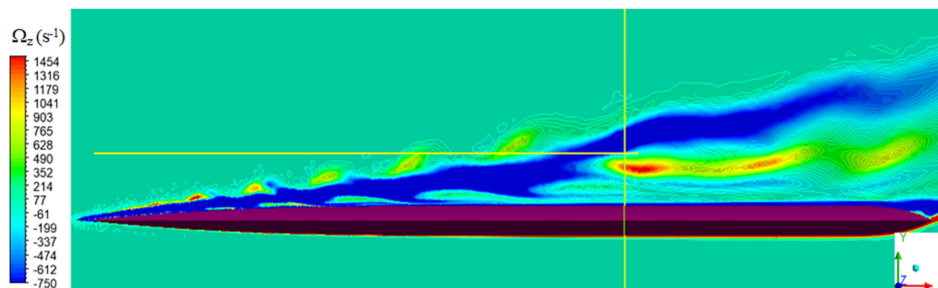
a)



b)



c)



d)

Figure 3.19 Azimuthal vorticity contours: a) Mesh 1, b) Mesh 2, c) Mesh 3 and d) Mesh 4. Vertical line indicates where the axial velocity at the vortex core first switches signs, and horizontal one shows the position of the vortex core

Table 3.6 Vortex breakdown locations of four meshes

	Mesh 1	Mesh 2	Mesh 3	Mesh 4
x-coord. (m)	-0.186	-0.279	-0.342	-0.352
x/C	0.81	0.72	0.65	0.64

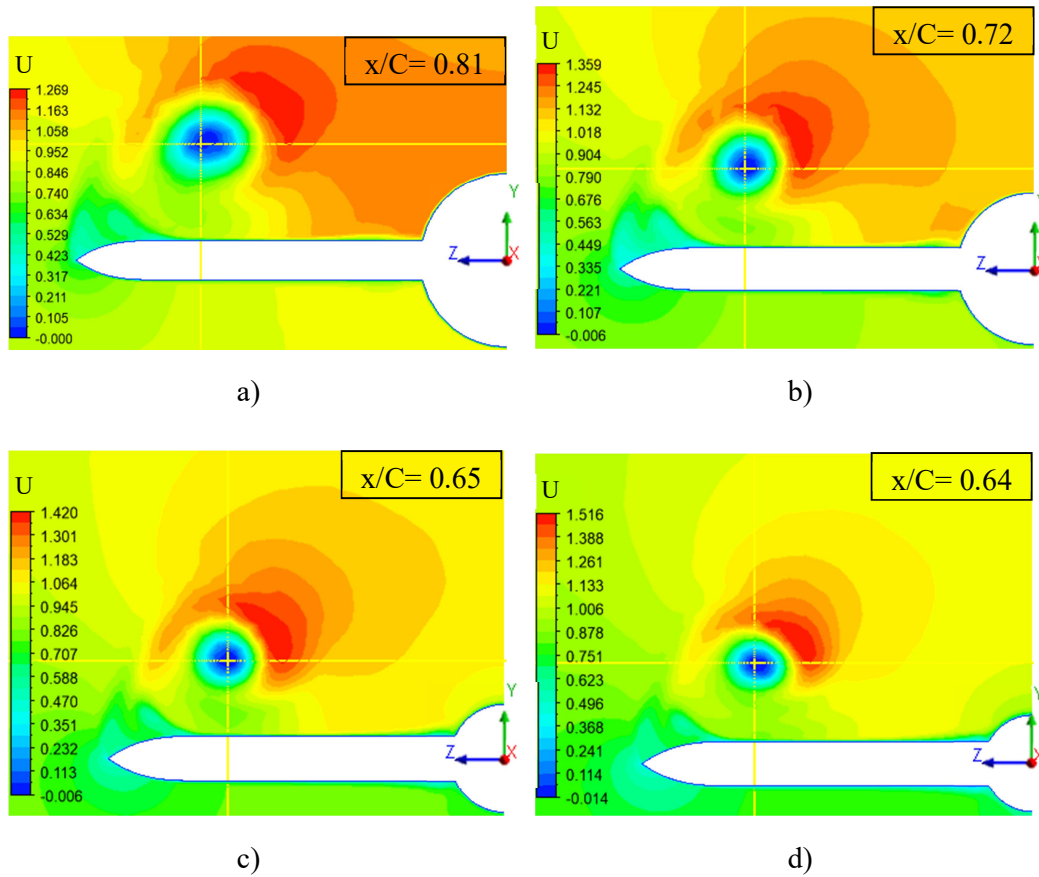


Figure 3.20 Contours of axial velocity normalized free stream velocity ($U= u/U_0$) of a) Mesh 1, b) Mesh 2, c) Mesh 3 and d) Mesh 4 at where axial velocity first switches sign (breakdown initiation). Cross-hair shows the point of the minimum velocity element which can be considered the core center.

CHAPTER 4

VALIDATION STUDY

After obtaining the mesh independent solution of SST $k-\omega$ model, some of its results were first compared with the findings of a second simulation that was done using Spalart-Allmaras (S-A) with curvature correction (cc) which was, to a certain extent, another distinguished turbulence model in [48] for the correct representation of the vortical flow over the wing. The S-A calculation was also performed using Mesh 3 in Fluent under the same Re , M and angle of attack values of the grid independence study and with all the same solution parameters previously set for the SST $k-\omega$ run. This comparison enabled a quick insight into some important differences between the two models.

The outcomes of these two RANS models were then comprehensively evaluated by comparing them with the experimental as well as the numerical solution data available in the literature in order to verify and validate their accuracies.

Figure 4.1 and 4.2 present some important aspects of the results coming out of S-A and SST $k-\omega$ calculations to have an idea about how different the performances of the two models, as a first glance. Figure 4.1 depicts the C_p contours. As can be seen clearly that the secondary separation and correspondingly the secondary vortex could not be captured by S-A, as successfully as done by SST $k-\omega$. Besides, the iso-surface lines for the S-A plot noticeably show much straighter structure at the primary suction region and around it, indicating a lower performance of resolving the shear layer. On the other hand, the low pressure profile occurring at the primary vortex region looks stronger and continues more downstream in S-A solution when compared with SST $k-\omega$. Looking at the azimuthal vorticity contours given in Figure 4.2, similar lower resolution of S-A calculation in terms of reproducing the shear layer and vortical structure is visible. Additionally, as observed on the C_p contours in

Figure 4.1, vortex breakdown took place at a more downstream location in S-A solution when compared with SST k- ω .

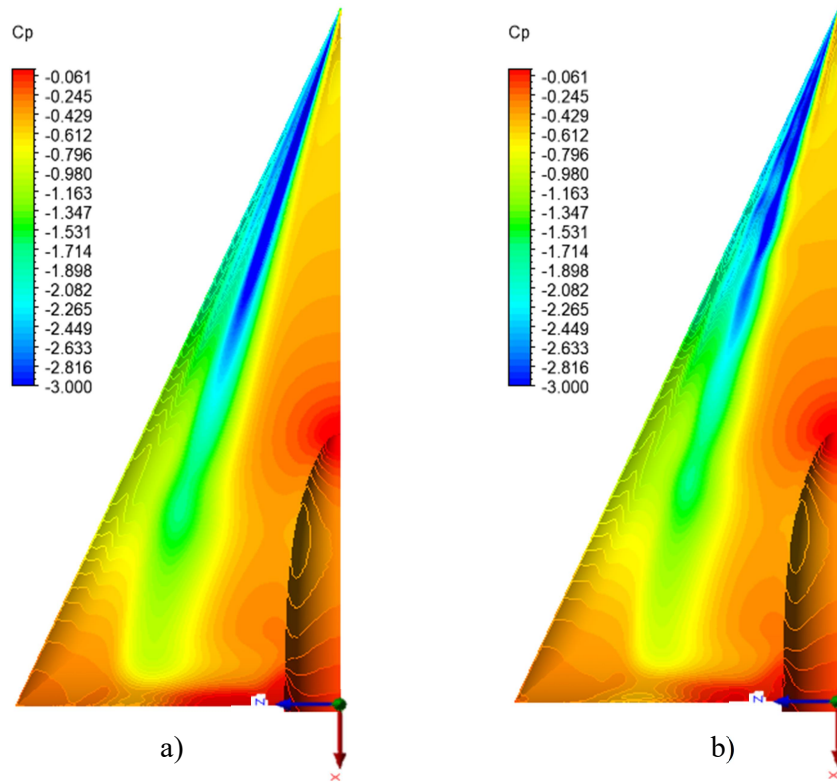


Figure 4.1 Cp contours of a) S-A-cc and b) SST k- ω -cc

Besides this alternative analysis, experimental and numerical data provided by Tangermann et al. [7] was used to assess the quality of SST k- ω calculations.

In [7], authors performed unsteady SST-Detached Eddy Simulation (DES), a combination of Large Eddy Simulation and RANS approach, of the air flow passing by the same VFE-2 wing configuration with again 23° angle of attack and under exactly the same Re and M of the present study. They then compared and validated the DES results with experimental ones, which were obtained by Furman and Breitsamter [8] in the low speed wind tunnel test as a part of VFE-2. In [8], though, the quality of the experimental results were judged and assured by comparing with the pressure measurements implemented by NASA on the same delta wing [4, 28].

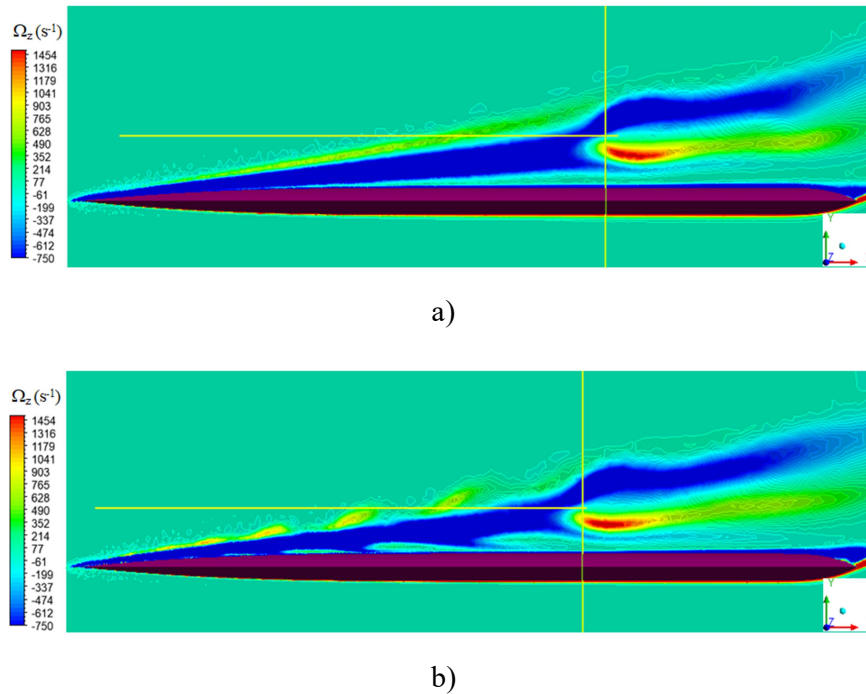


Figure 4.2 Azimuthal vorticity contours of a) S-A-cc and b) SST k- ω -cc

Figure 4.3 shows the C_p profiles of experimental data, SST-DES, S-A-cc and k- ω -SST-cc at the five chord wise stations.

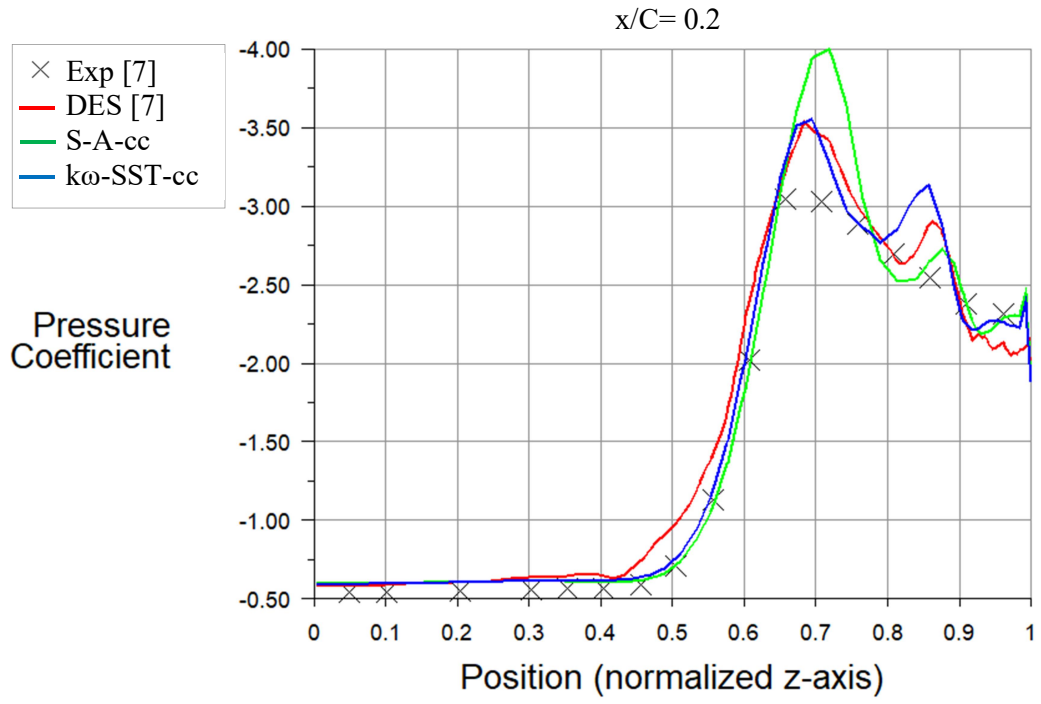
At the first cross section ($x/C=0.2$), the primary suction peak was over predicted by all numerical models when compared with the experiment. However it is evident that the experimental measurement failed to sense the secondary peak sourcing from the secondary vortex. k- ω and DES looks giving similar value for the primary vortex, while secondary peak of k- ω is slightly higher and inboard than DES. S-A, though, gives the highest peak of the primary vortex, putting out on the other hand the lowest and most outboard one for the secondary vortex.

In the next station ($x/C=0.4$), a two-vortex structure is clearly demonstrated by both experimental and numerical results. For the primary suction, DES and S-A show closer profiles to experiment than k- ω does. However, in capturing the secondary vortex, k- ω apparently does a better job than its alternatives. Besides, all three turbulence models seem adequately right in terms of determining the position of the both vortices.

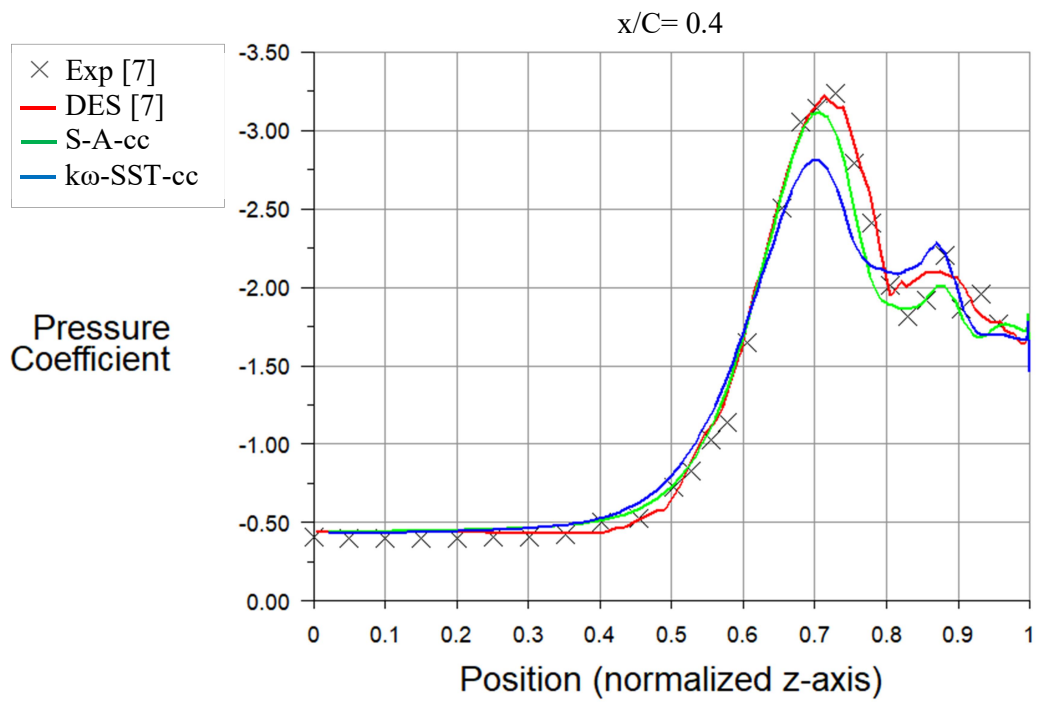
These two C_p charts ($x/C= 0.2, 0.4$) reveals also an important characteristic of SST $k-\omega$ model. The better performance of this model in capturing the secondary flow separation and correspondingly the secondary vortex causes a drop in its primary suction peak evaluation. One equation S-A model, though, behaves in opposite way as can be seen clearly from the charts.

The footprint of the secondary vortex is hardly visible in experimental data at the third ($x/C= 0.6$) station. This might be caused by the onset of the primary vortex breakdown. As it was stated in [7], the secondary vortex cannot get fed enough energy by the primary vortex any more after it has started to break down and thus its axis has separated further from the wing surface. Same weak presentation of the secondary vortex is also evident for $k-\omega$ and S-A profiles with a slightly inboard peak. However, the primary peak in S-A solution is still significantly higher than it is in $k-\omega$ solution. This is consistent with the characteristic definition mentioned above. DES is still giving strong primary and secondary suction peaks, meaning a later breakdown compared with the experiment, as again expressed in [7]. All three numerical models, on the other hand, under predicted the primary peak and they are located slightly inboard of the experimental one at this cross section.

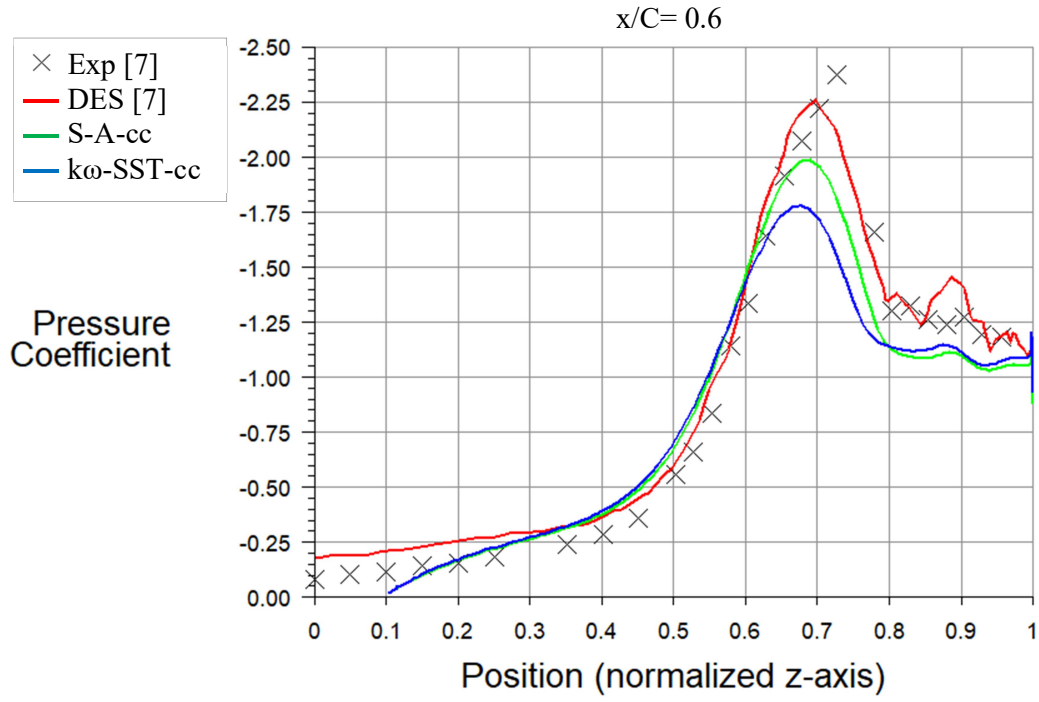
Last two charts (d and e) are clearly behind the breakdown of the primary vortex, yielding the primary suction to drop significantly and the secondary peak to almost vanish. Only DES shows a slightly stronger peak for the secondary vortex at $x/C= 0.8$. Concerning the primary suction peaks at the last two cross sections, DES and S-A look catching it successfully in the fourth station, however under predicting it at the last. $k-\omega$, on the other hand, gives weaker peaks for the primary vortex at both stations, which again can be read as a consequence of its previously explained behavior. Besides to these, all three simulations can be said to be in good agreement with the experiment in terms of the span wise location of the primary peak for the station $x/C= 0.8$. At the last cross section, though, only $k-\omega$ produces a slightly inboard primary peak.



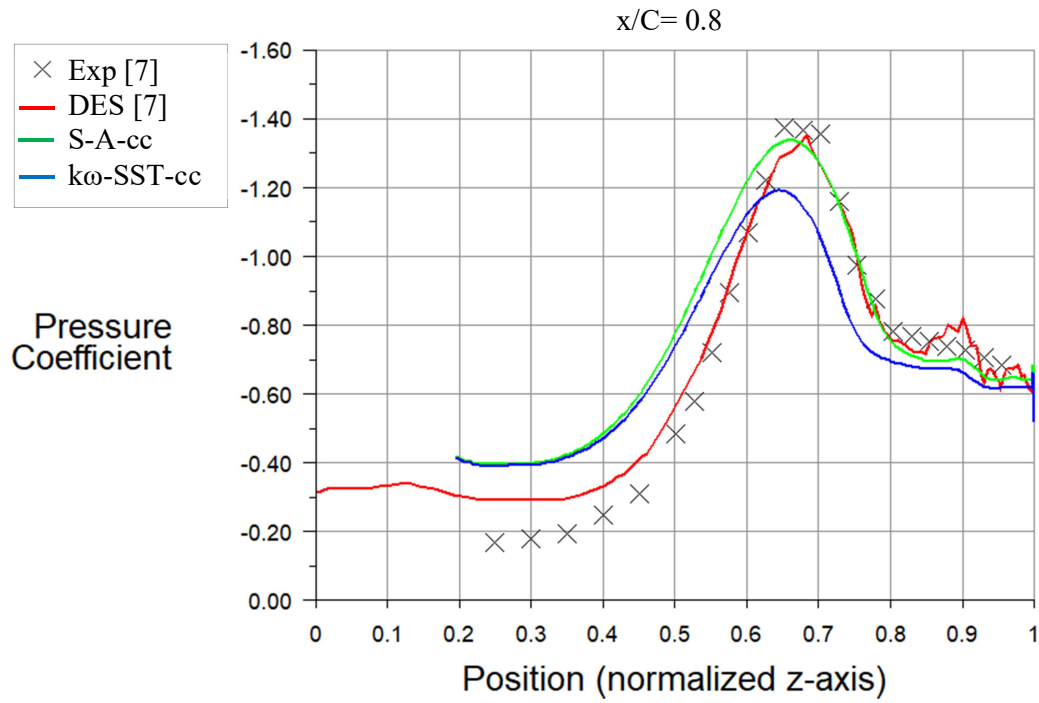
a)



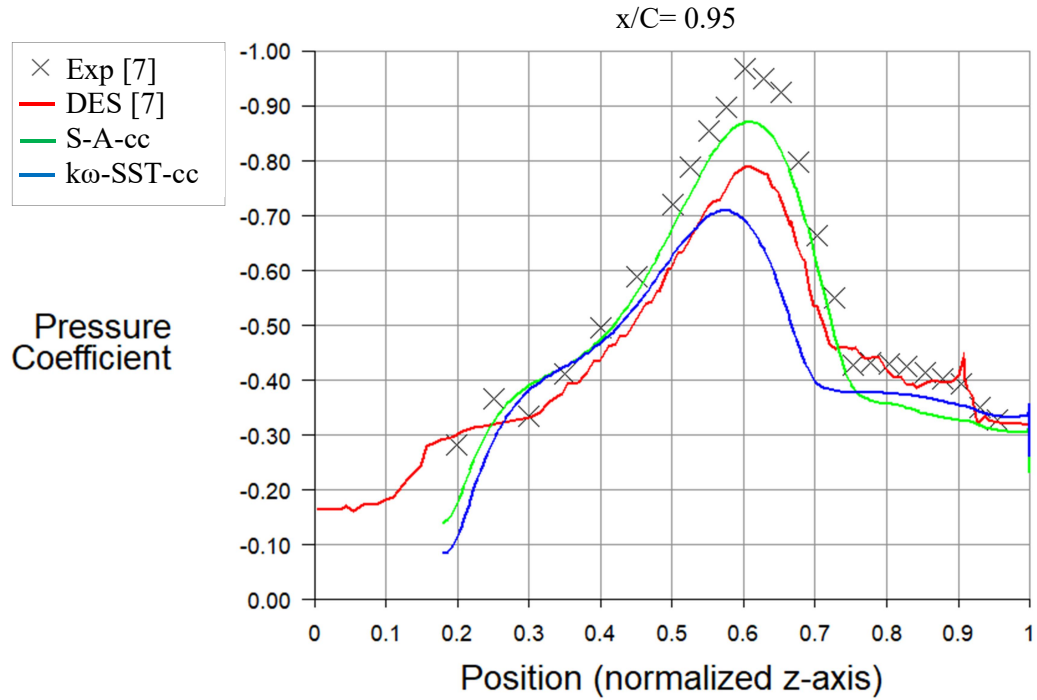
b)



c)



d)



e)

Figure 4.3 Span wise C_p profiles of the experiment [7] and three numerical simulations at chord wise stations on suction side a) $x/C=0.2$, b) $x/C=0.4$, c) $x/C=0.6$, d) $x/C=0.8$, and e) $x/C=0.95$

In [7], Tangermann et al. also compared their numerically generated streamlines of surface friction with the oil flow visualization on the wing upper surface conducted by Furman and Breitsamter. In Figure 4.4, these two data were presented together with wall shear streamlines calculated by S-A and SST $k-\omega$ models.

The streamlines of numerical calculations were drawn on their surface C_p contours. This gives the opportunity to see how compatibly the separations and vortices are presented by them. It is obvious from this figure that the C_p contours of DES and SST $k-\omega$ is much closer to each other at the primary and secondary vortex regions when compared with the S-A.

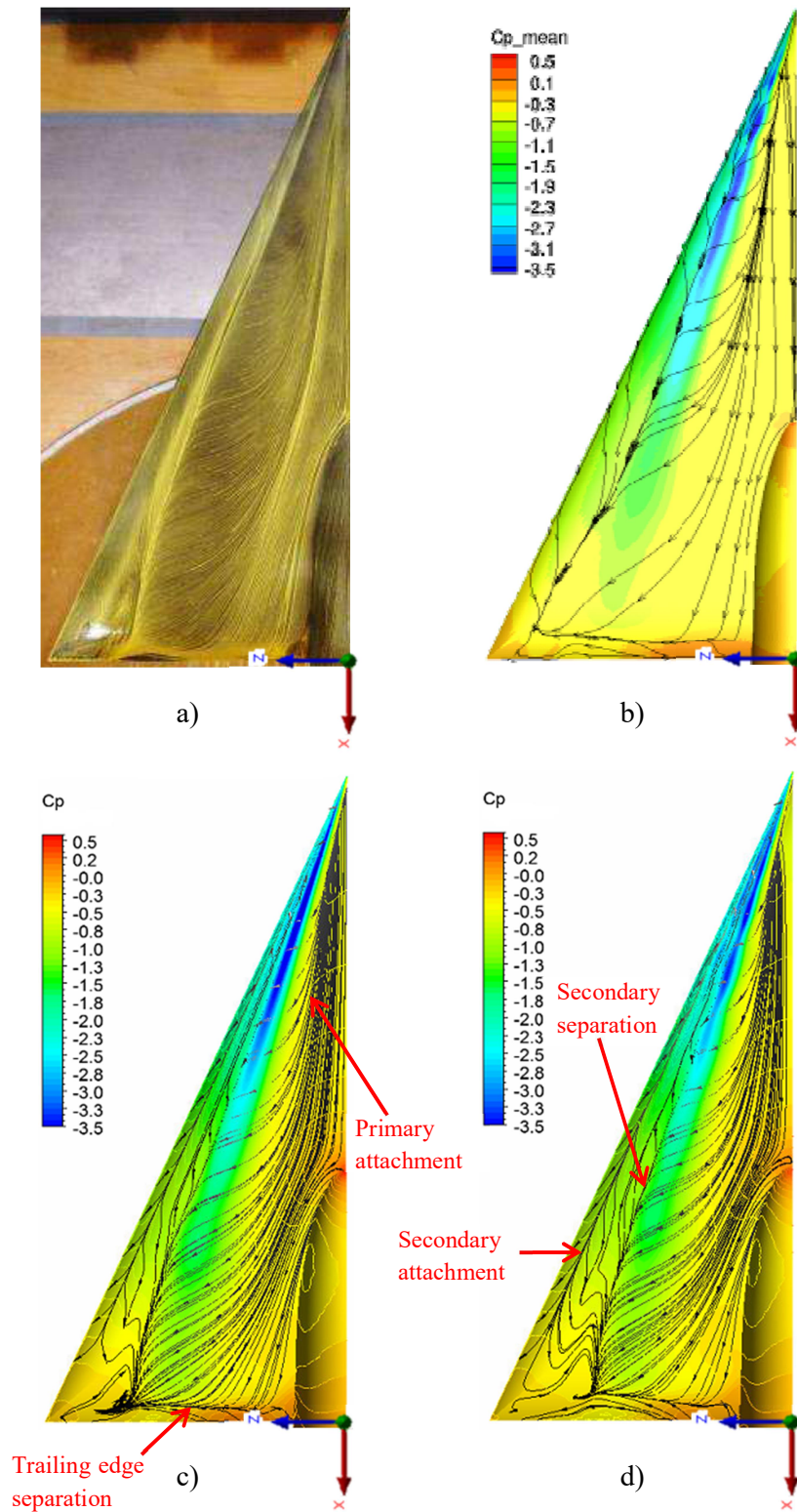


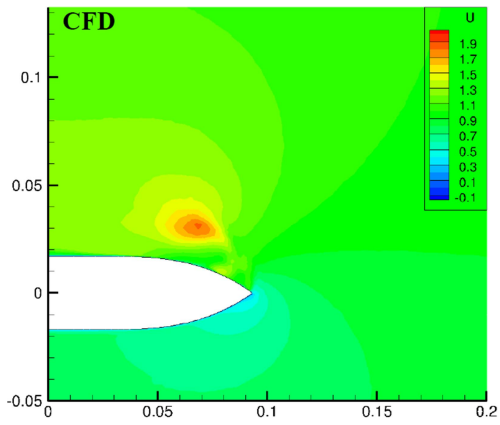
Figure 4.4 Experimental and numerical streamlines with Cp contours a) experiment [7], b) DES [7], c) S-A-cc and d) SST $k-\omega$ -cc

Concerning the streamlines, both S-A and SST $k-\omega$ looks in a better agreement with the experimental image, when compared with DES representation. The primary separation line is the leading edge itself. Besides, the primary attachment, secondary separation, secondary attachment and trailing edge separation lines can clearly be seen in S-A and SST $k-\omega$ streamlining. Although DES streamlines look similar in general sense to experiment and other two numerical representations, it reveals certain differences for the primary attachment line closure at the trailing edge and also for the secondary separation and attachment zones.

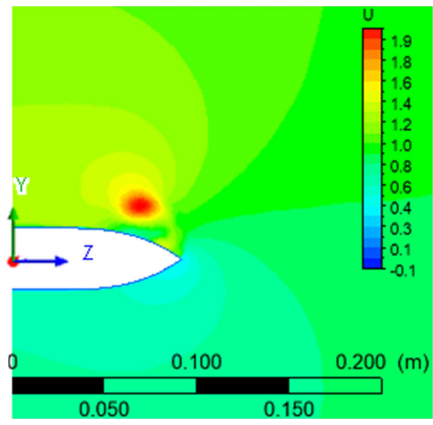
Contours for axial velocity normalized by the free stream velocity ($U = u/U_0$) were used as another means for comparing the numerical calculations only. Figure 4.5 presents these contours plotted on vertical planes at cross sections $x/C = 0.2, 0.4, 0.65$ and 0.95 taking DES contours again from [7]. In all cross sections, all three simulations can be said to give very similar results in terms of locations of the primary vortex cores, the recirculation zones at their centers and the overall contour profiles. However, there are certain differences between them sourcing mainly from having different vortex intensities and breakdowns at different locations along the wing.

In the first cross section ($x/C=0.2$) S-A and SST $k-\omega$ are clearly producing stronger peak of axial velocity than DES simulation. In the second ($x/C= 0.4$), though, $k-\omega$ have slightly weaker vortical core than the other two. The view at the next cross section ($x/C= 0.65$) clarifies this circumstance. Contour of $k-\omega$ simulation apparently shows the vortex breaking down giving negative axial velocity at this section. DES and S-A contours, on the other hand, are looking as they have not reach the breakdown point yet. The last plots ($x/C= 0.95$), though, reveals how closely the three simulations computed the velocity field and the flow separation on the trailing edge, indicated by the negative stream wise velocity appearing on the wing surface.

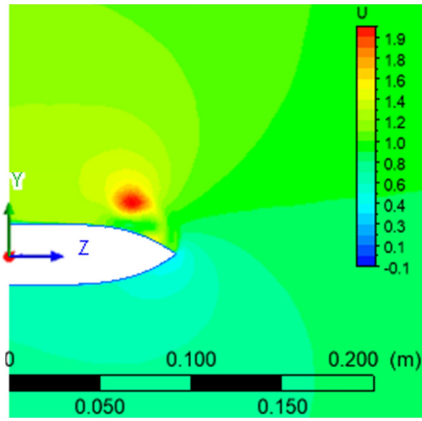
$x/C = 0.2$



a)

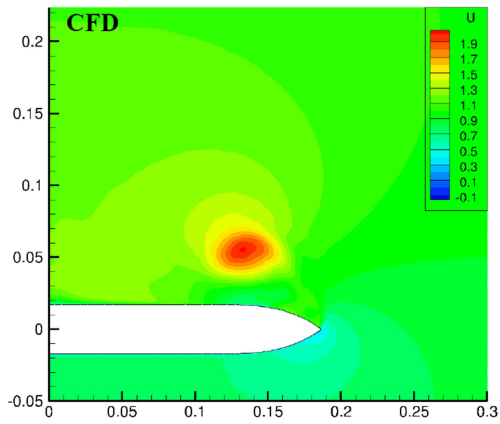


b)

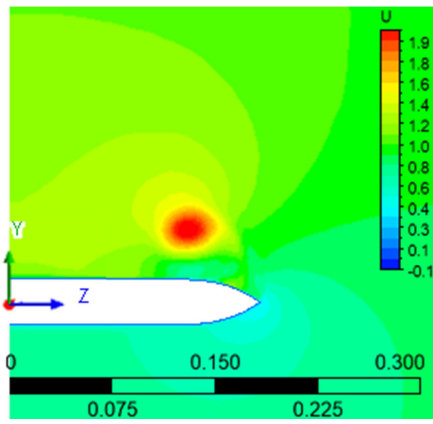


c)

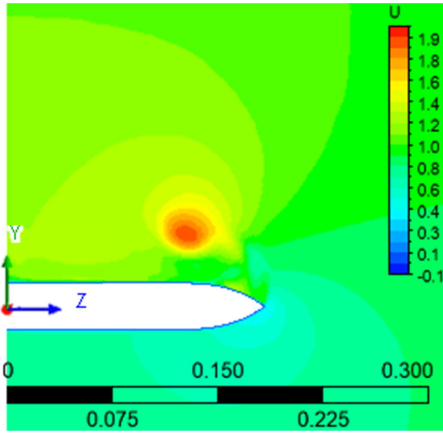
$x/C = 0.4$



a)

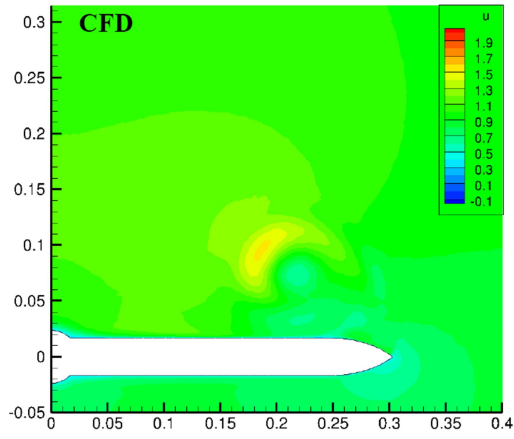


b)

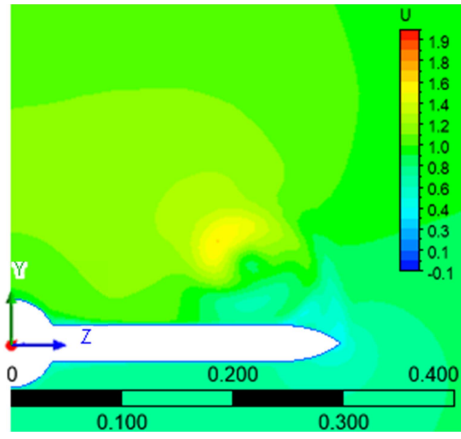


c)

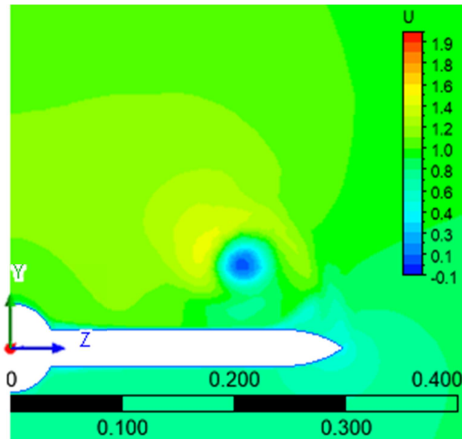
$x/C = 0.65$



a)



b)



c)

$x/C = 0.95$

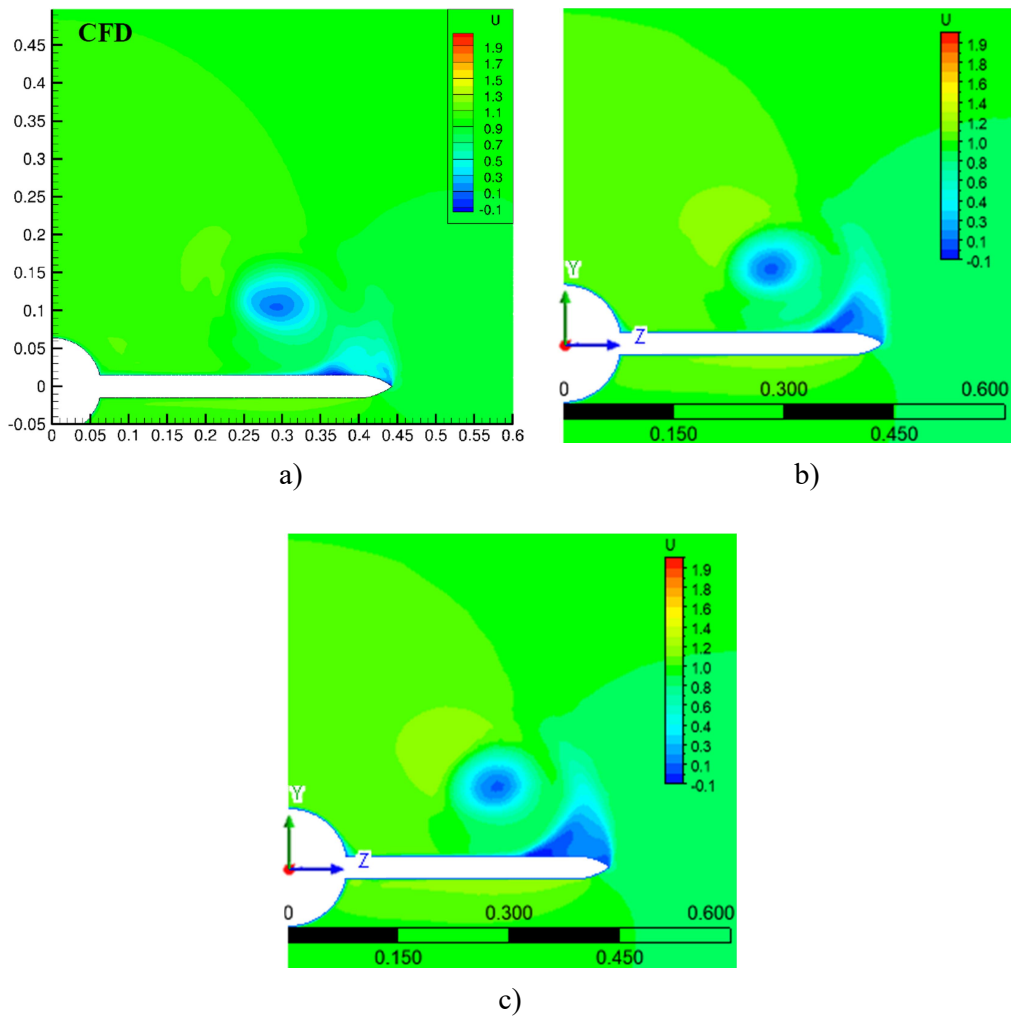


Figure 4.5 Normalized axial velocity ($U=u/U_0$) contours at $x/C=0.2$,
0.4, 0.65, and 0.95: a) DES [7], b) S-A-cc and c) SST $k-\omega$ -cc

The positions of the primary vortices at cross sections $x/C= 0.4, 0.6$ and 0.8 in the numerical calculations were determined by digitizing precisely the maximum or minimum velocity points found on the normalized axial velocity contours given in Figure 4.5. Besides, using the vectorial velocity field representations provided in [7], primary vortex core of the experimental observation for the same cross sections were localized with an error extent only in mm. All corresponding coordinate data was presented in Table 4.1. Looking this table, both SST $k-\omega$ and S-A solutions can be said to have predicted the primary vortex at very similar positions with DES and experiment, along with having some small deviations.

The locations of the vortex breakdown for the numerical calculations and experiment are provided in Table 4.2. The breakdown location data for DES and experiment was again provided by [7], while for the $k-\omega$ and S-A solutions they were obtained again using the normalized axial velocity contours plotted on cross planes over the wing. It is clearly seen here that SST $k-\omega$ showed better performance in capturing the breakdown location when compared with S-A.

Table 4.1 Vortex core location coordinates

Units are in meters (m)	$x/C= 0.4$		$x/C= 0.6$		$x/C= 0.8$	
	z	y	z	y	z	y
Exp [7]	0.135	0.060	0.192	0.088	0.256	0.100
DES [7]	0.132	0.055	0.191	0.081	0.255	0.090
S-A-cc	0.129	0.055	0.189	0.083	0.248	0.090
SST $k-\omega$ -cc	0.129	0.051	0.184	0.089	0.248	0.090

Table 4.2 Vortex breakdown locations of the turbulence models and experiment

	Experiment [7]	SST DES [7]	SST $k-\omega$ -cc	S-A-cc
x-coord. (m)	-	-	-0.342	-0.314
x/C	0.60	0.65	0.65	0.68

Both S-A and $k-\omega$ can be found sufficiently good at calculating the pressure and velocity fields. However, regarding the comparisons above on capturing the secondary separation and vortex, resolving the shear layer, surface streamlines and most importantly simulating the primary vortex breakdown, SST $k-\omega$ -cc can be said to have reproduced the flow field more successfully. Besides, in determining the breakdown location as well as evaluating the secondary and trailing edge separations and their corresponding influences, steady SST $k-\omega$ seems produced very close to, sometimes even finer outcomes than unsteady SST DES. Thus, it deemed suitable to utilize this turbulence model for the calculations in the control investigation.

CHAPTER 5

FLOW CONTROL USING BLEEDING

In order to delay the vortex breakdown, employment of bleeding control method was numerically simulated. As previously stated, this control technique proposes to use bleed holes on the wing body. At angle of attack, the air that will inherently stream along these holes, from the pressure side to the suction side, is supposed to excite the vortical flow field in a manner to reinforce the primary vortex and shift its breakdown location downstream.

In this study, it was decided to perform the control simulations under the same free stream conditions specified for the previous stages, that is $Re_{mac} = 1 \times 10^6$ and $M = 0.07$, and keeping the wing at 23° angle of attack again. It was also decided to place just one hole on the wing and locate its outlet before the section $x/C = 0.65$, aiming to effect the vortex prior to its breakdown as the fundamental strategy. Besides, bleeding in the parallel direction to the vortical flow and through a constant cross section hole, at a position having a certain distance to the vortex axis, was considered as being the case to be handled. The vortex axis was accepted as the line passing through the mid-section of the primary low pressure region revealed on the surface C_p contours presented previously. In addition to these, not to disturb the shear layer feeding of the primary vortex at the leading edge, the hole was decided to be placed inboard of the vortex axis and as to go through only the flat plate section of the wing.

After assigning the main characteristics of the method as above, it was decided to fix the position of the bleeding outlet and to investigate the effects of three hole parameters, as being the size (bleed area), inclination angle (angle between the hole axis and the wing flat surface) and shape, on retardation of the vortex breakdown.

In order to determine a common position for the holes to be investigated as well as to understand what arrangements would be good and proper for their sizing, some initial observations were needed to be made, first.

Holes only having rectangular cross sections with rounded corners were designed for these trials, as a common application seen also in previous work for VFE-2 wings [6]. Additionally, as being higher than the angle of attack of the wing, the inclination angles of the holes were set to 25° , in order to assure that a sufficiently good value was assigned to this parameter, referring to the work of Çelik et al. [54].

As previously mentioned, SST k- ω -cc was selected as the turbulence model to use along with the Mesh 3, for the calculations in this chapter. The domain meshes were regenerated with the necessary refinements at the regions of the bleed holes. The resulting grids, however, did not significantly differ from the Mesh 3 in terms of neither quality nor quantity.

Considering the results of these preliminary calculations, the outlet position of the bleed hole was fixed and the ranges of parameters were determined. Thus, 11 different holes, including different bleed hole sizes, shapes and angles were built and addressed in a way of strategy presented in Table 5.1. The aim of this strategy was to keep two of the parameters constant in every set and change only the one to be investigated to see the effect of its change on the breakdown delay. A base configuration was needed in order to do so and Hole 1 was selected for this purpose.

For the size investigation, three holes named as small, medium and large, were generated. They had rectangular form and 25° inclination angle in common. The increment rate between each of their bleed areas was set to 1.5. The aspect ratios of the three holes were kept constant too.

In the angle effect investigation, three holes having small rectangle cross sections and 20° , 30° and 35° inclination angles were tested to compare their results with Hole 1, which possess 25° bleed angle.

Table 5.1 Control work strategy

	Hole No.	Hole Size	Hole Shape	Hole Angle	Bleed Area ² (cm)	Aspect Ratio
Size Effect Investigation Set (<i>Area Enlargement Ratio = 1.5</i>)	1	Small	Rectangle	25°	16.53	1.27
	2	Med.	Rectangle	25°	25.2	1.29
	3	Large	Rectangle	25°	37.64	1.27
Angle Effect Investigation Set	1	Small	Rectangle	25°	16.53	1.27
	4	Small	Rectangle	20°	16.53	1.27
	5	Small	Rectangle	30°	16.53	1.27
	6	Small	Rectangle	35°	16.53	1.27
Shape Effect Investigation Set	1	Small	Rectangle	25°	16.53	1.27
	7	Small	Circle	25°	16.53	-
	8	Small	High A/R Chord wise Rectangle	25°	16.53	1.93
	9	Small	Chord wise Slot	25°	16.53	4.35
	10	Small	High A/R Span wise Rectangle	25°	16.53	0.52
	11	Small	Span wise Slot	25°	16.53	0.23

A/R: Aspect Ratio

Shape investigation was performed using holes having the same bleed area and angle as Hole 1, however different shapes and inherently different aspect ratios than each other. One of these holes had a circular cross section. Other holes were mainly two types and each of them had both a chord wise and span wise orientation. One of these two was named as ‘high aspect ratio (a/r) rectangle’ and the other as ‘slot’. All these

five holes were tested and again compared with Hole 1 in terms of their efficiencies, in scope of the shape investigation.

Figure 5.1 reveals in detail the location of Hole 1 over the wing (a), the sketch of its cross section on the upper wing surface with the corresponding relations (b) and its inclination angle (c). Figure 5.2, on the other hand, gives the isometric views of the wing with Hole 1 placed on it.

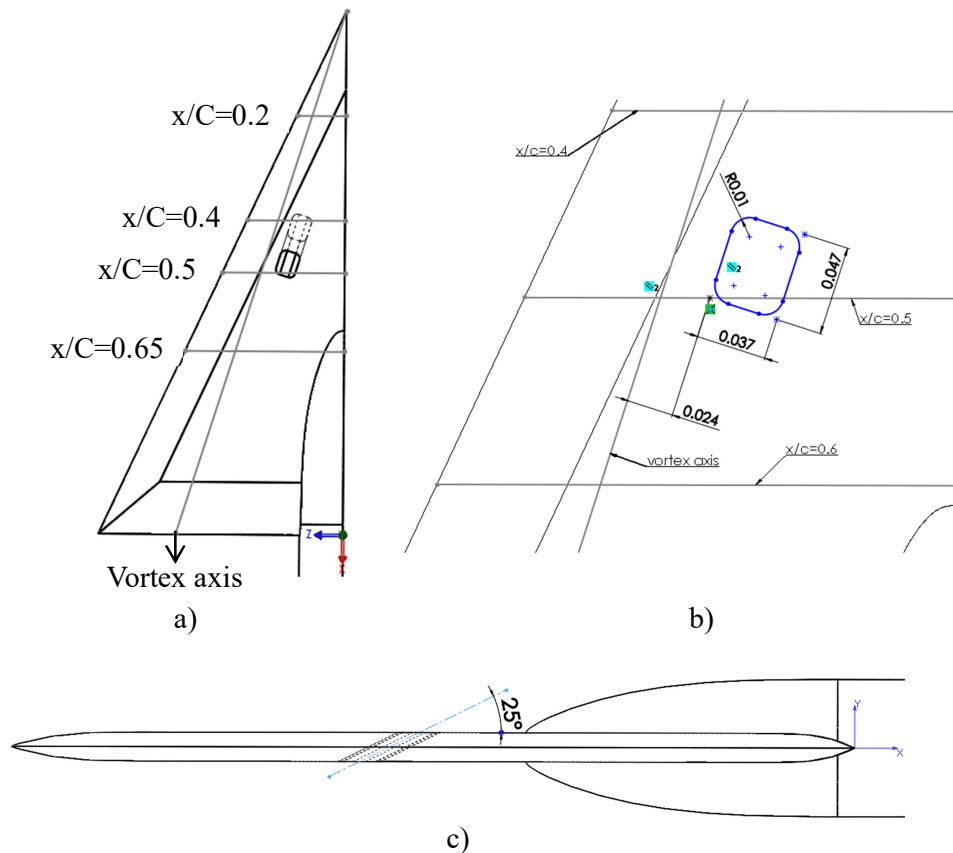


Figure 5.1 Hole 1: a) location (top view), b) sketch on the upper surface and c) side view

Figure 5.1 (b) is also a sample to demonstrate the fixed location for all the 11 holes, aforementioned above. The dimension between the vortex axis and the outlet, set as 0.024 m, was kept constant for all sketches of others. Besides, all their outlets were settled parallel to the vortex axis and on the $x/C = 0.5$ line as another constraint. Moreover, in the slot and rectangular formed holes, $R = 0.01$ was assigned as a

standard value for the slot head and fillet radius. The outlet of the circular hole, on the other hand, was placed on the geometric center of the rectangular cross section.

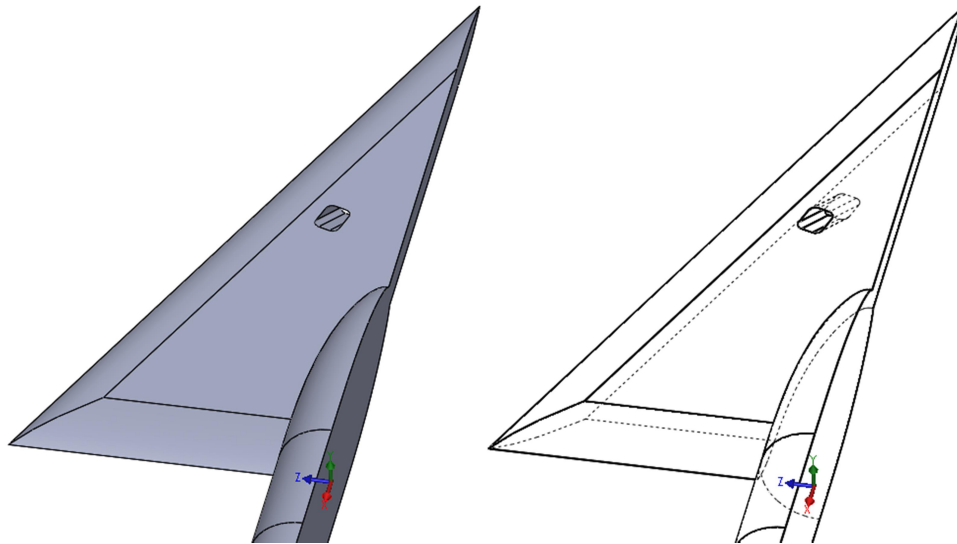


Figure 5.2 Hole 1 isometric views

Size investigation set is presented in Figure 5.3. Angle and Shape investigation sets, though, are provided in Figure 5.4 and Figure 5.5 correspondingly.

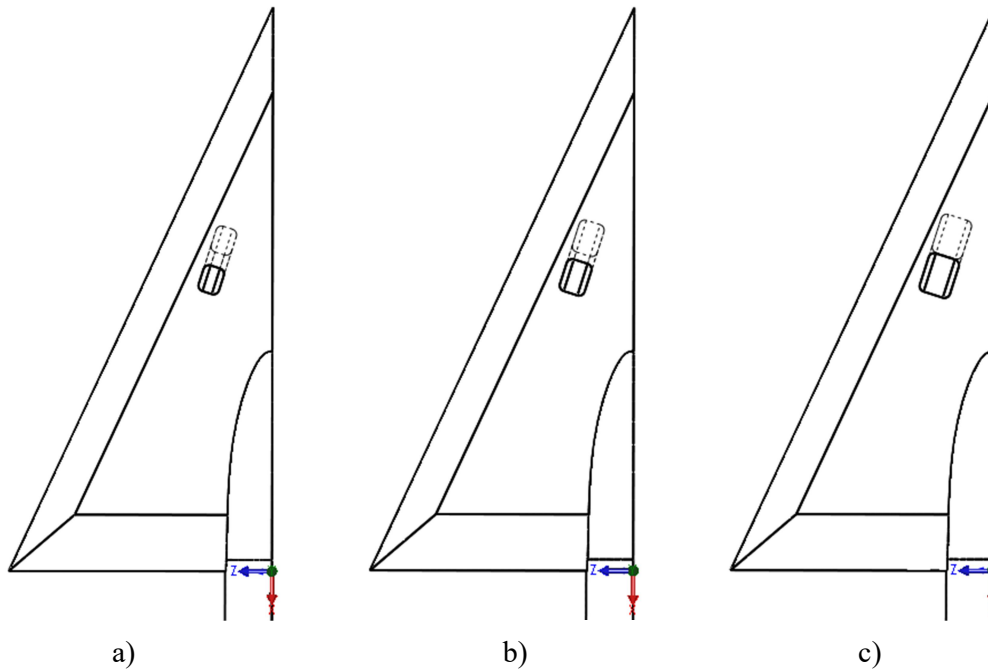


Figure 5.3 Size investigation set a) Hole 1, b) Hole 2 and c) Hole 3

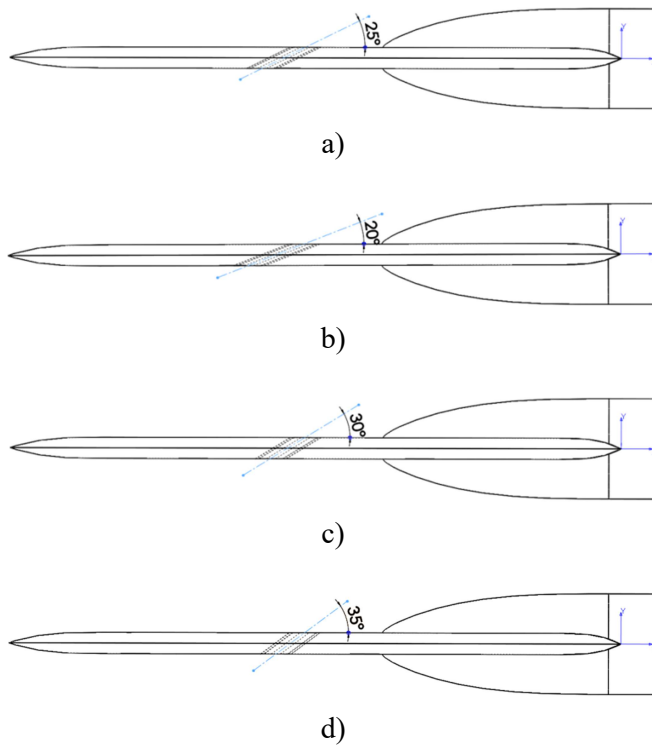
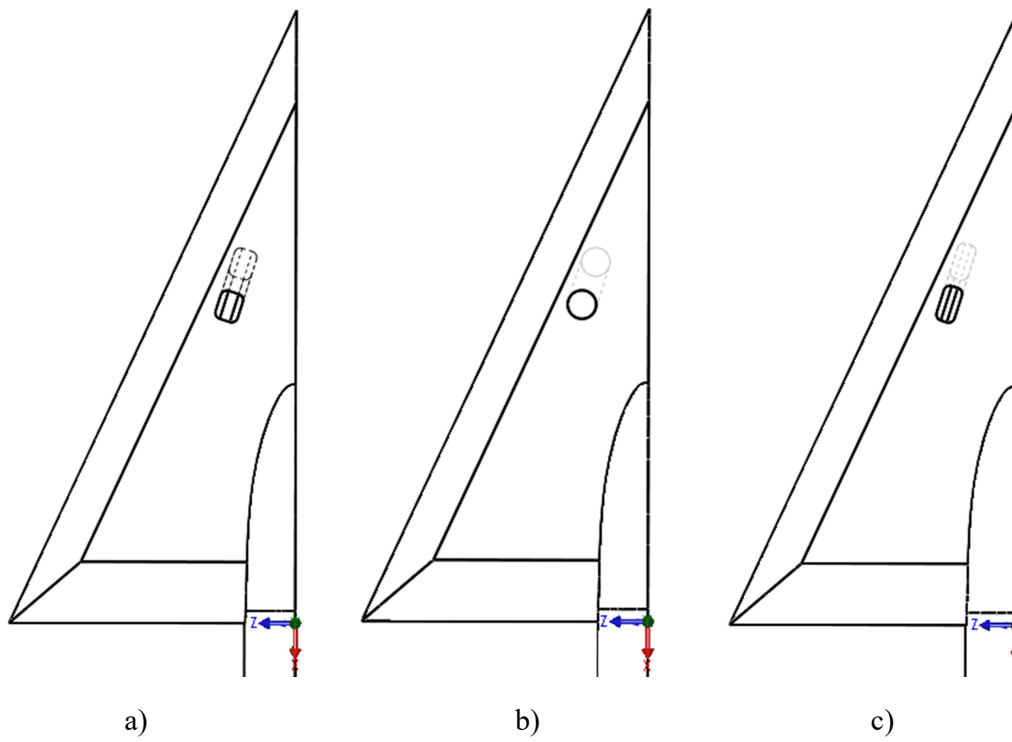


Figure 5.4 Angle investigation set a) Hole 1, b) Hole 4, c) Hole 5 and d) Hole 6



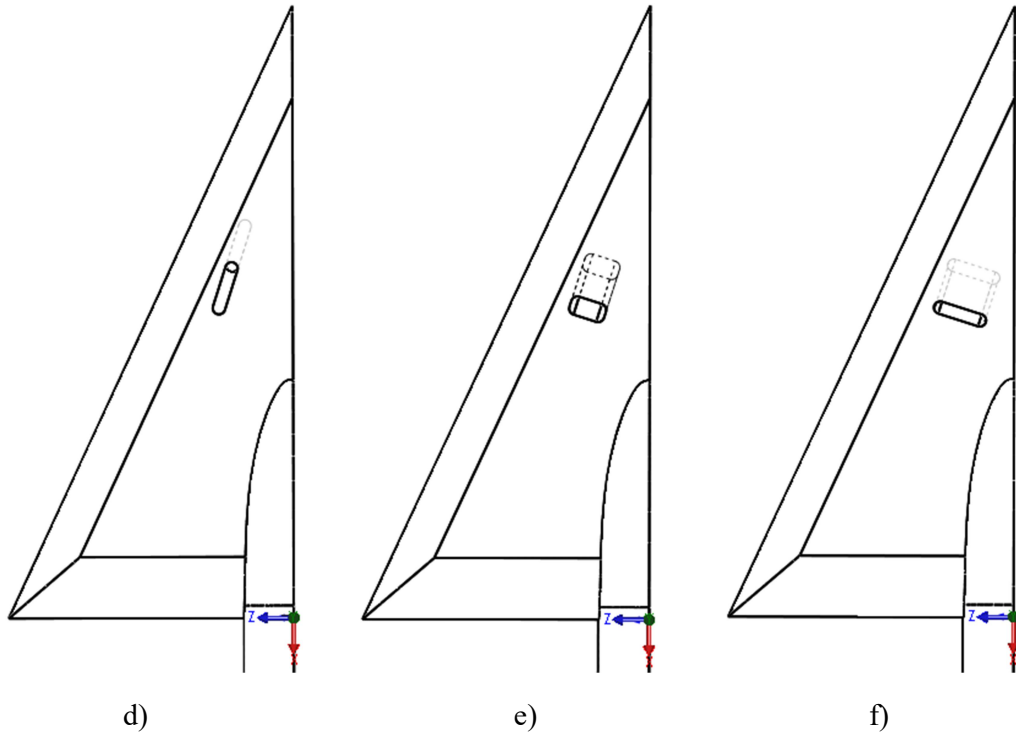


Figure 5.5 Shape investigation set a) Hole 1, b) Hole 7, c) Hole 8,
d) Hole 9, e) Hole 10 and f) Hole 11

Bleeding efficiencies of the 11 holes were assessed by comparing their calculated breakdown locations with the one belonging to the base (no-control) case, which was the solution of the SST $k-\omega$ -cc simulation of Mesh 3 without control. The vortex breakdown location of the base (no-control) case, which is at $x/C=0.65$, and the 11 bleeding control simulations were presented in Table 5.2.

In the size investigation, the solution with Hole 1 yielded the breakdown at the section of $x/C=0.69$, which is further downstream of the no-control case. However, Hole 2 having a medium size and Hole 3 having a large one shifted the breakdown better than that and to approximately the same position, $x/C=0.71$. Since nearly the same performance could be obtained by a smaller bleed outlet, Hole 2 was considered as the best of its set.

Regarding the effect of the inclination angle to the bleeding control performance, it can be said the retardation of the breakdown was improved with increasing the hole

angle from 20° to 30° . However, increasing the angle after this point turned out an earlier breakdown for Hole 6, having 35° inclination, compared with other cases. Thus, bleeding through 30° inclined Hole 5 seemed giving the best result for this investigation, with the vortex breakdown at $x/C= 0.71$.

For the shape effect investigation though, both chord wise and span wise slot simulations yielded a breakdown at $x/C= 0.66$ which can be said to be close to the no-control case. On the other hand, the high a/r rectangle holes enabled a vortex burst displacement till $x/C= 0.70$ station. However, bleeding through Hole 7 with the circular cross section apparently looked the most efficient in the set, delaying the vortex breakdown to $x/C= 0.73$.

Considering that combining the best performing parameters of each set might have a linear effect on the displacement of the breakdown onset, a new bleed hole with medium size, 30° inclination angle and circular shape was generated under name Hole 12 and its control efficiency was investigated with a new simulation. However, as can be seen in Table 5.2 the breakdown took place for this hole at $x/C= 0.68$, which means that the best parameters superposition did not contribute to the performance of the bleeding manipulation proportionally, as it was the case intended.

The visualization of the swirling strength of the vortical flow structure over the wing for the base (no-control) case and the best control cases of the investigations above (Hole 2, Hole 5 and Hole 7) were presented in Figure 5.6. The leading edge separations and the feedings of the vortex filaments to the primary vortex, as well as the vortex cores with the high stream wise velocity and their sudden expansion in the region of their breakdown can clearly be seen in this figure. Besides of these, air bleedings coming out of the hole outlets and their successful involvement to the flow field are revealed by this figure. The horizontal yellow lines indicate the positions of the vortex breakdown. The downstream shifts of the breakdowns of the vortices can be recognized easily from the figure, too.

Table 5.2 Control work vortex breakdown locations

	Hole No.	Hole Size	Hole Shape	Hole Angle	Breakdown Location x/C
	Base (no-control)	-	-	-	0.65
Size Effect Investigation Set	1	Small	Rectangle	25°	0.69
	*2	Med.	Rectangle	25°	0.71
	3	Large	Rectangle	25°	0.71
Angle Effect Investigation Set	1	Small	Rectangle	25°	0.69
	4	Small	Rectangle	20°	0.68
	*5	Small	Rectangle	30°	0.71
	6	Small	Rectangle	35°	0.66
Shape Effect Investigation Set	1	Small	Rectangle	25°	0.69
	*7	Small	Circle	25°	0.73
	8	Small	High A/R Chord wise Rectangle	25°	0.68
	9	Small	Chord wise Slot	25°	0.66
	10	Small	High A/R Span wise Rectangle	25°	0.70
	11	Small	Span wise Slot	25°	0.66
Best Parameter Combination	12	Med.	Circle	30°	0.68

* Chosen as the best of their sets.

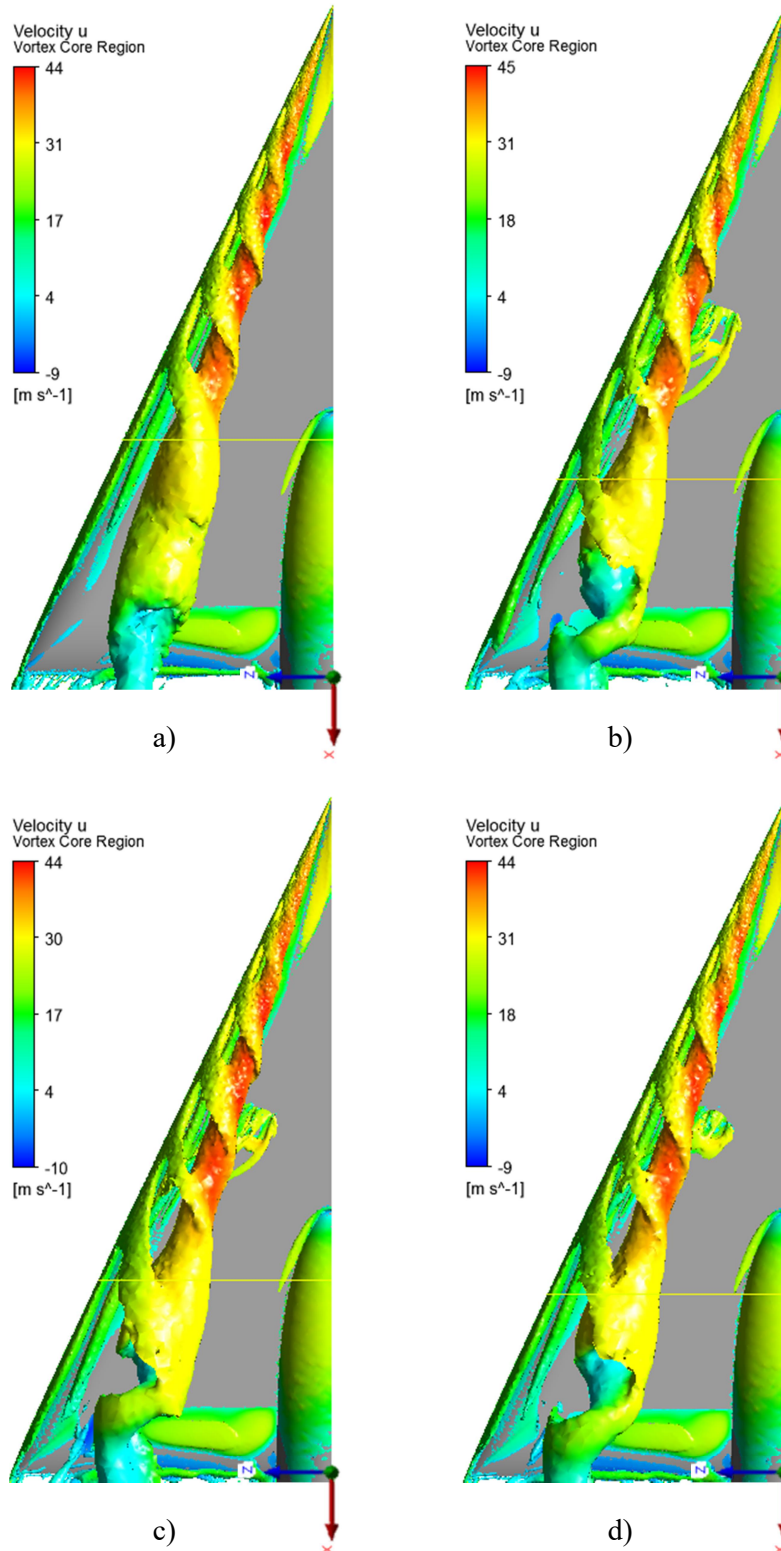


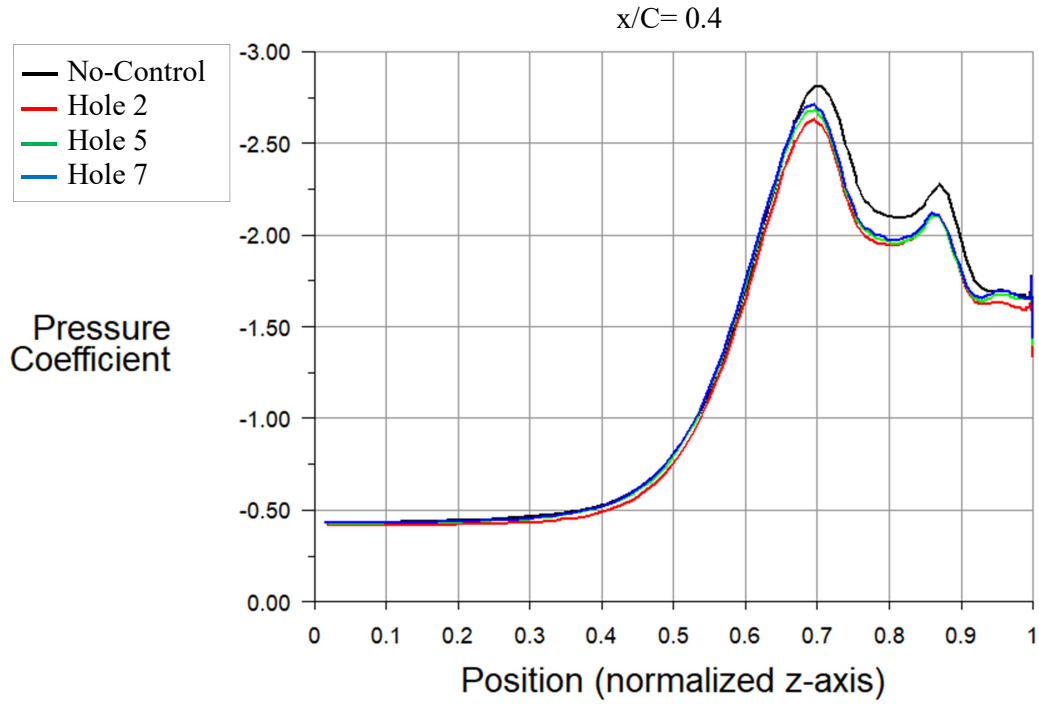
Figure 5.6 Swirling strength colored by stream-wise velocity for: a) Base, b) Hole 2, c) Hole 5 and d) Hole 7. Horizontal yellow line shows the vortex breakdown location

The effect of bleeding control on the vortical flow can also be understood by checking span wise C_p distributions on the wing surface. Figure 5.7 reveals the C_p graphics of the no-control case and the best resulted control applications, i.e., Hole 2, Hole 5 and Hole 7 solutions, plotted at three chord wise stations $x/C= 0.4, 0.65$ and 0.8 . It is evident that in the first station the primary and secondary peaks are higher in the no-control case. This can be seen as an estimated situation since the leading edge vortex was supposed to endure longer in the controlled cases and so its strength increase might have followed a different trend.

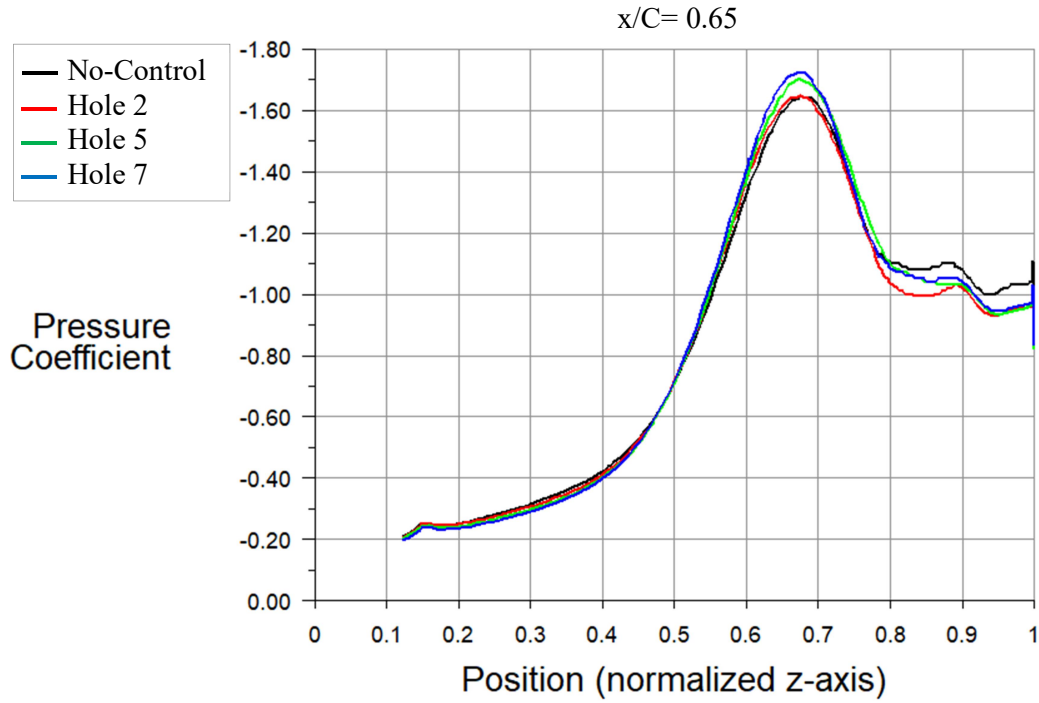
Hole 5 and Hole 7 simulations show clearly stronger primary vortex at the breakdown location of the no-control case $x/C= 0.65$, and Hole 2 solution gives the same primary peak value with the non-controlled solution, being different from the previous station. All three controlled cases, on the other hand, yield slightly weaker secondary vortex. The progression in the C_p profiles of the controlled cases on this location means the successful stabilization of the vortical flow by the bleeding control through the holes.

Proceeding towards the trailing edge, the effect of bleeding control becomes more obvious. Even in the region after the breakdown, e.g., at $x/C= 0.8$, the primary suction is observed apparently higher in the controlled cases. Besides, the relation for the C_p distributions of the bleeding holes seems to be in agreement with their corresponding breakdown locations.

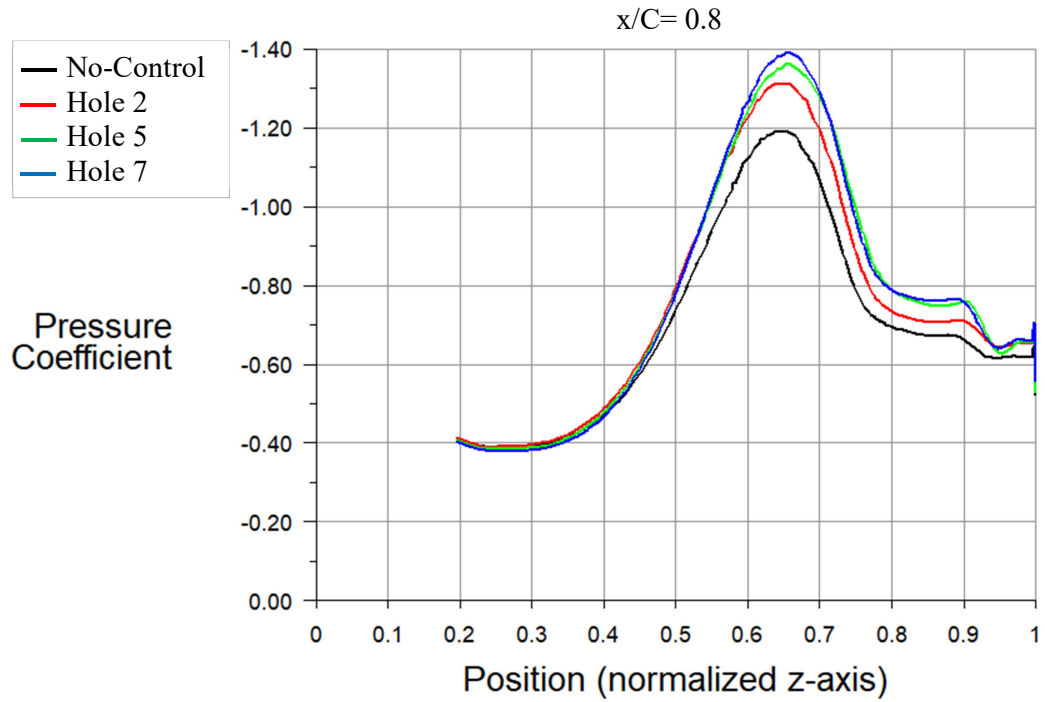
The ultimate goal of the flow control effort is to enhance the aerodynamic capability of the delta wing and one of the most important measures for this is to check the lift variation. Table 5.3 presents the lift forces exerted on the wing body as well as the corresponding coefficients resulted from the simulations of the no-control and the abovementioned three control cases, i.e., Hole 2, Hole 5 and Hole 7 solutions. Looking this table, a slight improvement in the lift force and the related coefficient is evident for the controlled cases.



a)



b)



c)

Figure 5.7 Span wise C_p profiles of the non-controlled and three controlled cases at chord wise stations on the suction side a) $x/C=0.4$, b) $x/C=0.65$ and c) $x/C=0.8$

Table 5.3 Lift Variation between the No-Control and Control Cases

	Lift Force (N)	Lift Coefficient
No-Control	74.59	0.314
Hole 2	75.74	0.319
Hole 5	76.23	0.321
Hole 7	75.83	0.319

CHAPTER 6

CONCLUSION

6.1 Summary and Conclusions

Turbulent incompressible vortical flow around a sharp edged VFE- 2 wing was modeled numerically using commercial CFD code ANSYS Fluent. By doing so, two different RANS based turbulence models were employed. First of them was a two-equation eddy viscosity model SST $k-\omega$ while the second was S-A with one closure equation and for both of the models curvature correction term was added in order to sensitize them to streamline curvatures. All computations were steady and done under fully turbulent approach. A mesh independence investigation was performed first by building a mesh refinement strategy and this showed the importance of the grid resolution near the edges and at critical locations to capture the separations and attachments as well as boundary layer features sufficiently well. The obtained numerical data then was compared with unsteady SST DES solutions and experimental findings from literature. SST $k-\omega$ was validated against the experiment and assessed as more successful than S-A in resolving the vortical flow features like the secondary separation, the secondary vortex and the shear layers surrounding the vortices, as well as in predicting the location of the primary vortex breakdown. Besides, as a steady RANS model, it revealed notably close, sometimes even better performance comparing with unsteady hybrid DES.

Bleeding control technique was conducted numerically using the mesh independent SST $k-\omega$ model again. Three hole parameters being size, inclination angle and shape were addressed in three sets of investigations and 11 configurations in total, fixing their outlet locations as presented in the study. The most effective parameter in each set in terms of vortex breakdown delay was determined. According to the results, it was managed in each set to strengthen the vortex and shift its breakdown to about 10% downstream of the chord wise location of the no-control case, besides achieving

a little amount of increase in the lift force and coefficient. However, combining the best parameters of the sets yielded a poorer performance comparing the individual investigation cases.

6.2 Recommendations for Future Work

Bleeding, as a novel passive flow control method, was applied to the VFE-2 wing and good results in terms of vortex breakdown retardation could be obtained. However, great number of investigation cases can be deduced by setting different parameters such as numbers and locations of the holes, bleeding direction, or even the parameters investigated in this study for future works.

Besides, the same hole was used as the base control case in each set as the strategy of the present study and the computations for each set were done separately. Following these computations the superposition of the best performing parameters was investigated as a last step. However, first determining the superior hole of one set, e.g., medium hole for the size set, and taking it as the base for the second set, i.e., using the medium size now as one of the constant parameters, and finally carrying the best performing hole of the second investigation set to the third one as to be the base case for it with the same logic, can be an interesting alternative approach for control investigations.

The calculations in the current study were carried out steady and that yielded the time average values of the quantities. However, unsteady phenomenon such as the vortex wandering or the oscillation of the breakdown location, reviving as a consequence of the unsteady nature of the vortical flow over slender delta wings, can be tried to be captured using transient models. On the other hand, fully turbulent approach was employed in the solutions under the present study. VFE-2 mostly handled flow regimes with $Re \geq 3 \times 10^6$ numerically, and in these cases fully turbulent solutions gave similar results to the experiments. However for lower Re cases, as it was in the present study, the laminar to turbulent boundary layer transition may play a major role on the flow behavior. Therefore in future works, models respecting this transition can also be employed in order to capture this important phenomenon.

REFERENCES

- [1] S. Z. Pirzadeh, "Vortical Flow Prediction Using an Adaptive Unstructured Grid Method," *RTO AVT Symposium on Advanced Flow Management, Part A – Vortex Flows and High Angle of Attack for Military Vehicles*, 2001.
- [2] A. M. Mitchell, J. Delery, "Research into Vortex Breakdown Control," *Progress in Aerospace Sciences*, vol. 37, no. 4, pp. 385-418, May 2001.
- [3] D. Hummel, "The International Vortex Flow Experiment 2 (VFE-2): Objectives and Overview," *RTO-TR-AVT-113 - Understanding and Modeling Vortical Flows to Improve the Technology Readiness Level for Military Aircraft*, Chapter 17, 2008.
- [4] J. Chu and J. M. Luckring, "Experimental Surface Pressure Data Obtained on 65° Delta Wing Across Reynolds Number and Mach Number Ranges," *NASA Technical Memorandum 4645*, 1996.
- [5] T. Hu, Z. Wang and I. Gursul, "Passive Control of Roll Oscillations of Low-Aspect-Ratio Wings Using Bleed," *University of Bath*, 2014.
- [6] C. Zwerger, S. Hickel, C. Breitsamter and N. Adams, "Wall-Modeled Large-Eddy Simulation of the VFE-2 Delta Wing," *33rd AIAA Applied Aerodynamics Conference*, 2015.
- [7] E. Tangermann and A. Furman and C. Breitsamter "Detached Eddy Simulation compared with Wind Tunnel Results of a Delta Wing with Sharp Leading Edge and Vortex Breakdown," *30th AIAA Applied Aerodynamics Conference*, 2012.
- [8] A. Furman and C. Breitsamter, "Experimental Investigations on the VFE-2 Configuration at TU Munich, Germany," *RTO-TR-AVT-113- Understanding and Modeling Vortical Flows to Improve the Technology Readiness Level for Military Aircraft*, Chapter 21, 2008.
- [9] S. Crippa, "Advances in Vortical Flow Prediction Methods for Design of Delta-Winged Aircraft," *KTH School of Engineering Sciences*, 2008.

- [10] F. M. Payne, T. Terry, R. C. Nelson, "Visualization of Leading Edge Vortices on a Series of Flat Plate Delta Wings," *NASA Contractor Report 4320, University of Notre Dame*, 1991.
- [11] M. R. Visbal, "Computational and Physical Aspects of Vortex Breakdown on Delta Wings" *33rd Aerospace Science Meeting & Exhibit, AIAA*, 1995.
- [12] C. Breitsamter, "Unsteady Flow Phenomena Associated with Leading-Edge Vortices," *Progress in Aerospace Sciences*, vol. 44, no. 1, pp. 48–65, 2008.
- [13] D. Hummel, "Effects of Boundary Layer Formation on the Vortical Flow above Slender Delta Wings," *RTO AVT Specialists' Meeting on Enhancement of NATO Military Flight Vehicle Performance by Management of Interacting Boundary Layer Transition and Separation*, 2004.
- [14] R. C. Nelson, A. Pelletier, "The unsteady aerodynamics of slender wings and aircraft undergoing large amplitude maneuvers," *Progress in Aerospace Sciences*, vol. 39, pp. 185-248, 2003.
- [15] P. B. Earnshaw, "An experimental investigation of the structure of a leading edge vortex," *RIAE Tech Note No. Aero. 2740*, March 1961.
- [16] I. Gursul, "Review of Unsteady Vortex Flows over Slender Delta Wings," *Journal of Aircraft*, vol. 42, no. 2, pp. 299-319, Mar.-Apr. 2005.
- [17] N. C. Lambourne and D. W. Bryer, "The Bursting of Leading-Edge Vortices - Some Observations and Discussion of the Phenomenon" *Aeronautical Research Council Reports and Memoranda*, Ministry of Aviation, no. 3282, 1962.
- [18] R. C. Nelson, K. D. Visser, "Breaking down the delta wing vortex," *Vortex flow aerodynamics, AGARD-CP-494*, Scheveningen, The Netherlands, October 1–4, 1991. p. 21-1–15.
- [19] M. Menke, H. Yang, I. Gursul, "Experiments on the unsteady nature of vortex breakdown over delta wings," *Experiments in Fluids*, vol. 27, pp. 262-272, 1999.
- [20] F. M. Payne, "The structure of leading edge vortex flows including vortex breakdown," *University of Notre Dame*, May 1987.
- [21] M. Gad-El-Hak and R. F. Blackwelder, "The Discrete Vortices from a Delta Wing," *AIAA Journal*, vol. 23, no. 6, pp. 963–962, 1985.

- [22] M. Gad-El-Hak and R. F. Blackwelder, “Control of the Discrete Vortices From a Delta Wing,” *AIAA Journal*, vol. 25, no. 8, pp. 1042–1049, 1987.
- [23] R. E. Gordnier and M. R. Visbal, “Unsteady vortex structure over a delta wing,” *Journal of Aircraft*, vol. 31, no. 1, pp. 243–248, 1994.
- [24] A. M. Mitchell, P. Molton, “Vortical Substructures in the Shear Layers Forming Leading-Edge Vortices,” *AIAA Journal Technical Notes*, vol. 40, no. 8, pp., 1689-1692, 2002.
- [25] A. E Washburn, K. D. Visser, “Evolution of the Vortical Structures in the Shear Layer of Delta Wings,” *25th AIAA Fluid Dynamics Conference*, AIAA Paper 94–2317, 1994.
- [26] M. Menke and I. Gursul, “Unsteady Nature of Leading Edge Vortices,” *Physics of Fluids*, vol. 9, no. 10, pp. 1-7, 1997.
- [27] J. M. Luckring, “Initial Experiments and Analysis of Blunt-Edge Vortex Flows,” *RTO-TR-AVT-113- Understanding and Modeling Vortical Flows to Improve the Technology Readiness Level for Military Aircraft*, Chapter 18, 2008.
- [28] J. M. Luckring, “Reynolds Number, Compressibility, and Leading-Edge Bluntness Effects on Delta-Wing Aerodynamics,” *24th International Congress of the Aeronautical Sciences*, 2004.
- [29] A. Furman and C. Breitsamter, “Turbulent and unsteady flow characteristics of delta wing vortex systems,” *Aerospace Science and Technology*, vol. 24, pp. 32-44, 2013.
- [30] A. Furman and C. Breitsamter, “Investigation of Flow Phenomena on Generic Delta Wing,” *25th International Congress of the Aeronautical Sciences*, 2006.
- [31] D. Hummel, “Final Results of the International Vortex Flow Experiment – Resumé and Outlook,” *RTO-TR-AVT-113 - Understanding and Modeling Vortical Flows to Improve the Technology Readiness Level for Military Aircraft*, Chapter 35, 2008.
- [32] H. Werlé, “Quelques résultats expérimentaux sur les ailes en flèche, aux faibles vitesses, obtenus en tunnel hydrodynamique” *La Recherche Aéronautique*, no. 41, pp. 15-21, 1954.

- [33] D. H. Peckham, S. A. Atkinson, "Preliminary Results of Low Speed Wind Tunnel Tests on a Gothic Wing of Aspect Ratio 1.0," *Aeronautical Research Council, Current Papers-508*, 1957.
- [34] J. Rom, "High Angle of Attack Aerodynamics", *Springer Verlag*, 1992.
- [35] M. J. Lee, C. M. Ho, "Vortex dynamics of delta wings," *Frontiers in Experimental Fluid Mechanics, Lecture Notes in Engineering*, vol. 46. Berlin: Springer, 1989. p. 365–427.
- [36] M. G. Hall, "A Theory for the Core of a Leading- Edge Vortex," *Journal of Fluid Mechanics*, vol. 11, pp. 209-228, 1961.
- [37] T. B. Benjamin, "Theory of the Vortex Breakdown Phenomenon," *Journal of Fluid Mechanics*, vol. 14, No. 4, pp. 593–629, 1962.
- [38] J. Delery, "Aspects of Vortex Breakdown," *Progress in Aerospace Sciences*, vol. 30, no. 1, pp. 1-59, 1994.
- [39] J Lopez, "Axisymmetric Vortex Breakdown Part 1: Confined Swirling Flow," *Journal of Fluid Mechanics*, vol. 221, pp. 533–552, 1990.
- [40] G. L Brown, J. M Lopez, "Axisymmetric Vortex Breakdown Part 2: Physical Mechanisms," *Journal of Fluid Mechanics*, vol. 221, pp. 553–576, 1990.
- [41] M. Jones, A. Hashimoto, Y. Nakamura, "Criteria for Vortex Breakdown Above High-Sweep Delta Wings," *AIAA Journal*, vol. 47, no. 10, 2009.
- [42] I. Gursul, "Unsteady Flow Phenomena Over Delta Wings at High Angle of Attack," *AIAA Journal*, vol. 32, no. 2, pp. 225–231, 1994.
- [43] I. Gursul, Z. Wang, and E. Vardaki, "Review of Flow Control Mechanisms of Leading-Edge Vortices," *Progress in Aerospace Sciences*, vol. 43, no. 7–8, pp. 246–270, 2007.
- [44] A. Kölzsch and C. Breitsamter, "Vortex-Flow Manipulation on a Generic Delta-Wing Configuration," *Journal of Aircraft*, vol. 51, no. 5, pp. 1380–1390, 2014.
- [45] M. R. Visbal, D. V. Gaitonde, "Control of Vortical Flows Using Simulated Plasma Actuators," *44th AIAA Aerospace Sciences Meeting and Exhibit*, January 2006.
- [46] S. Phillips, C. Lambert, and I. Gursul, "Effect of a Trailing-Edge Jet on Fin Buffeting Introduction," *Journal of Aircraft*, vol. 40, no. 3, pp. 590–599, 2003.

- [47] R. Konrath, C. Klein, A. Schröder, K. de Groot, “Experimental Investigations on the VFE-2 Configuration at DLR, Germany,” *RTO-TR-AVT-113 - Understanding and Modeling Vortical Flows to Improve the Technology Readiness Level for Military Aircraft*, Chapter 19, 2008.
- [48] İ. C. Kucukyilmaz, “Control of Flow Structure on 70° Swept Delta Wing with the Along-Core Blowing Using Numerical Modeling,” M.S. Thesis, Dept. Mech. Eng. Dept., METU., Ankara, Turkey, 2016.
- [49] P. R. Spalart, S. R. Allmaras, “A One-Equation Turbulence Model for Aerodynamic Flows,” 30th *AIAA Aerospace Sciences Meeting and Exhibit*, January 1992.
- [50] ANSYS Fluent Tutorial
- [51] F. R. Menter, “Two-Equation Eddy-Viscosity Turbulence Models for Engineering Applications,” *AIAA Journal*, vol. 32, no. 8, pp. 1598-1605, 1994.
- [52] P. R. Spalart, M. Shur, “On the Sensitization of Turbulence Models to Rotation and Curvature Aerospace Science and Technology,” *Aerospace Science and Technology*, no: 5, pp. 297-302, 1997.
- [53] P. E. Smirnov, F. R. Menter “Sensitization of the SST Turbulence model to Rotation and Curvature by Applying the Spalart-Shur Correction Term,” *Proceedings of ASME Turbo Expo 2008: Power for Land, Sea and Air*, GT2008-50480, 2008.
- [54] A. Çelik, C. Çetin and M. M. Yavuz “Effect of Passive Bleeding on Flow Structure over a Nonslender Delta Wing,” *AIAA Journal*, vol. 55, no. 8, pp. 2555-2565, 2017.

APPENDIX A

TURBULENCE MODELING

A.1. Spalart-Allmaras Model (Continued From Section 3.3.2)

The production term is modeled as:

$$G_v = C_{b1}\rho\tilde{S}\tilde{\nu} \quad (\text{A.1})$$

$$\tilde{S} \equiv S + \frac{\tilde{\nu}}{\kappa^2 d^2} f_{v2} \quad (\text{A.2})$$

$$f_{v2} = 1 - \frac{\chi}{1 + \chi f_{v1}} \quad (\text{A.3})$$

Here, C_{b1} and κ are constants, d is the distance from the wall, and S is a scalar measure of the deformation tensor. S is based on the magnitude of the vorticity in the original model proposed by Spalart and Allmaras as:

$$S \equiv \sqrt{2\Omega_{ij}\Omega_{ij}} \quad (\text{A.4})$$

$$\Omega_{ij} = \frac{1}{2} \left(\frac{\partial u_i}{\partial x_j} - \frac{\partial u_j}{\partial x_i} \right) \quad (\text{A.5})$$

Ω_{ij} is the mean rate of rotation tensor here. However, vorticity and strain rate are identical for shear flows. Besides, vorticity has the advantage of being zero in inviscid flow regions like stagnation lines, where turbulence production due to strain rate can be unphysical. That is why a modification that combines the measures of both vorticity and the strain tensors in the definition of S can be done as:

$$S \equiv |\Omega_{ij}| + C_{\text{prod}} \min(0, |S_{ij}| - |\Omega_{ij}|) \quad (\text{A.6})$$

$$C_{\text{prod}} = 2.0, |\Omega_{ij}| \equiv \sqrt{2\Omega_{ij}\Omega_{ij}}, |S_{ij}| \equiv \sqrt{2S_{ij}S_{ij}} \quad (\text{A.7})$$

And the mean strain rate is defined as:

$$S_{ij} = \frac{1}{2} \left(\frac{\partial u_j}{\partial x_i} + \frac{\partial u_i}{\partial x_j} \right) \quad (\text{A.8})$$

The destruction term on the other hand can be modeled as follows:

$$Y_v = C_{w1} \rho f_w \left(\frac{\tilde{v}}{d} \right)^2 \quad (\text{A.9})$$

$$f_w = g \left[\frac{1 + C_{w3}^6}{g^6 + C_{w3}^6} \right]^{1/6} \quad (\text{A.10})$$

$$g = r = +C_{w2}(r^6 - r) \quad (\text{A.11})$$

$$r \equiv \frac{\tilde{v}}{\tilde{S} \kappa^2 d^2} \quad (\text{A.12})$$

C_{w1} , C_{w2} and C_{w3} are constants here and \tilde{S} is given by equation A.2.

All the modeling constants mentioned above are given as:

$$C_{b1} = 0.1355, \quad C_{w1} = \frac{C_{b1}}{\kappa^2} + \frac{(1 + C_{b2})}{\sigma_{\tilde{v}}}$$

$$C_{w2} = 0.3, \quad C_{w3} = 2.0, \quad \kappa = 0.4187$$

In ANSYS Fluent, the commercial code utilized in this study, a y^+ insensitive wall treatment extension (Enhanced Wall Treatment) exists in S-A model. All solution variables are blended by this treatment from their viscous sub layer formulation as:

$$\frac{u}{u_\tau} = \frac{\rho u_\tau y}{\mu} \quad (\text{A.13})$$

to the corresponding logarithmic layer values depending on y^+ with:

$$\frac{u}{u_\tau} = \frac{1}{\kappa} \ln \kappa \frac{\rho u_\tau y}{\mu} \quad (\text{A.14})$$

Here, y is the distance from the wall, u_τ is the shear velocity and u is the velocity parallel to the wall. Besides, κ is the von Kármán constant (0.4187), and $E = 9.793$. This blending also covers intermediate y^+ values in the buffer layer ($1 < y^+ < 30$).

A.2. Shear-Stress Transport (SST) k - ω Model (Continued From Section 3.3.3)

Looking at the modeling the turbulence productions and firstly the production of the turbulence kinetic energy, the term \tilde{G}_k of equation 3.10 is defined as:

$$\tilde{G}_k = \min(G_k, 10\rho\beta^*k\omega) \quad (\text{A.15})$$

where

$$\beta^* = \beta_i^*[1 + \zeta^*F(M_t)] \quad (\text{A.16})$$

$$\beta_i^* = \beta_\infty^* \left(\frac{4/15 + (Re_t/R_\beta)^4}{1 + (Re_t/R_\beta)^4} \right) \quad (\text{A.17})$$

Here, ζ^* , R_β and β_∞^* are model constants as being 1.5, 8 and 0.09, respectively.

The compressibility function, $F(M_t)$, is given by

$$F(M_t) = \begin{cases} 0 & M_t < M_{t0} \\ M_t^2 - M_{t0}^2 & M_t > M_{t0} \end{cases} \quad (\text{A.18})$$

$$M_t^2 \equiv \frac{2k}{a^2} \quad (\text{A.19})$$

$$a = \sqrt{\gamma RT} \quad (\text{A.20})$$

with $M_{t0} = 0.25$ as a model constant. For equation A.20, T represents the temperature, R the gas-law constant and γ the ratio of specific heats.

G_k in A.15 is calculated as in the standard k - ω model and formulated as:

$$G_k = -\rho \overline{u_i' u_j'} \frac{\partial u_j}{\partial x_i} \quad (\text{A.21})$$

G_k can also be evaluated in a consistent way with Boussinesq hypothesis as:

$$G_k = \mu_t S^2 \quad (\text{A.22})$$

Here, S represents the modulus of the mean rate of strain tensor and defined as:

$$S \equiv \sqrt{2S_{ij}S_{ij}} \quad (\text{A.23})$$

The production of ω , indicated by the term G_ω in the transport equation 3.11, is given by

$$G_\omega = \frac{\alpha}{\nu_t} \tilde{G}_k \quad (\text{A.24})$$

$$\nu_t = \mu_t \rho \quad (\text{A.25})$$

$$\alpha = \frac{\alpha_\infty}{\alpha^*} \left(\frac{\alpha_0 + Re_t/R_\omega}{1 + Re_t/R_\omega} \right) \quad (\text{A.26})$$

In these equations $\alpha_0 = 1/9$ and $R_\omega = 2.95$, as model constants. α^* and Re_t were previously given by (3.17) and (3.18) respectively. The evaluation of the term α_∞

differs between standard k- ω and SST k- ω models. In standard k- ω model α_∞ is given as a constant. However in SST k- ω :

$$\alpha_\infty = F_1 \alpha_{\infty,1} + (1 - F_1) \alpha_{\infty,2} \quad (\text{A.27})$$

with

$$\alpha_{\infty,1} = \frac{\beta_{i,1}}{\beta_\infty^*} - \frac{\kappa^2}{\sigma_{\omega,1} \sqrt{\beta_\infty^*}} \quad (\text{A.28})$$

$$\alpha_{\infty,2} = \frac{\beta_{i,2}}{\beta_\infty^*} - \frac{\kappa^2}{\sigma_{\omega,2} \sqrt{\beta_\infty^*}} \quad (\text{A.29})$$

where $\beta_{i,1}$ and $\beta_{i,2}$ are model constants given as 0.075 and 0.0828 respectively, $\kappa = 0.41$ and β_∞^* was defined previously above.

Recalling Y_k term in the transport equation 3.10 is representing the dissipation of the turbulence kinetic energy, its definition is given by

$$Y_k = \rho \beta^* k \omega \quad (\text{A.30})$$

Calculation of β^* was previously given by A.16 and relevant consequent equations.

Similarly, Y_ω represents the dissipation of the specific dissipation rate and is formulated as:

$$Y_\omega = \rho \beta \omega^2 \quad (\text{A.31})$$

$$\beta = \beta_i \left[1 - \frac{\beta_i^*}{\beta_i} \zeta^* F(M_t) \right] \quad (\text{A.32})$$

where ζ^* was given previously as a constant value of 1.5, β_i^* by A.17 and $F(M_t)$ by A.18. Besides to these,

$$\beta_i = F_1\beta_{i,1} + (1 - F_1)\beta_{i,2} \quad (\text{A.33})$$

Here, $\beta_{i,1}$ and $\beta_{i,2}$ were given previously as model constants and F_1 is obtained from equation 3.22.

Remembering the basic operation lies under the SST k- ω model is to blend k- ϵ and k- ω models together transforming the standard k- ϵ model into equations based on k and ω , we are introduced a cross-diffusion term, which is also employed in the transport equation 3.11:

$$D_\omega = 2(1 - F_1)\rho \frac{1}{\omega\sigma_{\omega,2}} \frac{\partial k}{\partial x_j} \frac{\partial \omega}{\partial x_j} \quad (\text{A.39})$$